

# Final Report

## DNAPL Dissolution in Bedrock Fractures And Fracture Networks

SERDP Project ER-1554

June 2011

Charles Schaefer  
**Shaw Environmental, Inc.**

John McCray  
Kaneen Christensen  
Peggy Altman  
**Colorado School of Mines**

Prabhakar Clement  
Jagadish Torlapati  
**Auburn University**

*This document has been cleared for public release*



REPORT DOCUMENTATION PAGE					Form Approved OMB No. 0704-0188	
The public reporting burden for this collection of information is estimated to average 1 hour per response, including the time for reviewing instructions, searching existing data sources, gathering and maintaining the data needed, and completing and reviewing the collection of information. Send comments regarding this burden estimate or any other aspect of this collection of information, including suggestions for reducing the burden, to the Department of Defense, Executive Services and Communications Directorate (0704-0188). Respondents should be aware that notwithstanding any other provision of law, no person shall be subject to any penalty for failing to comply with a collection of information if it does not display a currently valid OMB control number.						
PLEASE DO NOT RETURN YOUR FORM TO THE ABOVE ORGANIZATION.						
1. REPORT DATE (DD-MM-YYYY) 24-06-2011		2. REPORT TYPE Final		3. DATES COVERED (From - To) April 2007 - June 2011		
4. TITLE AND SUBTITLE DNAPL Dissolution in Bedrock Fractures and Fracture Networks				5a. CONTRACT NUMBER W912HQ-07-C-0013		
				5b. GRANT NUMBER ER-1554		
				5c. PROGRAM ELEMENT NUMBER		
6. AUTHOR(S) Schaefer, Charles, E. McCray, John, E. Clement, Prabhakar				5d. PROJECT NUMBER W74RDV63530161		
				5e. TASK NUMBER		
				5f. WORK UNIT NUMBER		
7. PERFORMING ORGANIZATION NAME(S) AND ADDRESS(ES) Shaw Environmental, Inc., 17 Princess Road, Lawrenceville, NJ 08016 Colorado School of Mines, Golden, CO Auburn University, AL				8. PERFORMING ORGANIZATION REPORT NUMBER ER-1554_Final Report_final_6_23_2011		
9. SPONSORING/MONITORING AGENCY NAME(S) AND ADDRESS(ES) Strategic Environmental Research & Development Program				10. SPONSOR/MONITOR'S ACRONYM(S) SERDP		
				11. SPONSOR/MONITOR'S REPORT NUMBER(S)		
12. DISTRIBUTION/AVAILABILITY STATEMENT Approved for public release; distribution is unlimited						
13. SUPPLEMENTARY NOTES						
14. ABSTRACT This project focused on measuring and evaluating the architecture, dissolution rate, and impact on groundwater quality of residually trapped tetrachloroethene (PCE) dense non-aqueous phase liquid (DNAPL) from discrete bedrock fractures and fracture networks constructed at the bench-scale. Results demonstrated that residual DNAPL in rock fractures is not well contacted by migrating water. This resulted in reduced dissolution rates, and persistence of DNAPL sources within the bedrock fractures. Bioaugmentation was effective at substantially enhancing the rate of DNAPL removal, despite dissolved PCE concentrations that were near solubility. Chemical oxidation was shown to be ineffective for treating DNAPL sources in bedrock fractures. This ineffectiveness was due to decreases in the effective DNAPL-water interfacial area (as measured using interfacial tracers) that were likely caused by oxidation reaction byproducts.						
15. SUBJECT TERMS bedrock, fractures, PCE, bioaugmentation, chemical oxidation, DNAPL						
16. SECURITY CLASSIFICATION OF:			17. LIMITATION OF ABSTRACT	18. NUMBER OF PAGES	19a. NAME OF RESPONSIBLE PERSON	
a. REPORT	b. ABSTRACT	c. THIS PAGE			Charles Schaefer	
U	U	U	UU	144	19b. TELEPHONE NUMBER (Include area code) 609-895-5372	

Reset

## Contents

ER-1554 .....	1
LIST OF FIGURES .....	iv
LIST OF TABLES .....	vi
LIST OF ACRONYMS .....	vii
ABSTRACT.....	viii
Objectives .....	viii
Technical Approach.....	viii
Results.....	ix
Benefits .....	ix
1. OBJECTIVES .....	10
2. BACKGROUND .....	12
2.1 DNAPL Architecture and Dissolution.....	12
2.2 Bioaugmentation for Treatment of DNAPL Sources in Bedrock.....	13
2.3 Chemical Oxidation for Treatment of DNAPL Sources in Bedrock .....	14
2.4 Fracture Network Processes.....	16
3. MATERIALS AND METHODS.....	19
3.1 Overall Approach and Rationale.....	19
3.2 Task 1: Preparation of Fracture Systems – Single Fracture Systems .....	20
3.2.1 Rock Selection .....	20
3.2.2 Initial Rock Characterization .....	21
3.2.3 Construction of Discrete Fractures .....	23
3.3 Task 1: Preparation of Fracture Systems – Fracture Networks .....	27
3.3.1 Network Construction .....	27
3.3.2 Rock Characterization - Sorption .....	31
3.3.3 Rock Characterization – Rock Matrix .....	32
3.4. Task 2a: Single Fracture Characterization & Dissolution Experiments .....	33
3.4.1 Fracture Characterization without DNAPL Present .....	33
3.4.2 Dissolution of Residual DNAPL .....	34
3.4.3 Determination of DNAPL-Water Interfacial Area.....	35
3.5. Task 2b: Single Fracture Bioaugmentation Experiments .....	36
3.5.1 Batch Bioaugmentation Experiments.....	36
3.5.2 Fracture Bioaugmentation Experiments.....	37
3.6. Task 2c: Single Fracture Chemical Oxidation Experiments.....	39
3.6.1 Oxidant Demand Testing on Colorado and Arizona Rocks.....	39
3.6.2 Chemical Oxidation Experiments in Rock Fractures .....	40
3.7. Task 3a: Fracture Network DNAPL Architecture and Dissolution .....	42
3.7.1 Fracture Network Characterization .....	42
3.7.2 DNAPL Architecture and Dissolution .....	42
3.8. Task 3b: Fracture Network Bioaugmentation Experiments.....	44
3.9. Task 3c: Fracture Network Chemical Oxidation Experiments .....	44
3.10. Analytical Methods.....	47

4. A CONCEPTUAL AND NUMERICAL MODEL TO DESCRIBE BIOAUGMENTATION FOR TREATMENT OF DNAPL SOURCES IN BEDROCK FRACTURES.....	49
5. RESULTS & DISCUSSION: .....	53
SINGLE FRACTURE DISSOLUTION EXPERIMENTS .....	53
5.1 Sorption.....	53
5.2 Matrix Porosity .....	53
5.3 Fracture Properties .....	54
5.4 DNAPL Architecture .....	57
5.5 DNAPL Dissolution.....	61
5.6 Conclusions – Discrete Fracture Dissolution Experiments .....	64
6. RESULTS & DISCUSSION: .....	65
SINGLE FRACTURE BIOAUGMENTATION EXPERIMENTS.....	65
6.1 Batch Experiments .....	65
6.2 Dechlorination Kinetics .....	66
6.3 General Observations during Bioaugmentation Experiments.....	66
6.4 Dechlorination Results.....	67
6.5 DNAPL Dissolution Enhancement .....	72
6.6 DHC Migration .....	74
6.7 Discrete Fracture Bioaugmentation Conclusions.....	74
7. RESULTS & DISCUSSION: .....	75
7.1 Verification Using Batch Data and Simulation .....	75
7.2 Model Calibration .....	76
7.3 Model Prediction.....	78
7.4 Sensitivity Analysis .....	80
7.4.1 Model response to variations in the yield coefficient .....	80
7.4.2 Model response to variations in the DHC maximum utilization rate constant (q).....	82
7.4.3 Bioaugmentation Model Conclusions .....	83
8. RESULTS & DISCUSSION: .....	84
SINGLE FRACTURE CHEMICAL OXIDATION EXPERIMENTS.....	84
8.1 Persulfate Experiments .....	84
8.2 Permanganate Experiment .....	86
8.3 Post-Oxidation Tracer Testing and DNAPL Recovery .....	87
8.4 PCE Oxidation Rates .....	89
8.5 Contact with Residual DNAPL.....	90
8.6 Discrete Fracture Chemical Oxidation Conclusions.....	91
9. RESULTS & DISCUSSION: .....	93
FRACTURE NETWORK DISSOLUTION .....	93
9.1 Rock Matrix Characterization.....	93
9.1.1 Diffusion of Solutes into Rock Matrix.....	93
9.1.2 Adsorption on to Rock.....	93
9.2 Fracture Network Properties .....	93
9.3 DNAPL Architecture in Fracture Networks .....	96
9.4 DNAPL Dissolution in Fracture Networks.....	99
9.5 Statistical Evaluation of DNAPL Dissolution in Fracture Networks .....	102



9.6 Fracture Network DNAPL Dissolution Conclusions.....	104
10. RESULTS & DISCUSSION: .....	105
FRACTURE NETWORK BIOAUGMENTATION .....	105
10.1 Fracture Network Bioaugmentation.....	105
11. RESULTS & DISCUSSION: .....	108
FRACTURE NETWORK CHEMICAL OXIDATION .....	108
11.1 Mass Removal during KISCO .....	108
11.2 Sequential KISCO experiment.....	113
11.3 Fracture Network Mass Removal Compared to Four Literature Studies .....	113
11.4 DNAPL Dissolution Mass Transfer during KISCO in Fracture Networks .....	116
11.5 Relating Changes in Interfacial Area to Dissolution in KISCO Fracture Networks .....	118
11.6 Experimental Mass Balances .....	120
11.7 Fracture Network Chemical Oxidation Conclusions .....	122
12. OVERALL CONCLUSIONS AND FINDINGS .....	124
13. IMPLICATIONS FOR FUTURE RESEARCH .....	129
14. REFERENCES .....	130
APPENDIX A: SUPPORTING DATA .....	141
A-1. CALCULATION OF BACK-PARTITIONING COEFFICIENT.....	141
A-2. PERSULFATE ELUTION DURING THE SINGLE FRACTURE CHEMICAL OXIDATION EXPERIMENTS.....	142
APPENDIX B: LIST OF PUBLICATIONS .....	143

## LIST OF FIGURES

Figure 2-1: Photomicrograph of amorphous manganese oxide.....	15
Figure 2-2: Conceptual Model.....	17
Figure 3-1: Experimental approach, broken down by task.....	19
Figure 3-2: Top face of Colorado sandstone.....	20
Figure 3-3: Inducing fracture.....	24
Figure 3-4: Fracture roughness.....	24
Figure 3-5a,b: Fracture edges.....	26
Figure 3-6: Effluent manifold.....	26
Figure 3-7: Completed discrete fracture system.....	27
Figure 3-8: Experimental design and schematic of fracture network.....	28
Figure 3-9: Experimental fracture apparatus .....	29
Figure 5-1: Water uptake for Colorado sandstone.....	53
Figure 5-2: Water uptake for Arizona sandstone.....	54
Figure 5-3: Bromide elution curves in rock C1.....	55
Figure 5-4: Bromide elution curves in rock A1.....	55
Figures 5-5a and 5-5b : Aperture ratio.....	58
Figure 5-6: PCE-water interfacial tension .....	60
Figure 5-7: Effluent dissolved PCE concentration relative to PCE.....	61
Figure 5-8: Lumped and intrinsic mass transfer coefficients.....	63
Figure 6-1: Batch Bioaugmentation experiment with PCE DNAPL.....	65
Figure 6-2: PCE dechlorination.....	66
Figure 6-3: Effluent concentrations of ethenes and DHC.....	67
Figure 6-4: Effluent concentrations of ethenes, chloride and DCH from rock A1.....	69
Figure 6-5: Effluent concentrations of ethenes, chloride and DCH from C1 .....	71
Figure 6-6: Effluent DHC levels.....	72
Figure 7-1: Model prediction for the batch results reported .....	75
Figure 7-2: Model calibration results .....	78
Figure 7-3: Model prediction results .....	79
Figure 7-4: Comparison of modeled and observed PCE Concentrations .....	80

Figure 7-5: Model response to a decrease in yield by 0.5 times for Experiment 3 .....	81
Figure 7-6: Model response to an increase in yield by 5 times for Experiment 3 .....	81
Figure 7-7: Model response a decrease in q by 0.5-times for Experiment 3 .....	82
Figure 7-8: Model response to an increase in q by 2 times for Experiment 3 .....	83
Figure 8-1: PCE DNAPL mass removal rates in the persulfate experiments .....	84
Figure 8-2: Dissolved effluent PCE concentrations for each persulfate experiment.....	86
Figure 8-3: PCE DNAPL mass removal rates in the permanganate experiment.....	87
Figure 8-4: SDBS and bromide elution curves .....	88
Figure 9-1: Aqueous phase PCE DNAPL concentration.....	101
Figure 10-1: Fracture network bioaugmentation .....	105
Figure 10-2: Chloride generation during the fracture network Bioaugmentation experiment ....	106
Figure 10-3: Chloride generation correlated to flow .....	107
Figure 11-1.(a.-c): Aqueous phase PCE concentrations prior to KISCO .....	109
Figure 11-2: PCE DNAPL mass removal rates during KISCO .....	111
Figure 11-3: Relationship between experimental mass of PCE.....	119
Figure A-2: : Persulfate effluent concentrations for the four persulfate experiments .....	142

## LIST OF TABLES

Table 3-1: Composition of artificial groundwater .....	23
Table 3-2: Physical properties of the two experimental networks.....	28
Table 3-3: Experimental design for the bedrock fracture Bioaugmentation experiments .....	37
Table 3-4: Experimental design for the bedrock fracture chemical oxidation.....	41
Table 3-5: Experimental conditions for each of the fracture network dissolution experiments ....	43
Table 3-6: Experimental variables for each of the fracture network KISCO experiments.....	45
Table 5-1: Fracture properties for each rock.....	56
Table 5-2: Residual saturation and DNAPL-water interfacial area .....	57
Table 5-3: Regressed values of R from CXTFIT.....	59
Table 7-1: Bioaugmentation parameters regressed from batch experiments.....	75
Table 7-2: Summary of numerical model parameters used for Experiment 3 .....	76
Table 7-3: Calibrated Monod parameters for Experiment 3 .....	78
Table 9-1: Summary of fracture network properties prior to DNAPL injection .....	94
Table 9-2: Summary of DNAPL dissolution results for each of the fracture networks .....	97
Table 9-3: Characteristics of fracture experiments.....	98
Table 9-4: Summary of Pearson-product moment correlations.....	103
Table 11-1: Experimental conditions of KISCO applications in the fracture network.....	110
Table 11-2: Mass removal comparison and post-KISCO conditions .....	112
Table 11-3: Summary of the mass removed .....	115
Table 11-4: Impacts of KISCO on fracture network dissolution.....	117



## LIST OF ACRONYMS

AGW	artificial groundwater
DCE	<i>cis</i> -1,2-dichloroethene
DHC	<i>Dehalococcoides</i>
DNAPL	dense non-aqueous phase liquid
EDTA	ethylenediaminetetraacetic acid
GC	gas chromatograph
HPLC	high-performance liquid chromatography
ISCO	<i>in situ</i> chemical oxidation
KISCO	permanganate <i>in situ</i> chemical oxidation
NOD	natural oxidant demand
PCE	tetrachloroethene
PTFE	polytetrafluoroethylene
SDBS	sodium dodecyl benzenesulfonate
TCE	trichloroethene
VC	vinyl chloride



## ABSTRACT

### Objectives

This project focused on measuring and evaluating the architecture, dissolution rate, and impact on groundwater quality of residually trapped tetrachloroethene (PCE) dense non-aqueous phase liquid (DNAPL) from discrete bedrock fractures and fracture networks. Treatment using both chemical oxidation and bioaugmentation also were evaluated in order to compare their relative effectiveness and identify potential limitations in fractured settings.

The specific objectives of this project were as follows:

- Determine residual DNAPL saturation, distribution, and interfacial area characteristics in various bedrock fractures and fracture networks;
- Measure and evaluate DNAPL-water interfacial area and dissolution rates as a function of DNAPL saturation within the fractures;
- Measure and evaluate DNAPL dissolution kinetics during chemical oxidation and bioaugmentation treatment in individual bedrock fractures and fracture networks;
- Identify potential limitations (e.g., fouling due to chemical precipitation or biological growth, DNAPL in dead-end fractures) of chemical oxidation and bioaugmentation in bedrock fractures;
- Evaluate the impact of partial DNAPL removal on groundwater quality;
- Develop and validate models to describe and predict DNAPL dissolution.

### Technical Approach

The overall approach for this project consisted of constructing laboratory fractures at two scales: a single fracture scale and a fracture network scale. Single fracture systems were created by inducing a single fracture in sandstone blocks. Fracture network systems, which contained multiple vertical and horizontal fractures, were constructed by assembling sandstone blocks; points of contact between the blocks defined the fracture network. Once constructed, the experimental fracture systems were contaminated with residual PCE DNAPL. Using conservative and interfacial tracers, the DNAPL architecture was assessed. In addition, dissolution experiments were performed to evaluate DNAPL dissolution kinetics. DNAPL dissolution also was evaluated during application of bioaugmentation, and during application of chemical oxidation using both permanganate and persulfate.

This project was a collaborative effort among Shaw Environmental, Inc. (Shaw), the Colorado School of Mines (CSM), and Auburn University. Shaw's efforts focused on overall project coordination, model development, and the single plane fracture systems. CSM efforts focused on



the fracture network experiments. Auburn focused on development of the DNAPL dissolution model in fracture systems.

## **Results**

Results from both the single fracture and fracture network experiments demonstrated that, compared to unconsolidated systems, residual DNAPL is not well contacted by migrating water. This resulted in reduced dissolution rates, and persistence of DNAPL sources within the bedrock fractures. While DNAPL dissolution during application of bioaugmentation was hindered by these intrinsic mass transfer limitations, results showed that bioaugmentation was effective at substantially enhancing the rate of DNAPL removal, despite dissolved PCE concentrations that were at or near solubility. Microbially-enhanced dechlorination rates during bioaugmentation were well described by a modified version of our previously developed bioaugmentation model. Results also showed that removal of a relatively small fraction of the DNAPL mass resulted in a large decrease in the dissolved PCE concentration.

Chemical oxidation was shown to be ineffective for treating DNAPL sources in bedrock fractures in both the single fracture and fracture network experiments. This ineffectiveness was due to decreases in the effective DNAPL-water interfacial area (as measured using interfacial tracers) that were likely caused by oxidation reaction byproducts.

## **Benefits**

This research demonstrated the difficulty in contacting DNAPL sources in fractured bedrock, and highlighted the importance of mass transfer processes even at the single fracture scale. However, results show that only partial removal of the DNAPL mass may be needed to sufficiently improve groundwater quality. In terms of evaluating treatment technologies, results of this study showed that bioaugmentation is a potentially effective remedial approach for DNAPL sources in fractured rock, and likely is a better long term option than either persulfate or permanganate oxidation.

## 1. OBJECTIVES

The overall goal of this proposed research is to evaluate the dissolution of residual DNAPLs in fractured geological settings during implementation of *in situ* chemical and biological remedial technologies, and to investigate the subsequent impact of incremental DNAPL removal on groundwater quality. Improved understanding regarding these phenomena are needed to facilitate the design and monitoring of remedial activities in bedrock source zones. Specifically, this proposal will address the following questions: 1) What is the rate of DNAPL dissolution during chemical oxidation and bioaugmentation, and how does that dissolution vary with time?; 2) How effectively can chemical oxidation or bioaugmentation amendments be delivered to DNAPL sources in bedrock fractures?; 3) What bedrock characteristics (e.g., aperture thickness, matrix diffusion, dead-end fractures) impact DNAPL removal?; and, 4) What are the impacts of fractional DNAPL removal on groundwater quality?

Several remedial technologies have been employed for treatment of DNAPL source areas in unconsolidated porous media, which have given rise to a multitude of studies to evaluate technology performance, to identify geologic conditions that can potentially impact treatment effectiveness, and to determine the result of source zone remediation on groundwater quality. Comparatively, only a limited number of remedial technologies have been evaluated for treatment of DNAPL source areas in fractured bedrock, with relatively little known about the performance, optimization, and limitations of these technologies in consolidated media.

DNAPL contamination is present in fractured bedrock at several DoD facilities. Improved understanding of the processes controlling the dissolution of subsurface DNAPL source zones is needed to assess contaminant impact on surrounding groundwater, predict the longevity and persistence of DNAPL sources, select the appropriate remedial technologies, effectively design and implement the selected *in situ* technologies, evaluate remedial performance, and estimate the time needed to remediate a DNAPL source zone. Such understanding requires improved insight into the *fundamental* pore scale processes impacting mass transfer between the DNAPL and groundwater phases, as well as the impacts of these pore scale processes on the aquifer scale.

The rate of DNAPL dissolution is typically controlled by interfacial mass transfer between the DNAPL and surrounding groundwater, especially during implementation of an *in situ* remediation technology that involves a relatively rapid reaction in the aqueous phase (e.g., chemical oxidation, bioaugmentation). *In situ* chemical oxidation and bioaugmentation are two technologies that are frequently implemented, thus understanding DNAPL dissolution processes during application of these technologies is of particular interest.

***Interfacial mass transfer between the DNAPL and surrounding groundwater is proportional to the DNAPL-water interfacial area. However, comprehensive studies have not been performed to evaluate and measure how pore scale DNAPL-water interfacial area varies as a function of fracture morphology and fracture saturation (mL DNAPL per mL fracture volume) as the DNAPL dissolves in fractured media.*** In addition, it is currently unclear how chemical oxidation and bioaugmentation technologies impact the effective DNAPL-water



interfacial area during source area treatment, and the efficiency of amendment delivery to the DNAPL-water interface in bedrock is not well understood. Without this information, it is difficult to predict the long term rate of DNAPL dissolution, estimate the dissolved contaminant flux emanating from the source area, determine the rate and dosage of remedial amendments, and determine the extent of the DNAPL mass that will need to be remediated to facilitate a final monitored natural attenuation remedy. Such tools would prove extremely useful at several DoD facilities in order to improve the quality of remedial or site assessment.

This project focused on measuring and evaluating the architecture, dissolution rate, and impact on groundwater quality of residually trapped tetrachloroethene (PCE) dense non-aqueous phase liquid (DNAPL) from discrete bedrock fractures and fracture networks. Treatment using both chemical oxidation and bioaugmentation also were evaluated in order to compare their relative effectiveness and identify potential limitations in fractured settings.

The specific objectives of this project were as follows:

- Determine residual DNAPL saturation, distribution, and interfacial area characteristics in various bedrock fractures and fracture networks;
- Measure and evaluate DNAPL-water interfacial area and dissolution rates as a function of DNAPL saturation within the fractures;
- Measure and evaluate DNAPL dissolution kinetics during chemical oxidation and bioaugmentation treatment in individual bedrock fractures and fracture networks;
- Identify potential limitations (e.g., fouling due to chemical precipitation or biological growth, DNAPL in dead-end fractures) of chemical oxidation and bioaugmentation in bedrock fractures;
- Evaluate the impact of partial DNAPL removal on groundwater quality;
- Develop and validate models to describe and predict DNAPL dissolution.

## 2. BACKGROUND

### 2.1 DNAPL Architecture and Dissolution

Groundwater contamination by dense non-aqueous phase liquids (DNAPLs) is a widespread environmental concern, and is a significant issue at many DoD facilities. Releases of chlorinated DNAPL compounds such as tetrachloroethene (PCE) may result in the downward migration of chlorinated solvents into fractured bedrock. DNAPL can become immobilized in bedrock fractures as a residual phase, where it can serve as a long-term contaminant source to groundwater. The subsequent rate of DNAPL dissolution into surrounding groundwater is controlled by interfacial mass transfer between the DNAPL and groundwater. This is especially true if groundwater velocities are high, as often is the case during implementation of a pump-and-treat remedial strategy, in fractured bedrock aquifers, and/or if there is a rapid reaction occurring near the DNAPL-water interface (e.g., *in situ* chemical oxidation). This mass transfer can be expressed by the following equation:

$$N = k a_i V (C_{\text{sat}} - C) \quad \text{Eq. 2-1}$$

where  $N$  is the rate of contaminant dissolution in surrounding groundwater (mg/sec),  $k$  is the mass transfer coefficient (cm/s),  $a_i$  is the DNAPL-water interfacial area per unit volume ( $\text{cm}^2/\text{cm}^3$ ),  $V$  is the unit volume of surrounding groundwater ( $\text{cm}^3$ ),  $C_{\text{sat}}$  is the DNAPL aqueous solubility ( $\text{mg}/\text{cm}^3$ ), and  $C$  is the measured (or, actual) groundwater concentration adjacent to the DNAPL ( $\text{mg}/\text{cm}^3$ ).

The key parameters needed to evaluate and predict interfacial mass transfer between DNAPL and water in fractured geological settings are still not well understood because fundamental understanding regarding the configuration (i.e., DNAPL-water interfacial area) of dissolving DNAPL in bedrock fractures is lacking. Theoretical predictions (1-4) and experimental measurements (5-9) of fluid-fluid interfacial areas and DNAPL dissolution have been performed for unconsolidated media. These studies have provided insight into DNAPL configuration and morphology in sands and soils. The referenced DNAPL dissolution studies have generally shown that dissolution flux is proportional to the DNAPL-water interfacial area.

While recent studies (9) have measured the interfacial area and developed correlations for predicting an interfacial mass transfer coefficient in unconsolidated media, there is a notable absence of any similar studies (simultaneously measuring interfacial area and DNAPL dissolution) that have been performed for bedrock or fractured systems. Dickson and Thomson (10) performed DNAPL dissolution experiments in fractures and developed a fracture dissolution model to simulate dissolution of DNAPL in bedrock fractures. They note that their model is sensitive to a morphology index, which represents the ratio of DNAPL-water interfacial area to DNAPL volume. Similarly, simulations performed by Detwiler et al. (11) have shown that dissolution of non-aqueous phases in fractures is not simply a function of entrapped saturation,



but also of the geometry of the entrapped phase (i.e., DNAPL-water interfacial area). Simulations performed by Rubin et al. (12) also confirm the need to understand the interfacial mass transfer coefficient for NAPL dissolution in fractured bedrock. Thus, these studies identify the need to measure and evaluate DNAPL-water interfacial area in bedrock fractures in order to evaluate and predict DNAPL dissolution. However, to the best of our knowledge, comprehensive studies have not been carried out to evaluate DNAPL-water interfacial area, DNAPL dissolution rates, and DNAPL architecture in fractured bedrock systems.

## 2.2 Bioaugmentation for Treatment of DNAPL Sources in Bedrock

Bioaugmentation for chlorinated ethenes typically involves the subsurface delivery of mixed anaerobic cultures that contain *Dehalococcoides* spp. (DHC) that can reductively dechlorinate the chlorinated ethenes; DHC are the only bacteria known to completely dechlorinate PCE and TCE (13). Bioaugmentation for treatment of tetrachloroethene (PCE) and trichloroethene (TCE) in groundwater has been successfully applied at numerous sites, including several DoD facilities. While several laboratory and field studies have demonstrated the effectiveness of bioaugmenting with DHC for treating dissolved phase PCE and TCE (14-17), the use of this approach for treating PCE or TCE when present as a dense non-aqueous phase liquid (DNAPL) has received far less attention. Because the overall value of addressing source area at chlorinated solvent sites, treatment of DNAPL source areas increasingly has become a focus at many contaminated sites (18-20). Batch and column studies have indicated that the presence of PCE DNAPL can have an inhibitory effect on the reductive dechlorination of PCE during bioaugmentation (21-23). Adamson et al. (22) noted the accumulation of TCE and *cis*-1,2-dichloroethene (DCE) in the DNAPL source zone, without further dechlorination to vinyl chloride (VC) or ethene until PCE concentrations decreased to approximately 10  $\mu\text{M}$ . One recent study has indicated that concentrations of dissolved PCE near saturation can permanently inactivate biomass (24).

Despite this apparent inhibitory effect of DNAPL on the reductive dechlorination of PCE, bioaugmentation has been shown to enhance the rate of PCE DNAPL dissolution in sand columns and flow cells by factors ranging from approximately 1.1 to 21 (23, 25-26). Enhancement rates were typically higher when the dissolved concentration of PCE was less than approximately 300  $\mu\text{M}$  (23, 26). Other factors shown to impact DNAPL dissolution enhancement and overall PCE dechlorination during bioaugmentation include microbial dechlorination kinetics, water velocity (which impacts residence time and shear stress), electron donor supply, bioclogging, pH, and DNAPL saturation and architecture (26-30). Becker and Seagren (28) also show that non-DHC partial dechlorinators can play an important role in DNAPL dissolution. Because PCE dechlorination products such as TCE or *cis*-1,2-dichloroethene (DCE) have solubilities that are substantially greater than PCE, partial PCE dechlorination can greatly enhance the overall rate of DNAPL dissolution.

While prior studies have provided insight into DNAPL dissolution processes during bioaugmentation in unconsolidated media, published studies that evaluate similar mechanistic processes of PCE DNAPL dissolution in fractured bedrock systems currently are lacking. Several recent experimental and theoretical studies have focused on evaluating abiotic DNAPL

dissolution in bedrock fracture systems (10, 31-32), and DNAPL dissolution in fractures during implementation of chemical oxidation (33). However, besides the research performed as part of this project, we are unaware of any published studies that evaluate bioaugmentation for treatment of DNAPL in fractured bedrock.

The distribution of microorganisms relative to the DNAPL will ultimately control the effective diffusion (or, transport) length between the contaminant and the reactant. DNAPL-water interfaces may also serve as sorptive sites for the microorganisms, thereby further impacting microbial transport and kinetics within the targeted region. These issues, although critical to DNAPL treatment via bioaugmentation in bedrock, have not been examined in sufficient detail.

### 2.3 Chemical Oxidation for Treatment of DNAPL Sources in Bedrock

Chemical oxidation for treatment of tetrachloroethene (PCE) and trichloroethene (TCE) in groundwater has been successfully applied at numerous sites. Permanganate and persulfate are among the oxidants that have been frequently used. Use of persulfate for treatment of PCE and TCE typically requires use of an activator to attain sufficient treatment rates, which may be in the form of heat, alkaline pH, or iron activation (34-39). While the reaction of these oxidants with chlorinated ethenes in the aqueous phase have been carefully examined, their effectiveness for treating PCE and TCE when present as a dense non-aqueous phase liquid (DNAPL) has received less attention. Several laboratory studies applying permanganate have shown that DNAPL mass removal rates quickly diminish long before DNAPL is completely removed due to mass transfer limitations (40-42). Field studies using permanganate to treat DNAPL sources have attained mixed results (43-47). The challenges associated with using permanganate to treat DNAPL sources has been attributed to the formation of  $\text{MnO}_2$  and/or carbon dioxide gas generation (42, 48-50). While the absence of  $\text{MnO}_2$  formation during persulfate reaction with chlorinated ethenes is a potential benefit (compared to permanganate oxidation), we are unaware of any published studies that examine DNAPL dissolution during persulfate oxidation.

The introduction of  $\text{KMnO}_4$  into the subsurface may exacerbate subsurface heterogeneities due to manganese oxides precipitation from the oxidation reaction. Two primary types of manganese oxides form during  $\text{KMnO}_4$  ISCO, amorphous particles /solids that result from the oxidation of aqueous phase contaminants and the solid film that results at the interface of DNAPL and  $\text{KMnO}_4$  (51). Figure 2-1 presents a photomicrograph comparison of the amorphous particles generated during the aqueous phase contaminant oxidation (left) and the platelets forming the interfacial film (right). The amount of manganese oxides particles that develop, grow, and potentially settle as a result of  $\text{KMnO}_4$  ISCO with organic contaminant reactions is a function of the particle size and concentration, the time allowed for particle development, and the impact of matrix conditions on the ability of particles to agglomerate (52).



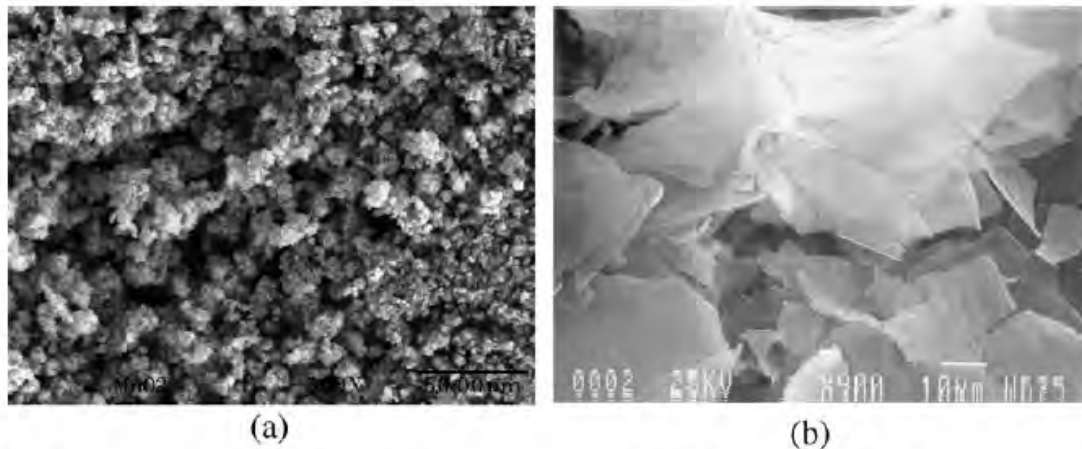


Fig. 8. (a) Photomicrograph of amorphous manganese oxide solids created from the chemical oxidation of aqueous phase TCE by  $\text{MnO}_4^-$ . Magnification= $\times 500$ . (b) Photomicrograph of manganese oxide film created during the chemical oxidation of  $\text{TCE}_{\text{DNAPL}}$  by  $\text{MnO}_4^-$ . Magnification= $\times 900$ .

**Figure 2-1.** (a) Photomicrograph of amorphous manganese oxide solids created from the chemical oxidation of aqueous phase TCE by  $\text{MnO}_4^-$ . Magnification= $\times 500$ . (b) Photomicrograph of manganese oxide film created during the chemical oxidation of NAPL phase TCE by  $\text{KMnO}_4$ . Magnification= $\times 900$  (51).

The formation of amorphous manganese oxide solids and/or the platelets in aqueous environments affect the effectiveness of remedial actions in two ways including: 1) changes to the hydraulic properties of the subsurface formation thereby affecting delivery of  $\text{KMnO}_4$  to the contaminated areas and 2) increasing the sorption potential for many co-contaminant metals found at sites contaminated with chlorinated organic compounds. Changes to the hydraulic properties of the subsurface are due to pore-clogging and reduction in formation permeability. Hydraulic alterations lead to changes and/or reductions in aqueous flow paths and velocities. Conversely, permeability reductions in and around a DNAPL source zone may be considered beneficial by reducing or blocking the flow through the DNAPL zone and effectively cutting off the of dissolved contaminant flux (50). Once  $\text{KMnO}_4$  ISCO reactions are complete, subsurface reactions continue to influence the long term fate and transport of manganese oxides.

Treatment of DNAPL sources in bedrock fractures using chemical oxidants poses additional challenges. In laboratory scale fractured sandstone blocks, the ratio of DNAPL-water interfacial area to residual DNAPL saturation was shown to be less in bedrock fractures than in corresponding sands; DNAPL-water mass transfer coefficients in discrete bedrock fractures also have been shown to be substantially less than in unconsolidated media (10, 32). These findings suggest that DNAPL chemical oxidation in bedrock fractures may occur more slowly than in unconsolidated media, thereby amplifying the adverse effects of product precipitate formation observed in the studies described in the previous paragraph. Consistent with this assessment,

Tunnicliffe and Thomson (33) showed that DNAPL dissolution enhancement was minimal and  $\text{MnO}_2$  precipitation altered the flow field in bench scale permanganate oxidation experiments in rock fractures. We are unaware of any other published studies examining the use of chemical oxidants for treatment of DNAPL sources in bedrock.

## 2.4 Fracture Network Processes

Research centered on fracture network transport behavior is often based in numerical model simulations of mixing at fracture intersections (53-56) or field-scale tracer tests (57-60). Keller et al. (61) obtained images of intersecting fractures in a granite rock core that demonstrated that fracture intersections are large aperture regions that may impact flow and contaminant transport. Wood et al. (62) showed similar impacts of fracture intersections in unsaturated flow experiments using limestone blocks.

Natural fractures usually constitute preferential conduits for propagation of solutes in rocks and discontinuous media (54). Pankow and Cherry (63) describe DNAPL movement in fractured geologic media as primarily controlled by the orientation and interconnection of the fractures. In contrast, Reynolds and Kueper (64) state that aperture is the most important factor controlling the migration rate of DNAPL through a single fracture since the authors relate an increase in fracture aperture from 15 to 50 micrometers results in an approximately 20-fold increase in the rate of migration. In reality, all these factors interplay to influence the migration of DNAPLs in fractured media. As described by Kueper and McWhorter (65), the time taken for a non-aqueous phase liquid to traverse a fractured aquitard is inversely proportional to the fracture aperture, the fracture dip from horizontal and the height of the pool collected above the aquitard. When DNAPL enters a fractured environment, it preferentially migrates through the larger aperture pathways controlled by capillary pressure, wettability, interfacial tension and relative permeability (63). The advancing DNAPL front and intersecting fractures will be only be invaded if the capillary pressure of the DNAPL-water system exceeds the entry pressure (65). The entry pressure of a DNAPL is seen to be directly proportional to the interfacial tension between the DNAPL and the water (65).

The movement of two mutually immiscible liquids through a rough-walled fracture is often considered to be analogous to the movement of these liquids through porous media, where the distribution of apertures within the fracture parallels the distribution of pores and pore throats in porous medium (65). However, Schwille and Pankow (66) investigated the spreading of low-concentration DNAPL solutions (2 grams/liter) in fractured rock and showed that the process of spreading in fractured media is much different than that in porous media and fractured media usually cannot be modeled as quasi-equivalent porous media. The difference between the findings of Kueper and McWhorter (65) and Schwille and Pankow (66) may be attributed to the greater density and viscosity of a DNAPL versus a dissolved DNAPL solution.

The net effect of diffusive properties is to temporarily retard of the apparent movement of the solute compared the aqueous phase (67) while simultaneously extending the longevity of the contaminant in the subsurface. Dual domain transport commonly refers the matrix diffusion

processes increasing the duration of a contaminant plume through storage of aqueous phase contaminant in the surrounding rock matrix.

**Matrix Diffusion:** Matrix diffusion is the process whereby solutes dissolved in groundwater diffuse into and out a rock matrix (68, 69). Forward diffusion occurs when dissolved contaminants move into the rock matrix from the open fracture while back diffusion is the process where dissolved contaminants will move out of the rock matrix and into water in the open fractures (69). Figure 2 illustrates the matrix diffusion (forward) that may potentially occur in fractured porous media, dependant on the physiochemical properties of the host rock.

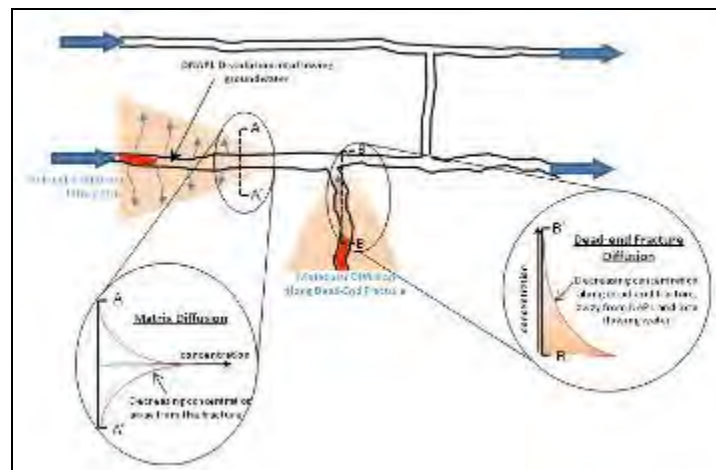


**Figure 2-2.** Recreated and modified from Kueper et al. (69). Schematic representing both dual domain transport scenarios A) Matrix diffusion (forward) and B) Dead-end fracture diffusion in fracture setting.

The characteristics affecting matrix diffusion processes include the physical properties of the rock and the chemical properties of the contaminant. Fick's First Law best describes the resultant aqueous chemical mass flux from the fracture into (or out of) the matrix (70):

$$J_D = -\phi_m D_e \frac{\partial C_w}{\partial x_i} \quad \text{Eq. 2-2}$$

where  $J_D$  is the effective diffusive flux ( $M/L^2/t$ ), in the  $x_i$  direction of flow ( $L$ ),  $\phi_m$  is the matrix porosity (-).  $D_e$  is the effective diffusion coefficient for the chemical solute in media ( $L^2/t$ ),  $C_w$  is the aqueous solute concentration and  $\partial C_w / \partial x_i$  ( $M/L^3/L$ ) is the chemical concentration gradient perpendicular to the flux. Conceptually, matrix diffusion is an important process impacting

longevity of the aqueous contaminant source zone but loss of contaminant mass to the matrix through diffusion does not significantly retard the migration rate of the actual DNAPL, particularly in the 50  $\mu\text{m}$  or greater aperture fractures (64).

Dual domain transport may also be observed in fracture setting where the contaminant is not stored in the matrix alone, but rather in fractures outside of the primary flow path (i.e., “dead-end” fractures). In natural fracture networks, dead-end fractures are not “dead” in terms of fluid flow but rather small pressure differences will create local flow cells that particles can advectively enter and will be delayed compared to particles not entering such low velocity zones. (71). Storage of solutes in these dead end fractures, create a situation where the contaminant reenters the primary flow path by back diffusion from the dead end fracture, as illustrated in Figure 2. The influence of dead end fracture volume on the field study by Berkowitz and Scher (72) found that dominant aspects of chemical (particle) transport in fracture networks—non-Gaussian propagation—result from subtle features of the steady flow-field distribution through the network. In analyzing fracture network solute transport, the presence of dead-end fractures may mimic dual-domain transport from matrix diffusion.

### 3. MATERIALS AND METHODS

#### 3.1 Overall Approach and Rationale

Our approach for assessing DNAPL architecture dissolution in fractured bedrock was to employ laboratory-scale fractures using well characterized fracture systems. Two types of fracture systems were studied. The first were single fracture systems. These single fracture systems consisted of a single horizontal fracture within a sandstone block, thus limiting flow and dissolution processes to a single plane. The second type of system studies were fracture networks. Fracture networks were constructed using several sandstone blocks. The horizontal and vertical planes where the blocks came together formed the fracture network. This network contained elements of a “real” fracture network, including fracture intersections, horizontal and vertical fracture planes, and dead end fractures. Once constructed, these fracture network (both the single fracture and fracture network) were used to evaluate DNAPL architecture and dissolution, as well as treatment effectiveness during application of bioaugmentation and chemical oxidation.

The overall approach for this project is outlined in Figure 3-1. Experiments consisted of laboratory fracture studies at both the single fracture scale, as well as the fracture network scale. Mathematical models were developed to describe DNAPL dissolution processes at both of these scales. Details of the methodologies for these approaches are provided in the following sections.

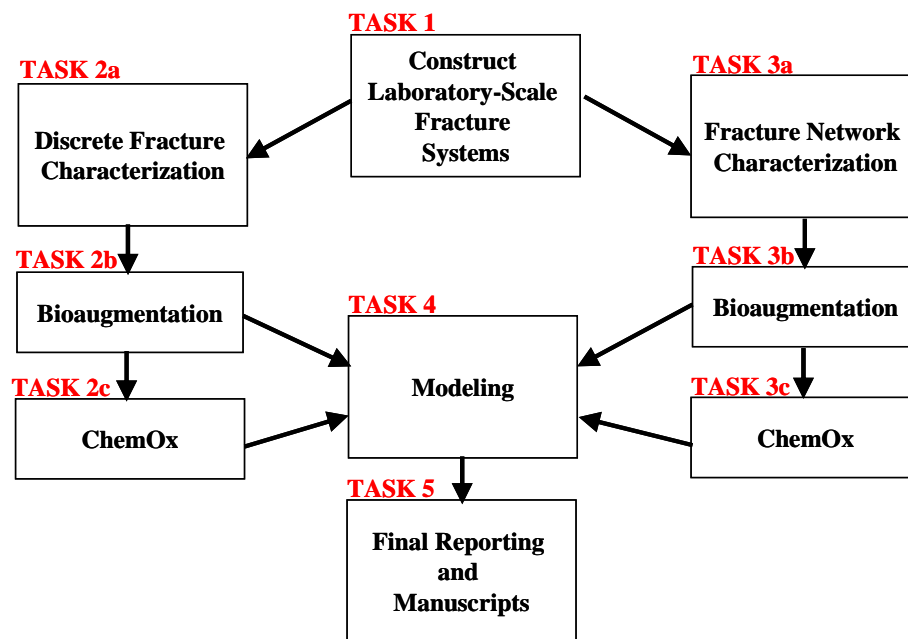


**Figure 3-1.** Experimental approach, broken down by task.



## 3.2 Task 1: Preparation of Fracture Systems – Single Fracture Systems

### 3.2.1 Rock Selection

Two rock-types were selected for this project. Based on discussions between Shaw and the Colorado School of Mines (CSM), the criteria for selection included the following: 1) relevance and representativeness of the rock type to DoD DNAPL-contaminated sites, 2) rock stability and inertness relative to the selected chemical (i.e., chemical oxidation) and biological treatments, 3) rock inertness with respect to the selected interfacial tracer (i.e., sodium dodecyl benzenesulfonate (SDBS)), 4) ease at which fractures could be induced in the rock, and 5) accessibility of the rock from local outcrops or commercial quarries.

Our initial intent was to use limestone as one of the model rock types. However, the limestone interacted very strongly with the SDBS interfacial tracer, and substantial dissolution of the rock appeared to occur in the aqueous system. Concerns also existed regarding potential interactions between the limestone matrix and the chemical oxidants. Based on this information, a Colorado sandstone was selected as the first model rock. This sandstone meets all the criteria listed in the preceding paragraph. Fractured sandstone systems are present at many DoD DNAPL sites, and preliminary testing showed that this rock was relatively inert to the SDBS tracer and was readily fractured along naturally occurring mineral planes. A quarry local to CSM carries ample quantities of this rock in pore-cut blocks that were suitable for the laboratory experiments. A picture of the Colorado sandstone block is shown in Figure 3-2.



**Figure 3-2.** Top face of Colorado sandstone. Rock dimensions are 29 cm x 29 cm x 5 cm.

An Arizona sandstone was selected for the second model rock type. This sandstone was selected based on the same criteria and rationale as the Colorado sandstone, and provides for a comparison between two different types of sandstone. As discussed in Section 3.2.3, the fracture plane/roughness of the Arizona sandstone appears much smoother than that of the Colorado sandstone. These differences in sandstone characteristics are expected to provide a meaningful contrast for the dissolution experiments.

### **3.2.2 Initial Rock Characterization**

Preliminary testing was performed on selected model rocks to evaluate their suitability for the laboratory experiments and to determine key chemical and physical parameters that will be needed to ultimately simulate DNAPL dissolution and contaminant fate and transport.

#### *Surfactant Sorption*

The anionic surfactant SDBS, which is used as an interfacial aqueous tracer to measure the DNAPL-water interfacial area in the fracture experiments, was tested to determine if significant interaction with the rock surfaces occurred. Substantial adsorption of the surfactant to the rock surface within the fracture would likely inhibit measurement of surfactant sorption to the DNAPL interfaces, thereby impeding our efforts to accurately measure DNAPL-water interfacial area.

Initial testing was performed to measure adsorption of the SDBS surfactant on to the rock surface. Testing was performed using the Colorado Sandstone, the Arizona sandstone, and a limestone. For each rock type, rocks were broken into small pieces of approximately 0.5 cm diameter, and 5 grams of rock were then placed into 40 mL glass serum bottles. Twenty mL of deionized water containing 20 mg/L SDBS were then added to each bottle. Controls, which contained the SDBS solution without rock, were also prepared. All bottles were capped with Teflon septa and allowed to equilibrate at room temperature for 24 hours. Bottles were periodically shaken. All treatments were prepared in duplicate.

After approximately 24 hours, the aqueous solution in each bottle was analyzed for SDBS. SDBS was analyzed using a GENESYS™ 2 UV-spectrophotometer. Aqueous samples were filtered with a 0.2 micron filter prior to analysis to limit the introduction of any fine particulates that were generated from the rock. SDBS displays an adsorption peak at a wavelength of approximately 235 nanometers. Adsorbance of SDBS in the rock-filled bottles was compared to that of the controls to determine the extent of SDBS sorption to the rock.

#### *Adsorption of Chlorinated Ethene to the Rock*

Quantification of the sorption of chlorinated ethenes onto the rocks is needed to calculate the retardation factors that will be needed to simulate contaminant fate and transport within the fracture systems. A preliminary adsorption experiment was performed to measure adsorption of PCE, TCE, and DCE onto the Colorado sandstone. Rocks were broken into small pieces of

approximately 1.0 cm-diameter, and 6 grams of rock were then placed into 60-mL glass serum bottles. Twenty mL of an artificial groundwater aqueous solution (AGW) (see Table 3-1 for groundwater composition) were then added to each bottle. Controls, which contained the AGW without rock, were also prepared. All bottles were capped with Teflon septa, and both treatments were prepared in triplicate. A glass Hamilton syringe was used to amend all bottles with 50  $\mu\text{L}$  of a stock solution containing PCE/TCE/DCE dissolved in methanol. Final aqueous concentrations were approximately 50 ppm of each solvent. Bottles were gently shaken for 24 hours at room temperature, and headspace samples (100  $\mu\text{L}$ ) were then analyzed on a Varian 3900 GC-FID (Palo Alto, CA).

#### *Adsorption of bromide*

Quantification of the sorption of the bromide tracer onto the rock is needed to verify that bromide will act as a conservative tracer in the fracture experiments. An adsorption experiment was performed to measure adsorption of bromide ( $\text{Br}^-$ ) onto the Colorado sandstone and the Arizona sandstone. Rocks were broken into small pieces of approximately 1.0 cm-diameter, and 6 grams of rock were then placed into 60-mL glass serum bottles. Twenty mL of an AGW solution amended with 100 ppm of bromide (as NaBr) were then added to each bottle. Controls, which contained the AGW without rock, were also prepared. All bottles were capped with Teflon septa, and both treatments were prepared in duplicate. Bottles were gently shaken for 72 hours at room temperature, and aqueous samples were filtered through a 0.2 micron filter and then analyzed via ion chromatography (Dionex DX-120, Sunnyvale, CA).

An additional set of sorption experiments also was performed by placing 1-cm thick slabs (approximately 45  $\text{cm}^2$ ) of each rock (the Colorado and Arizona sandstones) in bromide solutions for a minimum of two weeks. The rock slabs were then placed in bromide-free water, and the mass of bromide that diffused out of the rock was measured. The volume of water the rock was placed into was much greater than the volume of pore water in the rock.

#### *Matrix Porosity*

The porosity of the rock matrix could impact contaminant fate and transport during the laboratory column experiments, as slow diffusion into or out of this low permeability region can have lead to long-term “tailing” of contaminant concentrations. Rocks with large matrix porosities typically have an increased potential and capacity for such uptake compared to rocks with limited matrix porosity. Sandstones typically have a relatively large matrix porosity (approximately 10%) compared to other rock types (e.g., granite).

Matrix porosities were measured for the Colorado and Arizona sandstones. Small (approximately 11.5 cm x 5 cm x 1 cm and 13 cm x 9 cm x 1.5 cm, respectively) rectangular blocks were oven dried at 105° C for 1 to 4 days and subsequently weighed; successive measurements were collected until equilibrium conditions were attained. The blocks were then immersed in artificial groundwater (AGW) (see Table 3-1 for groundwater composition) to allow for infiltration of the water into the rock matrix. Water uptake into the rock was determined by



measuring the wet rock mass. Water uptake was monitored until equilibrium conditions were attained. Care was taken to removed and excess or pooled water on the rock surface prior to weighing.

**Table 3-1.** Composition of artificial groundwater used in the fracture experiments.

Component	Concentration (g/L)
MnSO <sub>4</sub> -H <sub>2</sub> O	0.001
NaSO <sub>4</sub>	0.18
NaCl	0.113
NaHCO <sub>3</sub>	0.04
HCl	pH to 6.5

### 3.2.3 Construction of Discrete Fractures

#### *Creation of Fractures*

Our initial strategy for inducing rock fractured was to implement the techniques used by Reitsma and Kueper (73), where tension fractures were induced using by applying a pressure along opposite edges of the rock, which mimics natural fractures formed by weathering or stress relief. However, their technique was applied to limestone. The sandstone blocks used in this project were not amenable to this technique because: 1) the sandstone rock was harder than the limestone and more difficult to fracture, and 2) the sandstone blocks did not contain a dominant fracture bedding plane, but rather consisted of secondary mineral bedding planes that were more difficult to fracture.

As a result, an alternate technique of fracturing was employed. A 4-inch wide masonry chisel was used to lightly tap along mineral bedding planes that were visible along the edges of the sandstone blocks. The blocks used were approximately 29 cm x 29 cm x 5 cm thick. This light tapping caused a distinct fracture to occur along a natural bedding plane. A picture of this procedure is shown in Figure 3-3. The interior of the split Colorado and Arizona sandstones, showing the “top” and “bottom” of the horizontal fracture plane, is shown in Figure 3-4. The fracture surface was very irregular, creating an uneven fracture surface that mimicked the naturally occurring bedding planes. The fracture procedure yielded similar results, but the fracture surface of the Arizona sandstone was visually observed to be less rough and more uniform than the Colorado sandstone. Two fracture blocks of each sandstone were constructed.



**Figure 3-3.** Inducing fractures. Fractures were induced along natural mineral bedding planes of the sandstone rocks.



**Figure 3-4.** Fracture roughness. Internal view of fractures for the Arizona and Colorado sandstones.

### *Fracture Block Design and Construction*

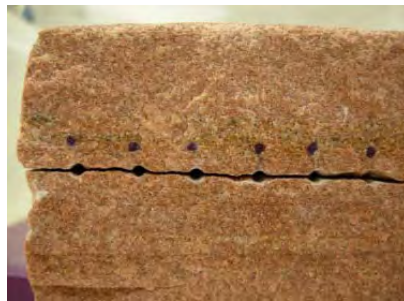
The dimensions of the Colorado sandstone fracture blocks are 29 cm x 29 cm x 5 cm. The two no-flow boundaries along the sides of the rock were sealed with Devcon plastic steel liquid (Grainger, Robbinsville, NJ). To prevent evaporative losses, the top and bottom of the rock were sealed with galvanized sheet metal that was attached with Devcon plastic steel putty (Grainger, Robbinsville, NJ). Small holes (5/64") were drilled along the influent and effluent sides of the fracture (Figure 3-5a). Pressurized air was applied to remove the resulting dust. The plastic, female luer fittings of stainless steel needles (16G) were removed prior to inserting the needle bevels into the holes. Care was taken to maintain the natural aperture width of the rock (i.e., the needles were not increasing the fracture aperture). Twelve needles were inserted into the influent side of the rock, and 28 needles were inserted into the effluent side. Flow simulations using MODFLOW and MT3DMS were performed to demonstrate that this number of injection points would create a uniform flow field (assuming the fracture consisted of a uniform permeability distribution).

The methods of Dickson and Thomson (10) for sealing the system were adapted for these experiments. Devcon plastic steel putty (Grainger, Robbinsville, NJ) was used to seal the space around the needles and along the length of the fracture (Figure 3-5b). Pieces of FEP-lined ultra-chemical resistant tygon tubing (1/16" i.d.) were attached to the blunt ends of the needles to serve as influent/effluent manifolds. Lengths were kept at a minimum to limit the volume in the lines<sup>1</sup>. The influent lines were connected through a series of tees to a peristaltic pump (Masterflex, Cole-Parmer Instrument Company, Chicago, IL). The effluent lines were connected to two Teflon manifolds (AutoMate Scientific, Berkeley, CA) in which the polypropylene tubing was replaced with truncated stainless steel needles (Figure 3-6). The manifolds were connected via Teflon tubing to a tee for sampling.

In order to achieve low flow rates (0.1 mL/min), a high precision/high pressure piston pump and a pressure gauge was installed along the influent line. All fracture blocks were leak-tested to verify the integrity of the sealant and fittings. Testing also was performed to verify that the pressure drop across each manifold was less than the pressure drop across the fracture, thereby confirming that the manifolds did not create any significant artificial flow effects within the fracture. A picture of the completed apparatus is shown in Figure 3-7.

---

<sup>1</sup> Based on the calculated volume of the fracture, the residence time in the effluent manifold was less than 10% of the residence time in the fracture.



a)



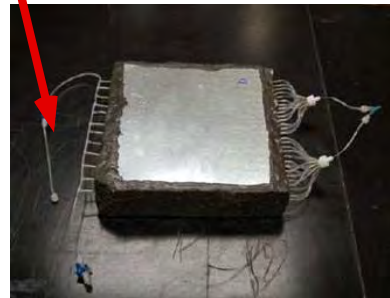
b)

**Figure 3-5a,b.** Fracture edges. Holes were drilled in the rock for insertion of stainless steel needles. The fracture was sealed on all sides with the plastic steel.



**Figure 3-6.** Effluent manifold, made of Teflon, used to connect the effluent lines. Stainless steel needles were used to connect this manifold to the Teflon-lines effluent lines.

Influent manifold connected  
to HPLC pump. Typical flow  
of 0.1 mL/min.



Effluent collection

**Figure 3-7.** Completed discrete fracture system. Two Colorado and two Arizona systems were constructed.

### 3.3 Task 1: Preparation of Fracture Systems – Fracture Networks

#### 3.3.1 Network Construction

Two fracture network systems, designated Network A and Network B, were used for the experiments and were based on discrete fractured rock assembly procedures previously performed (10, 32, 62). Figure 3-8 presents a general schematic of the internal fracture network arrangement used to conduct the bench-scale fracture network dissolution experiments and the characterization tests. The networks were constructed using a low porosity (less than 3.2%, as characterized by thin section analysis) Lyons Colorado Red Sandstone (CO Red). The CO Red was purchased as three individual, equally sized, saw-cut sandstone blocks from Camp Stone, Westminster, Colorado. Masonry tools were used to break each of the three CO Red blocks into three smaller blocks by inducing regularly spaced fractures along the horizontal mineral bedding planes (indicated by the dashed lines in Figure 3-8). Two fractures were induced in each large block; the induced fracture surfaces were rough (due to the natural mineralogy), mimicking natural fractures. The rough/chopped horizontal fractures were considered more realistic of a natural fracture network setting and were chosen for use along the primary flow pathway while the smooth/cut vertical fractures were oriented perpendicular to the primary flow paths. Table 3-2 summarizes the physical properties of the experimental networks described herein. The initial design arrangement was used for one 100-day dissolution experiment. Network A was used for dissolution experiments 2 through 4 and bioaugmentation experiment. Network B was used for dissolution experiments 5 through 8 and ISCO with  $\text{KMnO}_4$  experiments.

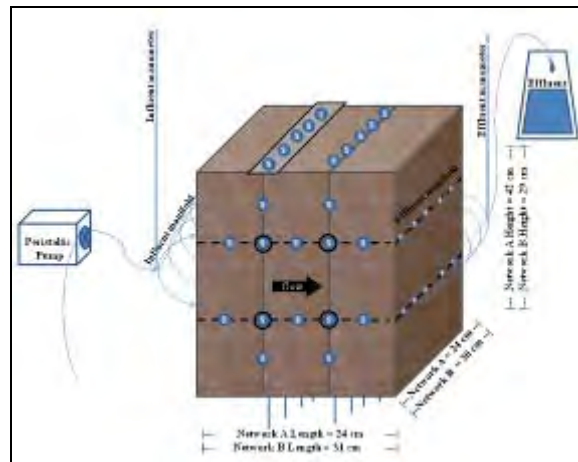


**Figure 3-8.** Experimental design and schematic of fracture network arrangement for Network A and Network B used for DNAPL dissolution experiments. Split faces are indicated by dashed line (horizontal) and saw cut faces are represented by the straight blue line (vertical). Black circles around side ports are locations represent the location of side ports for Network A, all ports labeled “S” refer to Network B. Network A Experiments 1 through 3 were injected through influent manifold. Top highlighted area (influent side) corresponds to DNAPL injection location for Network A Experiment 4 and Network B experiments.

**Table 3-2:** Physical properties of the two experimental networks.

	Network A	Network B
Length in Direction of Flow (cm)	24	31
Width perpendicular to flow (cm)	24	30
Height of experimental apparatus (cm)	42	29
Horizontal Fractures(#)	2	2
Vertical Fractures (#)	2	2
Matrix porosity (%)	3 ( $\pm 0.2\%$ )	3 ( $\pm 0.2\%$ )
Flow Ports (total #)	16 (8 influent/8 effluent)	20 (10 influent/10 effluent)
Sample Ports (#)	9 (4 on each side/0 top/1 bottom )	46 (14 on each side/10 top/8 bottom)



Early iterations of the experimental network design, encased the fractured CO Red blocks with 0.32 cm thick Teflon® lined aluminum sheets (aluminum encasement) on every side. Prior to assembly, eight 1.5 cm diameter holes were drilled into the influent and effluent sides of the encasement (16 holes total), four on each side of the top horizontal fracture and four on each side of the bottom horizontal fractures. Brass fittings were threaded into the holes and 0.32 cm i.d. viton tubing was attached to create the influent and effluent manifolds. Four 1.5 cm diameter holes were drilled on each side of the initial network design at the fracture intersections and perpendicular to the primary flow pathway. Four brass ball valves were threaded into each side (eight total) to enable spatial sampling at the fracture intersections. A 2.5 cm diameter drain port was drilled into the bottom encasement sheet, aligned with the influent side vertical fracture, and used to drain fluids from the network through a single ball valve threaded to the drain port. The aluminum encasement was assembled around the CO Red, sealed with Hercules® non-volatile organic compound plumbing caulk and compression was applied using standard clamps across two locations on each side and from top to bottom to minimize average network aperture. After the initial 100-day dissolution experiment (experiment 1), the fracture network was disassembled, cleaned, and reassembled as Network A.

#### *Network A*

Network A was encased with 0.32 cm thick Teflon® lined aluminum sheets (aluminum encasement) on every side and horizontal fractures were best-fit fracture surfaces. Influent, effluent and side sampling ports were created by 1.5 cm diameter holes drilled into the aluminum encasement. Influent and effluent ports were aligned with the two horizontal fracture surfaces and had brass fittings threaded into each hole that enabled attachment of 0.32 cm inner diameter (i.d.) viton tubing for effluent sampling. Prior to assembly, eight 1.5 cm diameter holes were drilled into the influent and effluent sides of the encasement (16 holes total), four on each side of the top horizontal fracture and four on each side of the bottom horizontal fractures. Brass fittings were threaded into the holes and 0.32 cm inner diameter (i.d.) viton tubing was attached to create the influent and effluent manifolds. Sampling ports on the sides of the experimental apparatus were also constructed. Four 1.5 cm diameter holes were drilled on each side of Network A at the fracture intersections and perpendicular to the primary flow pathway. Four brass ball valves were threaded into each side (eight total) to enable spatial sampling at the fracture intersections. A 2.5 cm diameter drain port was drilled into the bottom encasement sheet, aligned with the influent side vertical fracture, and used to drain fluids from the network through a single ball valve threaded to the drain port. The aluminum encasement was assembled around the CO Red, compression was then applied in all directions of the network using a standard clamp system to produce the smallest fracture apertures possible. Following compression the aluminum casing was sealed with Hercules® non-volatile organic compound plumbing caulk to create a closed system. Three-way valves and 0.3 cm i.d. viton tubing were attached in advance of the influent manifold and at the end of the effluent manifolds and used as a manometer to monitor pressure head across the network during the experiments. Brass ball valves were installed at the fracture

intersections perpendicular to the primary flow pathway into the sample ports drilled into each side of the experiment and one sample/drain port was installed on the bottom of the network. The interior of all ports (sample and flow) were comprised of chemically inert materials (primarily Teflon, brass or stainless steel) so as not to interact with the PCE in the experimental network. The aluminum encasement was assembled around the CO Red, compression was applied in all directions of the network using a standard clamp system to produce the smallest fracture apertures possible and then sealed with Hercules® non-volatile organic compound plumbing caulk. The assembled dimensions of Network A were 42 cm high, by 24 cm long by 24 cm wide, with each of the nine blocks sized 14 cm high, by 20 cm long by 8 cm wide.

#### *Network B*

Network B was constructed to produce fracture apertures and aperture distributions that were different and smaller than those in Network A and to produce equal distances between fracture intersections to assess the uniformity of DNAPL distribution within the network. Network B was constructed similarly to Network A with the following exceptions: the horizontal fracture surfaces were the matched induced fracture mates (producing a smaller average aperture than Network A) Devcon® plastic steel putty was used in place of the 0.32 cm thick aluminum casing; and flow and/or sample ports were created with 16- to 20-gauge stainless steel needles carefully emplaced at regular intervals across the horizontal and vertical fractures, respectively used as effluent flow ports and sample ports (Figure 4-1).

During assembly of Network B, aperture measurements were collected using a gap gauge at the locations where sample ports would planned for installation to quantify the aperture size in the vicinity of spatial sample locations. Measured aperture values were also used to compare to apertures calculated from tracer testing (discussed in detail in Section 3.4). Stainless steel needles were inserted into the fractures with care to ensure the needles did not increase the existing fracture apertures. The interior of all ports (sample and flow) were comprised of chemically inert materials (primarily Teflon or stainless steel) so as not to interact with the PCE in the experimental network. Needles in the two horizontal fractures of the influent and effluent sides of the network were used to construct influent and effluent manifolds. These manifolds were constructed of 0.16 cm i.d. Teflon tubing attached to the 16-gauge flow port needles using volatile organic compound free caulking and covered with Devcon® plastic steel putty. Three-way valves were attached in advance of the influent manifolds and at the end of the effluent manifolds to serve as manometers for measuring difference in hydraulic head (head) across the network during dissolution and tracer testing. Compression was applied in all directions of the network using a standard clamp system to produce the smallest fracture apertures possible. Once assembly was complete, the entire system was sealed in plastic steel putty to prevent evaporative losses from the network during the course of dissolution experiments. The assembled dimensions of Network B were 28 cm high by 31 cm long by 30 cm wide, with each of the nine blocks sized 9.3 cm high by 31 cm long by 10 cm wide.



### **3.3.2 Rock Characterization - Sorption**

SDBS is an anionic surfactant used as an interfacial aqueous tracer to measure the DNAPL-water interfacial area in the fracture network experiments. Sorption testing was conducted to determine if adsorption of the surfactant to the rock surface was observed since substantial adsorption would inhibit accurate measurement of surfactant sorption to the DNAPL interfaces and quantification of the DNAPL-water interfacial area. Five grams of CO Red sandstone, broken into small pieces of approximately 0.5 cm diameter, were placed in 50 mL glass flasks with 40 mL of 100 mg/L SDBS aqueous solution (the maximum concentration used in any interfacial area tracer test). The 50 mL sorption test flasks were sealed and agitated for 72 hours. Sorption tests were conducted in duplicate with controls that contained the SDBS solution without rock. At 72 hours, the aqueous solution in each bottle was analyzed for SDBS using a Beckman Coulter DU 800 UV/Vis Spectrophotometer at 225 nanometers. Prior to UV analysis, aqueous samples were filtered with a 0.2 micron filter prior to analysis to remove fine rock particulates. Absorbance of SDBS in the rock-filled bottles was compared to the controls to determine the extent of SDBS sorption to the rock. Results of the sorption testing revealed that sorption/interaction of SDBS, PCE, and bromide to the CO Red was negligible (<5% of solute mass sorbed to the rock) and will not be discussed further.

Bromide is a conservative tracer and the elution curve of bromide during tracer testing is used as a basis of comparison for SDBS to determine DNAPL-water interfacial area in the fracture network experiments. Sorption testing was conducted to determine if adsorption of the conservative tracer to the rock surface was observed since substantial adsorption would distort quantification of the DNAPL-water interfacial area. Five grams of CO Red sandstone, broken into small pieces of approximately 0.5 cm diameter, were placed in 50 mL glass flasks with 40 mL of 100 mg/L aqueous bromide solution (the maximum concentration used in any interfacial area tracer test). The 50 mL sorption test flasks were sealed and agitated for 72 hours. Sorption tests were conducted in duplicate with controls that contained the bromide solution without rock. At 72 hours, the aqueous solution in each bottle was analyzed for bromide using an ion-specific conductivity probe. Prior to ion analysis, aqueous samples were filtered with a 0.2 micron filter prior to analysis to remove fine rock particulates. Bromide results from the rock-filled bottles were compared to the controls to determine if bromide adsorbed to the CO Red rock.

Aqueous phase PCE sorption onto the CO Red rock was quantified to determine contaminant fate and transport within the fracture network. Two grams of the CO Red was broken into pieces of approximately 0.5 cm diameter and placed into 20-mL glass serum bottles with 20 mL of 38 mg/L aqueous PCE solution. Controls, which contained the PCE solution without rock, and initial PCE samples were collected from each bottle. All bottles were capped with Teflon septa, and both treatments were prepared in duplicate. Bottles were gently shaken for 72 hours at room temperature, and then 2 mL aqueous samples were collected from the serum bottles and analyzed on a Shimadzu GC-17A with FID for aqueous phase PCE concentrations.

### 3.3.3 Rock Characterization – Rock Matrix

#### Diffusion

The rate of maximum solute uptake into the rock matrix was estimated using a derivation of Fick's First law for steady state diffusion across a membrane where:

$$J = \frac{D_{\text{eff}}}{L} \times C \quad \text{Eq. 3-1}$$

$J$  is the diffusional flux ( $\text{mg}/\text{cm}^2/\text{sec}$ ),  $L$  is the experimental length ( $\text{cm}$ ), and  $C$  is the solute concentration ( $\text{mg}/\text{cm}^3$ ) and  $D_{\text{eff}}$  is the effective diffusion coefficient ( $\text{cm}^2/\text{sec}$ ).  $D_{\text{eff}}$  of the CO Red rock matrix was quantified as an empirical function of the CO Red porosity using a normalized diffusion coefficient (or diffusivity) as presented in Boving and Grathwol (74):

$$D_{\text{eff}} = \varepsilon^m D_{\text{aq}} \quad \text{Eq. 3-2}$$

where  $\varepsilon$  is the matrix porosity,  $m$  is an empirical exponent related to the tortuosity of the rock,  $D_{\text{aq}}$  represents the aqueous diffusion coefficient of the solute. The  $m$  value for CO Red was estimated as 1.64, based on its similar properties to the Fontainebleau Sandstone (72). The diffusional flux,  $J$ , in Equation 3-1 was then used to calculate the maximum diffusional flux into the rock matrix ( $M_u$ ):

$$M_u = J \times A \quad \text{Eq. 3-3}$$

where  $A$  is the surface area of the horizontal fractures ( $\text{cm}^2$ ) based on the known area of the cut sandstone blocks. The rate of solute migration through the fractures ( $M_f$ ) was then estimated using

$$M_f = Q \times C \quad \text{Eq. 3-4}$$

where  $Q$  is the volumetric flow rate ( $\text{cm}^3/\text{sec}$ ) and  $C$  is the solute concentration ( $\text{mg}/\text{cm}^3$ ). The ratio of Equation 3-3 to Equation 3-4 ( $M_u/M_f$ ), estimates the percentage of solute mass uptake by the matrix based on the solute mass available in the fracture network. A value less than 0.01 would indicate that the rate of solute mass uptake into the matrix is substantially less than the rate of mass migration through the fractures and can be neglected when assessing solute transport. A value greater than 0.1 would indicate the rate of solute mass uptake by the matrix needs to be considered when evaluating mass transport through the experimental system.

Matrix diffusion calculations for  $M_u/M_f$  provided a maximum value of  $10^{-4}$  for all solutes, indicating that mass uptake into the matrix is substantially less than the rate of mass migration through the fractures and can be neglected in evaluating solute transport in the fracture network experiments.

### *Natural Oxidant Demand*

Natural oxidant demand (NOD) tests for the CO Red in the presence of  $\text{KMnO}_4$  were conducted in 20 mL glass serum bottles using 2.5g crushed CO Red rock with 20 ml of 2 g/L (equivalent to 1.5 g/L  $\text{MnO}_4^-$ ) or 10 g/L (equivalent to 7.5 g/L  $\text{MnO}_4^-$ )  $\text{KMnO}_4$  solutions. Experiments were conducted in duplicate for each  $\text{KMnO}_4$  concentration and compared to two  $\text{KMnO}_4$  controls at the same concentrations that did not contain crushed CO Red. The NOD tests were conducted for 10 days.  $\text{KMnO}_4$  readings from each vial were collected every two days. NOD testing determined the oxidant demand of the CO Red was negligible, on average 0.07 % of the  $\text{KMnO}_4$  applied was consumed by CO Red NOD of the course of the each experiment.

NOD experiments at low pH (pH = 2.0) were conducted to identify if increased oxidant losses occurred due to low pH conditions. These tests were conducted similarly to the NOD testing except the 2 g/L and 10 g/L  $\text{KMnO}_4$  solutions were reduced to a pH of 2, the lowest pH expected during  $\text{KMnO}_4$  applications. The low pH tests were also conducted for a 10 day period and were compared to controls that did not contain CO Red. When not being sampled, the vials containing the oxidant solutions were stored in a non-transparent container to prevent breakdown of the oxidant by light. A slight (2%) increase in oxidant demand was observed in the controls and the experiments containing CO Red during the low pH tests. Based on the concentration of the  $\text{KMnO}_4$  delivered to the network, the increased oxidant demand was not expected to significantly impact oxidant deliver. Testing of  $\text{KMnO}_4$  consumption at the reduced pH determined a 3% increase in  $\text{KMnO}_4$  consumption was observed over the 10 day period (the longest  $\text{KMnO}_4$  application conducted was 10 days), which falls within the analytical limits of the visual spectrophotometer. Approximately 97% of the oxidant concentration at the 2.0 pH was maintained at the end of the 10 day, low pH NOD tests.

## **3.4. Task 2a: Single Fracture Characterization & Dissolution Experiments**

### ***3.4.1 Fracture Characterization without DNAPL Present***

Initial fracture-flow experiments were performed to characterize the fracture for each of the four rocks, which consisted of the two Colorado rocks (labeled C1 and C2) and the two Arizona rocks (labeled A1 and A2). All rocks were pre-wetted for several days to ensure that the rock matrix was water-saturated prior to initiating fracture flow experiments. The absence of any retardation of the SDBS tracer (which will sorb to the air-water interface (75)) during the initial tracer testing (prior to DNAPL addition, and described in the following paragraph) confirmed that significant trapped air was not adjacent to the water flow path. The pressure drop across each rock fracture at a given flow rate was measured using a manometer tube; this testing was performed to provide an estimate of fracture aperture.

Bromide and SDBS tracer tests were performed in the absence of PCE DNAPL for each rock. This testing was performed to: 1) verify that SDBS sorption to the rock surface was negligible, as evidenced by co-elution of the SDBS with the bromide, 2) evaluate potential

impacts of matrix diffusion on solute transport through the fracture plane, and 3) to evaluate fracture aperture and aperture distribution. Influent bromide and SDBS concentrations were 20 mg/L and 50 mg/L, respectively. Influent lines were pre-purged with tracer to limit residence time in the influent tubing prior to entry within the rock. Effluent samples were collected as a function of time and analyzed for each tracer. Tracer testing was typically performed at a flow rate of approximately 0.1 mL/min, although small (about a factor of two) changes in flow rate were used to confirm that the measured quantities were not a function of flow rate. Tracer experiments were performed at least in duplicate for each rock.

### ***3.4.2 Dissolution of Residual DNAPL***

Residual PCE was attained in the fractures by injecting two fracture volumes of PCE through the manifold at a flow rate of approximately 1.1 mL/min. To avoid contamination of the HPLC pump, a peristaltic pump (Masterflex) was used to inject the PCE DNAPL into the water-saturated fractures. In order to avoid contamination of the influent manifold used for the tracer experiments, a second manifold using FEP-lined tygon tubing was used during PCE injection. Displacement of water from the rock effluent typically ceased before one fracture volume of PCE had been delivered; water and PCE appeared to flow through the same effluent ports in each experiment. A minimum of two fracture volumes of artificial groundwater was then injected into the rock at a flow rate of approximately 1 mL/min to attain residual PCE saturation. PCE displacement from the rock typically ceased within one fracture volume of water injection. An additional two fracture volumes (minimum) of water were subsequently injected into the rock at a flow of approximately 10 mL/min (Capillary Number  $\sim 10^{-5}$ ) to ensure that all mobile PCE was displaced from the fracture and influent/effluent manifolds, and to ensure that PCE would not be mobilized during the dissolution experiments.

The residual PCE volume for each experiment was measured volumetrically as the difference between the PCE volume injected into the rocks and the total volume of PCE DNAPL that was recovered from the effluent after each post-PCE water flood; only separate-phase PCE was considered, as the volume of dissolved PCE was insignificant compared to the non-aqueous phase volume. Evaluation of alternate PCE flooding sequences were not performed in this study, thus results are limited to the PCE saturation history examined in these experiments.

After attaining residual PCE saturation (defined as residual PCE volume divided by the fracture volume) for each rock, bromide and SDBS tracer tests (0.1 mL/min flow rate) were repeated for each rock. Following the tracer testing, PCE dissolution kinetics were evaluated by measuring the effluent PCE concentrations as a function of flow rate (ranging from approximately 0.1 to 3 mL/min). To ensure equilibrium conditions, a minimum of two fracture volumes of water (without SDBS) at each tested dissolution flow rate were allowed to flow through the rock before an effluent concentration was measured. Because of the relatively low solubility of PCE, PCE mass removal during the dissolution testing did not result in a significant reduction in the residual PCE DNAPL mass (<5%).

At the conclusion of the experiment, several fracture volumes of ethanol were injected into the fractures to displace and dissolve the residual PCE. PCE concentrations in the effluent ethanol solution were measured to determine the mass of PCE DNAPL in the fractures, and to verify that the DNAPL had been removed prior to beginning additional experiments. Any DNAPL free-product that eluted during the co-solvent flooding also was included in the overall DNAPL mass balance.

### 3.4.3 Determination of DNAPL-Water Interfacial Area

Bromide and SDBS tracer testing, as described in the previous section, were performed both with and without DNAPL present in the fractures. These tests were performed to 1) evaluate any changes in flow/dispersion due to entrapment of the residual PCE, and 2) provide a measurement of the effective DNAPL-water interfacial area.

Retardation factors for the SDBS relative to the bromide were calculated using CXTFIT, and assuming a single domain equilibrium model. The DNAPL-water interfacial area, defined as the DNAPL-water area divided by the fracture volume, was calculated using the regressed retardation factor and by applying the Gibbs Adsorption Equation as follows

$$\Gamma = -\frac{MW}{RT} \frac{d\gamma}{d \ln C} = -\frac{MW}{RT} \frac{d\gamma}{dC} C \quad \text{Eq. 3-5}$$

where

$\Gamma$  = mass of surfactant sorbed at interface per unit area [ $\text{kg/m}^2$ ]

$R$  = gas constant [ $\text{mJ/mol K}$ ]

$T$  = temperature [ $\text{K}$ ]

$\gamma$  = interfacial tension between DNAPL and water [ $\text{mN/m}$ ]

$MW$  = surfactant molecular weight [ $\text{kg/mol}$ ]

$C$  = aqueous phase surfactant concentration [ $\text{kg/m}^3$ ]

And the following expression for the retardation factor:

$$R = 1 + a\Gamma/C_0 \quad \text{Eq. 3-6}$$

where  $a$  is the PCE-water interfacial area ( $\text{cm}^2/\text{cm}^3$  fracture volume), and  $C_0$  is the influent SDBS aqueous concentration. The value of  $\Gamma$  was determined by taking the derivative of the curve relating SDBS aqueous concentration to the PCE-water interfacial area.



### 3.5. Task 2b: Single Fracture Bioaugmentation Experiments

Experiments were performed using the four single fracture systems (A1, A2, C1, and C2) prepared with residual PCE DNAPL as described in Section 3.2.3. The objective of these experiments was to measure and assess the extent of microbially enhanced reductive dechlorination that occurred in the fractures, and to measure the extent of DNAPL dissolution enhancement that occurred as a result of the bioaugmentation treatment. In addition to the fracture experiments, an initial set of batch experiments was performed to serve as a baseline for comparison.

For all bioaugmentation experiments, Shaw's commercially available SDC-9 culture was used (76). The SDC-9 culture was isolated by enrichment culturing of aquifer samples from a southern California site. The culture contains at least two *Dehalococcoides* (DHC)-type organisms as determined by denaturing gradient gel electrophoresis (Microbial Insights, Knoxville, TN) (data not presented), and it is able to respire PCE, TCE, DCE and VC. The role of the individual DHC strains in dehalorespiration of these compounds, and the identity of lactate fermenting strains in the culture, have not been determined.

#### 3.5.1 Batch Bioaugmentation Experiments

Batch reactor experiments were performed to evaluate PCE dechlorination kinetics by DHC in the presence of PCE DNAPL. Experiments were performed by adding 6 L of artificial groundwater to each of two nitrogen sparged 6.5-L autoclavable bioreactors (Applicon, Inc., Foster City, CA). Approximately 10 mL of PCE was added to each reactor. This amount of PCE was sufficient to saturate the overlying aqueous solution, and maintain the presence of undissolved DNAPL throughout the duration of the experiment. Each reactor also was amended with sodium lactate (final concentration of 1,000 mg/L), yeast extract (final concentration of 300 mg/L), and DHC ( $10^9$  cell/L). The reactors were continuously mixed (250 rpm) and maintained at room temperature ( $\sim 21$  °C). The reactors were operated for 100 days, with periodic sampling for chlorinated ethenes, reduced gases, anions, and volatile fatty acids. For anions and volatile fatty acids, 1 mL aqueous samples were collected and filtered ( $0.25\ \mu\text{m}$ ) prior to analysis. For chlorinated ethenes and reduced gases, 5 mL aqueous samples were collected, preserved with acid, and equilibrated in a 14 mL glass serum bottle (with septa) prior to headspace analysis.

An additional batch experiment was performed similar to those described by Schaefer et al. (17) to evaluate microbial PCE dechlorination at elevated (near the aqueous PCE solubility) dissolved concentrations, but in the absence of DNAPL. Glass serum bottles (13 mL) with Teflon-lined rubber septa were prepared in duplicate with 13 mL artificial groundwater and dissolved PCE (final concentration of approximately 0.95 mM). The bottles were inoculated with bacteria to attain a final concentration of approximately  $5 \times 10^{11}$  DHC/L. Sodium lactate was added for a final concentration of 1,000 mg/L. A parallel set of controls were prepared without bacteria or lactate. Periodic sampling for chlorinated ethenes and reduced gases was performed.

### 3.5.2 Fracture Bioaugmentation Experiments

Bioaugmentation experiments on the fractured sandstones were performed after residual PCE DNAPL saturation was attained in the rocks, as described in Section 3.4.2. The seven sandstone bioaugmentation experiments are summarized in Table 3-3.

**Table 3-3.** Experimental design for the bedrock fracture bioaugmentation experiments. Flow velocity is calculated by dividing the influent volumetric flow rate by the fracture aperture (calculated by bromide tracers), the fracture width (29 cm), and the water-filled porosity. Dissolution enhancement factors were calculated at the end of the experiment, or the end of electron donor addition.

Experiment	Rock	DHC Inoculation (cells DHC)	Flow Velocity (cm/min)	Dissolution Enhancement Factor (Eq. 6-1)
1	A1	3 x 10 <sup>6</sup> (day 0) 8 x 10 <sup>8</sup> (day 91)	0.10	5.0
2	A2	3 x 10 <sup>6</sup> (day 0) 8 x 10 <sup>8</sup> (day 91)	0.062	1.1
3	A1	4 x 10 <sup>8</sup>	0.10 (decreased to 0.025 on day 13)	3.5
4	A2	4 x 10 <sup>8</sup>	0.062 (decreased to 0.015 on day 13)	3.4
5	C1	2 x 10 <sup>9</sup>	0.11 (decreased to 0.022 on day 37)	1.4
6	C2	2 x 10 <sup>9</sup> 2 x 10 <sup>11</sup> (day 58)	0.11 (decreased to 0.022 on day 37)	1.3
7	C1	4 x 10 <sup>8</sup>	0.044 (increased to 0.22 on day 29)	Not Calculated

After attaining residual DNAPL saturation, the influent artificial groundwater was amended with 500 mg/L sodium lactate, 300 mg/L yeast extract, and 200 mg/L diammonium phosphate. The artificial groundwater solution used in the bioaugmentation experiments was prepared in an anaerobic chamber (Coy Laboratory Products, Inc., Model AALC) and transferred to Tedlar bags with single polypropylene fittings (SKC, Inc.) to serve as influent reservoirs for the fractures. The Tedlar bags were connected to a Whatman filter device (Polycap 36 HD disposable filter capsule, MAPP filter media with polypropylene housing, 10 µm pore size) with Viton tubing and



delivered to the fractured rocks at the selected flow rates (0.02 to 0.2 cm<sup>3</sup>/min) using piston driven high performance metering pumps. Resultant ground water velocities in the fractures were within ranges observed under natural conditions in conductive bedrock fractures (58, 77).

The fracture was flushed with the prepared anaerobic solution for a minimum of two days, after which bioaugmentation using the DHC-containing SDC-9 culture was performed. Five milliliters of the desired inoculation dosage was delivered to the fractures via the influent manifold using a syringe pump at a flow rate of 0.1 mL/min. After the DHC inoculation, delivery of the lactate/yeast extract/diammonium phosphate solution from the Tedlar bags recommenced.

The effluent artificial groundwater was drip-collected in a 10 mL plastic tube for analysis of pH, anions, DHC, and volatile fatty acids. This collection process limited any further reductive dechlorination by exposing the DHC to atmospheric air (76). Lack of additional dechlorination during sample collection and storage was verified by analyzing for chloride at 1, 2, and 4 days and observing no increasing trend in chloride concentration.

For analysis of chlorinated ethenes and reduced gases in the effluent, effluent lines from the fracture effluent manifold were connected to a 3 mL sample vial that was crimp sealed with Teflon-lined butyl rubber septa. The sample vials were configured so the effluent exited approximately 1 cm above the fracture to prevent gravity drainage of liquid from the fractures. Effluent flowed through the trap and exited via a 20 gauge needle (Figure 3-9). The sample vial was amended with 15 µL of 18% hydrochloric acid approximately 30 minutes prior to collection to maintain the pH less than 2, thereby inhibiting the dechlorination activity of the DHC (22). Contents of the vials were then transferred to 5 mL glass vials with Teflon-lined septum screw caps (containing an additional 15 µL of 18% hydrochloric acid) for headspace analysis. Parallel testing was performed to ensure that this sample collection method did not result in any appreciable volatilization losses. Fractures were flushed sequentially with ethanol, base (0.1 N NaOH), acid (0.1 N H<sub>2</sub>SO<sub>4</sub>), and artificial groundwater after each experiment to remove remaining DNAPL and biomass.





**Figure 3-9.** Experimental fracture apparatus constructed from sandstone blocks (influent manifold on the left, and effluent manifold on the right). Each rock was approximately 29 cm long (L) x 29 cm wide (W).

Experiment 7 (C1) was performed to evaluate the impacts of flow rate on effluent DHC concentrations, and to verify that injected DHC were not rapidly eluting through the fracture prior to collecting effluent samples. All fracture effluent was continuously containerized in glass beakers over a 10 day period following inoculation. The flow rate was increased after 29 days to assess the impact of velocity on DHC elution. Effluent monitoring of chlorinated ethenes, reduced gases, anions, or volatile fatty acids was not performed for this experiment.

### 3.6. Task 2c: Single Fracture Chemical Oxidation Experiments

#### 3.6.1 Oxidant Demand Testing on Colorado and Arizona Rocks

Batch experiments were performed in order to determine the oxidant demand of the Arizona and Colorado sandstones. Batch experiments to measure rock oxidant demand were conducted in duplicate for each sandstone using polyethylene sample bottles containing 200mL of artificial groundwater, 200g of crushed rock (approximate particle size of 10 to 30 mm), and amended with either 10,000mg/L of potassium permanganate or 20,000mg/L of sodium persulfate with 150mg/L of ferrous iron ethylenediaminetetraacetic acid (Fe-EDTA) activator. Duplicate controls without rock material also were prepared. The bottles were incubated at room temperature ( $21.5 \pm 0.4$  °C), periodically shaken over a two day period, then sampled to measure oxidant concentration in the aqueous phase.

An additional permanganate batch experiment was performed using crushed rock, artificial groundwater with the pH adjusted to 3, and 10,000 mg/L permanganate. This test was performed



to determine if the rock oxidant demand would increase if the pH was reduced to 3 (as discussed in Section 8, the pH of the effluent solution was near 3, likely due to the oxidation reactions). A control was prepared that contained no rock. Bottles were prepared in duplicate. After 48 hours of incubation, the permanganate concentration was measured in each sample.

Persulfate concentrations were measured using a 3mL sample aliquot. The 3 mL sample aliquot was placed in a 50mL Erlenmeyer flask and combined with 100mg of KI. The solution was titrated using a 0.01N standardized sodium thiosulfate solution from a calibrated burette to the flask. When the flask color turned a faint yellow 3mLs of starch solution were added to turn the solution dark blue. The titration was continued until the blue color disappeared. The volume of sodium thiosulfate was used to calculate the concentration of persulfate in the sample. Samples amended with rock were compared to controls (no rock added) to calculate the oxidant demand of the rock. Aqueous permanganate concentration was calculated using a Thermo Scientific Genesys 2 UV-spectrophotometer at a wavelength of approximately 525nm; permanganate oxidant demand was calculated by measuring the difference between the rock-amended samples and the controls.

### ***3.6.2 Chemical Oxidation Experiments in Rock Fractures***

Chemical oxidation experiments on the single fractured sandstones were performed after residual PCE DNAPL saturation was attained in the rocks. Methodology for attaining residual DNAPL saturation in the rocks are described in Section 3.4.2. A total of five chemical oxidation experiments were performed in the residual PCE-containing fractures. These experiments are described in Table 3-4. The oxidant solutions was stored in a 1 L glass reservoir that was shielded from ambient light. For the persulfate experiments, the Fe-EDTA solution was stored in a separate reservoir to prevent reaction with the persulfate. The reagents in the reservoir bottles were delivered to the fractured rocks at approximately 0.1 cm<sup>3</sup>/min total flow using piston driven high performance metering pumps. Resultant ground water velocities in the fractures were within ranges observed under natural conditions in conductive bedrock fractures (58, 77). Delivery of the oxidant was continuous during the duration of the experiments.

**Table 3-4.** Experimental design for the bedrock fracture chemical oxidation experiments. Flow velocity is calculated by dividing the influent volumetric flow rate by the fracture aperture (calculated by bromide tracers), the fracture width (29 cm), and the water-filled porosity. Fe-EDTA concentrations are provided on an Fe basis.

Experiment	Rock	Oxidant	Influent Oxidant Concentration (mg/L)	Activation	Velocity (cm/s)	DNAPL Mass Oxidized (mg)
1	A1	persulfate	9,500	1,000 mg/L Fe-EDTA	0.10	1,240
2	A1	persulfate	8,700	500 mg/L Fe-EDTA	0.10	550
3	C2	persulfate	9,500	500 mg/L Fe-EDTA	0.11	980
4	C2	persulfate	10,000	Alkaline (pH≥12)	0.11	120
5	A2	permanganate	10,400	none	0.062	1,100

For analysis of PCE, effluent lines from the fracture effluent manifold were connected to a 3 mL sample vial that was crimp sealed with Teflon-lined butyl rubber septa. The sample vials were configured so the effluent exited approximately 1 cm above the fracture to prevent gravity drainage of liquid from the fractures. Effluent flowed through the trap and exited via a 20 gauge needle. For the permanganate experiments, the sample vial was amended with sodium thiosulfate (40 mM) to inhibit any further oxidation reactions. For the persulfate experiments, samples were refrigerated at 4 °C to inhibit further oxidation reactions. Contents of the vials were then transferred to 5 mL glass vials with Teflon-lined septum screw caps for headspace analysis. Vials were equilibrated to room temperature prior to analysis.

For all other effluent analyses (pH, anions, permanganate or persulfate, and iron), the effluent artificial groundwater was drip-collected in a 10 mL plastic tube. The plastic tubes were amended with sodium thiosulfate to quench the permanganate reactions (except for when permanganate itself was being analyzed); the tubes were refrigerated at 4 °C to quench the persulfate reactions.

At the end of the oxidation experiments, if the fracture had not become plugged, a tracer test was performed. These tracer tests were performed using a conservative tracer (sodium bromide) and an interfacial tracer (SDBS). The details of these tracer tests, which consisted of a step input of bromide (25 mg/L) and SDBS (50 mg/L) in the artificial groundwater, and subsequent measurement of the elution of these compounds as a function of time, have been previously described (Section 3.4). Tracer testing was performed at 1 to 2-times the velocities shown in Table 3-4. These tracer tests were used to assess any changes in the fracture flow field and effective DNAPL-water interfacial area that may have occurred as a result of the oxidation

treatment. After completing the tracer testing, fractures were flushed sequentially with artificial groundwater, ethanol, and artificial groundwater after each experiment to remove the remaining DNAPL.

### **3.7. Task 3a: Fracture Network DNAPL Architecture and Dissolution**

#### ***3.7.1 Fracture Network Characterization***

Conservative tracer tests were conducted in the AGW saturated fracture network using bromide and SDBS before DNAPL was introduced to evaluate the flow path fracture volume and the aperture characteristic of the fracture network. Bromide is a conservative tracer and SDBS behaves conservatively in the absence of DNAPL or air (78, 79). The experimental fracture networks were saturated for several days with AGW prior to the onset of tracer testing. Water-saturation of the network was obtained by filling the networks with AGW for three days (minimum), then alternating flow between high volume and low volume discharge. Air was removed from the experimental networks by venting through all sample ports during flowing conditions. Once PCE DNAPL was introduced, interfacial area tracer tests were conducted to quantify the DNAPL-water interfacial area at various stages of the dissolution experiments. SDBS sorbs to the DNAPL-water interface and has been used to measure DNAPL-water interfacial area in several previous studies (32, 78, 79, 80, 81). All tracer tests were conducted as one fracture volume pulses using a 50 mg/L tracer solution of bromide and SDBS injected at experimental velocities reported in Table 3-5 (Section 3.7.2). Effluent solute concentrations were measured every five to ten minutes (dependant on experimental velocity) and all experiments were performed in duplicate. Velocity and pressure head measurements were regularly collected during all tracer tests. Pressure head measurements were determined based on the difference between influent and effluent manometer readings (cm).

#### ***3.7.2 DNAPL Architecture and Dissolution***

After characterizing the network in the absence of DNAPL, eight DNAPL dissolution experiments (three in Network A and four in Network B) were conducted. Experimental conditions for the DNAPL dissolution experiments are summarized in Table 3-5. In Network A, three experiments involving DNAPL flooded through the influent and one experiment involving DNAPL emplaced from the top ports, along the influent side were conducted. Network B experiments involved DNAPL emplaced from the top influent side ports. Influent DNAPL flooding was delivered via injection of 800 ml of PCE DNAPL through the influent manifold at the experimental linear velocities reported in Table 3-5. For the top, PCE DNAPL injection, 100 ml of was delivered by injection into the influent vertical fractures through the sample ports using a 25 ml glass syringe with 15 cm needle at approximately 10 ml/min.

**Table 3-5. Experimental conditions for each of the fracture network dissolution experiments. Standard error reported in parentheses as applicable.**

Network	Experiment	DNAPL emplaced	Aqueous Dissolution Testing (days)	CXTFIT Linear velocity (cm/min)	$S_N$	$K_L$ ( $\text{min}^{-1}$ )	$a_i$ ( $\text{cm}^2/\text{cm}^3$ )
A	1	Influent	5	0.6 (0.04) <sup>a</sup>	0.14	0.03 ( $\pm 0.01$ )	111 ( $\pm 6$ )
A	2	Influent	5	1.3	0.46	0.09	169
A	3	Influent	5	1.0	0.27	0.03	178
A	4	Top	100	0.3	0.13	0.02	20
B	5	Top	60	1.5 (0.3)	0.32	0.02 ( $\pm 0.01$ )	39 ( $\pm 10$ )
B	6	Top	35	1.6	0.16	0.01 ( $\pm 0.01$ )	10
B	7	Top	12	0.7 (0.1)	0.27	0.02 ( $\pm 0.01$ )	29 ( $\pm 7$ )
B	8	Top	13	1.2 (0.2)	0.19	0.02 ( $\pm 0.01$ )	18 ( $\pm 1$ )

<sup>a</sup> Standard Error reported in parenthesis for averaged values.

Following DNAPL delivery, the AGW linear velocity was increased to at least five times the experimental linear velocities reported in Table 3-5 for a minimum of ten fracture volumes to displace all mobile PCE DNAPL and attain residual saturation. The effluent was continuously captured into the glass filtering flask to measure the volume of DNAPL that eluted through the fractures. Residual DNAPL saturation was assumed to be achieved when the AGW effluent contained no PCE DNAPL for at least four fracture volumes at the increased flow rate. The volume of PCE NAPL trapped in the network was determined as the difference between PCE DNAPL volume delivered into the network and the volume recovered. The volume of PCE DNAPL trapped was then divided by the total fracture volume of the experimental network to determine the residual DNAPL saturation ( $S_N$ ). The  $S_N$  in the fracture setting was unlike residual saturation in commonly observed in porous media experiments. The  $S_N$  exists as pooled areas of DNAPL in the larger aperture regions in the fracture network. Once residual saturation was established, flow was reduced to the original experimental aqueous flow conditions and sequential pulsed bromide and SDBS tracer tests were conducted. DNAPL-water interfacial area was calculated based on the SDBS tracer data as described in Section 3.4.

After the completion of the dissolution and tracer testing, the DNAPL was drained from the network bottom ports and then ethanol was flushed through the influent/effluent manifolds to quantify the recoverable volume of PCE DNAPL. Effluent samples were collected during the



flushing and analyzed for PCE concentrations within the ethanol solvent. Approximately 25 to 75 percent of the volume of DNAPL input was recovered for all experiments. The low fracture network mass recoveries are attributed to collection of drained volume and the ethanol effluent into the open glass filtering flask reservoir which readily volatilized the PCE from the solvent.

### **3.8. Task 3b: Fracture Network Bioaugmentation Experiments**

Prior to inoculation of the dechlorinating microbial culture, the fracture network was flushed for two weeks with an anaerobic groundwater containing nutrient and electron donor constituents. This solution was prepared using nitrogen-sparged artificial groundwater (described in previous quarterly reports). Immediately following sparging, the bottles were placed in an anaerobic gas chamber where sodium-(L)-lactate, yeast extract and diammonium phosphate were amended. Each bottle contained 1 mL of a dilute solution of resazurin dye to verify that anaerobic conditions were maintained. The water was transferred into a gas-tight Tedlar plastic bag and connected to the fractures network. When the water exiting the network showed lactate concentrations similar to the influent and the water exiting was clear, it was determined the system was anaerobic and ready for bioaugmentation.

The *Dehalococcoides sp.* (DHC) containing microbial culture (SDC-9, Shaw Environmental and Infrastructure, Lawrenceville, NJ) was injected into the effluent tubing by way of a three-way valve. Using a 50 mL syringe,  $5 \times 10^8$  cells were injected at a flow rate of roughly 2.5 mL/min. The residence time in the fracture network was approximately 14 hours. After inoculation, the fracture network effluent was monitored for the volatile organic compounds (VOCs), reduced gases (ethene/ethane), chloride generation, pH, lactate, DHC cell concentration, and flow. VOC, reduced gases, and chloride concentrations were used to determine the extent of DNAPL dissolution enhancement that occurred as a result of bioaugmentation.

### **3.9. Task 3c: Fracture Network Chemical Oxidation Experiments**

Three KISCO experiments and four oxidant applications (identified as KISCO-1, -2 and -3) were used to evaluate the effectiveness of KISCO in an experimental fractured network setting. One KISCO application was applied during KISCO-1 and two sequential KISCO applications were applied during KISCO-2, referred to as KISCO-2a and 2b. KISCO-2b was used to determine if reaction by-products from prior KISCO applications affected the efficiency of subsequent KISCO applications due to a reduced DNAPL-water mass transfer as discussed previously. KISCO-1 and KISCO-2a were conducted at the same  $\text{MnO}_4^-$  concentration (7.5 g/L), while KISCO-2b and KISCO-3 were conducted at a concentration of 1.5 g/L  $\text{MnO}_4^-$ . Table 3-6 presents the experimental conditions related to the KISCO experiments.



**Table 3-6.** Experimental variables for each of the fracture network KISCO experiments.

Experiment	KISCO-1	KISCO-2A	KISCO-2B <sup>a</sup>	KISCO-3
Average Aperture (cm) <sup>b</sup>	0.1	0.1	0.05	0.06
Flow Path Fracture Volume (cm <sup>3</sup> ) <sup>c</sup>	95	93	49	60
Velocity <sup>d</sup> (cm/min)	1.5	1.5	1.7	1.2
DNAPL Residual Saturation (%)	25	13	13.9	17.5
PCE DNAPL Mass (g)	92.6	46.3	47	60
Permanganate concentration (g/L)	7.5	7.5	1.5	1.5

<sup>a</sup> KISCO-2b was part of sequential experiment <sup>b</sup> The mass balance aperture was used as the average aperture. <sup>c</sup> Flow path fracture volume is calculated as length of the fracture network multiplied by width and average aperture size. <sup>d</sup> Velocity was determined using CXTFIT.

Prior to KISCO applications, PCE DNAPL saturation ( $S_N$ ) was established to evaluate steady state dissolution of DNAPL in the fracture network. The KISCO experiments presented herein were carried out following the Network B dissolution experiments in the following sequence: Experiment 5 (KISCO-1), Experiment 6 (KISCO-2) and Experiment 8 (KISCO-3).  $S_N$  was defined as the volume of PCE DNAPL trapped in the network divided by the total fracture volume of the experimental network. The  $S_N$  for KISCO applications was adjusted to reflect the reduction in DNAPL volume from dissolution experiments.  $S_N$  was established by injecting PCE DNAPL along the top influent vertical fracture ports at approximately 3.5 cm/min until primarily DNAPL was observed in the effluent and displacement of AGW ceased. Injection from the top influent was selected in order to mimic DNAPL infiltration into a horizontal aquifer transport path. Following DNAPL delivery, the AGW flow rate was increased to a rate at least five times the experimental flow rate for a minimum of ten fracture volumes to displace all mobile PCE. Values of  $S_N$  for each chemical oxidation experiment are presented in Table 3-6. Mass quantities are generally reported in grams or milligrams (mg) instead of moles, to directly compare observed mass removal rates to other reported fracture and/or porous media experiments.

Once  $S_N$  was established PCE DNAPL dissolution rates were monitored for several days prior to KISCO applications to ensure steady state dissolution conditions were established. Experimental velocities, presented in Table 3-6, were similar to typical groundwater velocities observed in naturally fractured rocks (77). The experimental flow rate remained consistent for the duration experiment and was not increased during application of KISCO. The design experimental linear velocity (cm/min) was calculated using CXTFIT. Additionally, the average aperture of the primary flow path was considered equivalent to the mass balance aperture ( $e_{mb}$ ) described in Tsang (82). Finally, the quantity of KISCO applied to the fracture network was designed to be stoichiometrically sufficient to remove the residual mass of PCE DNAPL in the experiment. PCE DNAPL mass removal was calculated based on the stoichiometry in Eq 6-1), using measured effluent chloride concentrations collected from the inline chloride-ion probe (minus the concentration of background chloride in the artificial groundwater). Oxidant consumption and  $MnO_2$  generation was monitored during the KISCO-2 and KISCO-3 experiments.  $MnO_4^-$  consumption data from the KISCO-1 experiment was not collected. During chemical oxidation experiments, effluent chloride readings were collected via data logger every 2 minutes using a inline chloride selective ion probe or, barring availability of the data logger, samples were collected by hand during the last chemical oxidation experiment (KISCO 3). Prior to and following each chemical oxidation application, the chloride probe was calibrated using a five-point semi-log calibration and effluent chloride concentrations were determined using the calibration curve. The background chloride concentration of the artificial groundwater was subtracted from the chloride concentration to determine the volume of chloride generated from the oxidation of PCE. The effluent pH was monitored periodically with pH test strips and cross checked with a pH probe daily.

An experimental “enhancement factor” was calculated to quantify PCE mass removal from KISCO relative to mass removal from pre-KISCO steady state dissolution. The enhancement factor was calculated using the following formula:

$$E_f = \frac{MR_{KISCO}}{(SSD_{pre-KISCO} \times t_{KISCO})} \quad \text{Eq. 3-7}$$

where  $MR_{KISCO}$  is the mass removal of PCE DNAPL during KISCO (mg removed),  $SSD_{pre-KISCO}$  is the average PCE DNAPL mass removal rate during steady state dissolution (mg removed/day) and  $t_{KISCO}$  the number of days KISCO was applied. We expect ISCO to remove more than water flushing only, which would yield an enhancement factor greater than 1. An enhancement factor less than 1 indicates steady state dissolution conditions remove more PCE than was observed during KISCO; an enhancement factor of 1 indicated no difference water-only dissolution and ISCO. The  $SSD_{pre-KISCO}$  mass removal rates were calculated by time-integration of effluent aqueous PCE ( $PCE_{aq}$ ) concentrations prior to KISCO and, for the comparison calculation, it was assumed the mass removal rate during steady state dissolution would have remained constant for the duration of time that KISCO was subsequently applied. Following each KISCO experiment (except between 2a and 2b), the network was drained from the bottom ports and flushed with a 5% acetic acid and hydrogen peroxide solution (to remove  $MnO_2$  precipitation as practicable),

ethanol (to remove remaining PCE DNAPL) and AGW until background concentrations of all amendments applied to the network were negligible.

Tracer tests were conducted using aqueous solutions of sodium bromide and sodium dodecylbenzosulfonate (SDBS,) as described in Section 3.7.1. Briefly, prior to PCE DNAPL injection and  $\text{KMnO}_4$  delivery, sequential conservative tracer tests were conducted to ensure saturated conditions existed (i.e., no retardation of SDBS, because it would partition to an air-water interface) and to quantify fracture volume, hydrodynamic dispersion and characteristic aperture in the fracture network. A 50 mg/L solution of bromide and SDBS tracers was used. Once residual  $S_N$  was established, interfacial area tracer tests were conducted to quantify the network-averaged DNAPL-water interfacial area. Following KISCO, interfacial area tracer tests were again conducted to quantify changes in the DNAPL-water interfacial area, or potentially the effective fracture volume, as a result of KISCO.

### 3.10. Analytical Methods

#### *Single Fracture Experiments*

For the single fracture experiments performed at Shaw Environmental, Inc., Chlorinated ethenes and reduced gases concentrations were determined via headspace analysis using a Varian 3900 gas chromatograph equipped with a Flame Ionizing Detector (FID) and Aluminum RT column. Aqueous concentrations were determined by applying Henry's Law. Hydrogen headspace analysis was performed on a Varian 3800 GC equipped with a Valco Pulsed Discharge Helium Ionized Detector (PDHID) and tandem Pora Bond Q and Molesieve columns. Volatile fatty acid analysis was performed on a Dionex AS 50 Chromatograph equipped with a Dionex IonPac AS11-HC column and CD 25 Conductivity Detector. Anions were analyzed via ion chromatography (Dionex DX-120, Sunnyvale, CA). The effluent pH was monitored periodically with pH test strips. Aqueous DHC concentrations were determined by quantitative real-time PCR with primers (5'- gaagtagtgaaccgaaagg and 5'- tctgtccattgtagcgtc) that amplified a 235bp fragment of the 16s rRNA gene of DHC-type organisms. Biomass was concentrated via centrifugation at 3700 rpm for a minimum of one hour. Our previous work (5) demonstrated that measurement of DHC for the culture used in this study was sufficient to assess overall dechlorination activity and kinetics. Ferrous iron was measured using a Hach test kit model IR-18C. Permanganate was analyzed using a Thermo Scientific Genesys 2 UV-spectrophotometer at a wavelength of approximately 525nm. Persulfate concentrations were determined via titration using a 0.01N standardized sodium thiosulfate solution (Alfa Aesar).

#### *Fracture Network Experiments*

For the fracture network experiments performed at the Colorado School of Mines, Samples were collected directly into 2-ml gas chromatograph vials with zero headspace, sealed with an airtight Teflon-lined cap and analyzed within 72 hours of collection. Effluent dissolution samples not immediately analyzed were stored at 4 degrees Celsius until analysis. . Aqueous phase PCE samples collected during  $\text{KMnO}_4$  application were collected as 1:1 hexane extractions by



placing 1 milliliter (mL) of  $\text{KMnO}_4$  effluent into 1 mL of hexane, which served to cease the  $\text{KMnO}_4$  reaction and extract the PCE in the aqueous solution. All aqueous PCE samples were analyzed within 72 hours of collection by gas chromatography with flame ionizing detector (FID) (Shimadzu GC-17A with auto-sampler). SDBS was analyzed using a Beckman UV-spectrophotometer, with SDBS absorption at approximately 225 nm. Due to interference of aqueous-phase PCE at 225 nm on the UV-spectrophotometer, aqueous PCE was volatilized from the tracer samples prior to analysis and reconstituted with AGW for any evaporative AGW losses.

During bioaugmentation experiments, chlorinated ethenes were analyzed using a gas chromatograph (GC) with a flame-ionizing detector (Shimadzu GC-17A) using headspace analysis. Samples were collected using a gas-tight syringe to draw sample from system, injected into a sealed head-space vial, and allowed to equilibrate for 24 hours prior to analysis. Bromide, the conservative tracer used for characterization of flow, and chloride, a product of biodegradation of PCE, were analyzed using Cole-Parmer ion specific probes. Samples were collected and sent to Shaw Environmental, Inc. (Lawrenceville, NJ) for qPCR analysis. The presences of sufficient electron donor, lactate, was evaluated qualitatively using a colorimetric test using a lactate reagent (Catachem, INC Bridgeport, CT).

$\text{KMnO}_4$  concentration and consumption was monitored during the ISCO 2, 3 and 4 experiments and were analyzed at 525 nanometers (nm) on a Hach UV/visual light spectrophotometer.  $\text{KMnO}_4$  consumption data from the ISCO 1 experiment was not collected.  $\text{MnO}_2$  generation was determined by comparing filtered and unfiltered samples of the  $\text{KMnO}_4$  effluent at the 525 nm wavelength. The effluent pH was monitored periodically with pH test strips. Bromide and chloride samples were analyzed via Cole Parmer ion-specific conductivity probe. SDBS was analyzed using a Beckman UV-spectrophotometer at 225 nm. Following DNAPL dissolution experiments, samples were collected from the 46 side sample ports in Network B to quantify DNAPL and  $\text{KMnO}_4$  distribution.

#### 4. A CONCEPTUAL AND NUMERICAL MODEL TO DESCRIBE BIOAUGMENTATION FOR TREATMENT OF DNAPL SOURCES IN BEDROCK FRACTURES

This section describes the development of a bioaugmentation model to describe the results of the single fracture bioaugmentation experiments described in Section 6. Specifically, the observed data from single fracture bioaugmentation experiments 1 and 3 were evaluated. Modeling efforts were focused on the bioaugmentation kinetics rather than on extrapolation to 3-dimensional systems, as the biological and mass transfer processes controlling DNAPL dissolution and dechlorination were deemed most critical for assessing DNAPL dissolution processes. The model code described in this section may, however, be incorporated into the 3-dimensional RT3D transport model.

It was observed from the experimental data that there was a substantial stochastic variation in the dissolved PCE concentration levels in the single fracture bioaugmentation experiments 1 and 3 (discussed in Section 6); such variation is not uncommon for DNAPL dissolution in bedrock fractures (10, 83). To realistically recreate this stochastic variation in the model, we have converted the reported daughter product concentrations into equivalent moles of PCE and added them to the reported PCE level. This combined PCE concentration estimate was used as the input PCE level (after accounting for the time lag based on residence time). Appropriate interpolation methods were used to evaluate average daily concentration values for input PCE levels.

The reductive dehalogenation of PCE into TCE, DCE, VC and ethene along with the growth of mobile and immobile DHC was modeled using Monod kinetics (17, 84). The fate and transport of a contaminant in ground water can be modeled by the following one-dimensional equation:

$$\frac{\partial C}{\partial t} = -V \frac{\partial C}{\partial x} + D \frac{\partial^2 C}{\partial x^2} + \beta$$

Eq. 4-1

where  $C$  is the aqueous phase concentration (mg/L),  $V$  is the velocity (m/day),  $D$  is the hydrodynamic dispersion co-efficient ( $m^2/day$ ) and  $\beta$  is the reaction term. The above equation can be solved at every node on a given grid using a finite difference approximation. In case of multiple species, the above equation is written for all the species with the  $\beta$  term being coupled as one species degrades to form the daughter products. In this study, we used the operator split strategy to solve the equation (1) numerically. Operator split strategy is one of the numerical strategies used in solving multi-species reactive transport problems (85). The governing equations for all the reactions in the system are given below.

$$\frac{dC_{PCE}}{dt} = -V \frac{\partial C_{PCE}}{\partial x} + D \frac{\partial^2 C_{PCE}}{\partial x^2} - \left[ \frac{q_{PCE} X C_{PCE}}{C_{PCE} + K_{PCE}} \right] \quad \text{Eq 4-2}$$

$$\frac{dC_{TCE}}{dt} = -V \frac{\partial C_{TCE}}{\partial x} + D \frac{\partial^2 C_{TCE}}{\partial x^2} - \left[ \frac{q_{TCE} X C_{TCE}}{C_{TCE} + K_{TCE} \left( 1 + \frac{C_{PCE}}{I_{PCE}} \right)} \right] + \left[ \frac{q_{PCE} X C_{PCE}}{C_{PCE} + K_{PCE}} \right] - \xi_{TCE} C_{TCE} \quad \text{Eq. 4-3}$$

$$\frac{dC_{DCE}}{dt} = -V \frac{\partial C_{DCE}}{\partial x} + D \frac{\partial^2 C_{DCE}}{\partial x^2} - \left[ \frac{q_{DCE} X C_{DCE}}{C_{DCE} + K_{DCE} \left( 1 + \frac{C_{DCE}}{I_{DCE}} \right)} \right] + \left[ \frac{q_{TCE} X C_{TCE}}{C_{TCE} + K_{TCE} \left( 1 + \frac{C_{PCE}}{I_{PCE}} \right)} \right] - \xi_{DCE} C_{DCE} \quad \text{Eq. 4-4}$$

$$\frac{dC_{VC}}{dt} = -V \frac{\partial C_{VC}}{\partial x} + D \frac{\partial^2 C_{VC}}{\partial x^2} - \left[ \frac{q_{VC} X C_{VC}}{C_{VC} + K_{VC} \left( 1 + \frac{C_{DCE}}{I_{DCE}} + \frac{C_{TCE}}{I_{TCE}} \right)} \right] + \left[ \frac{q_{DCE} X C_{DCE}}{C_{DCE} + K_{DCE} \left( 1 + \frac{C_{DCE}}{I_{DCE}} \right)} \right] - \xi_{VC} C_{VC} \quad \text{Eq. 4-5}$$

$$\frac{dC_{Eth}}{dt} = -V \frac{\partial C_{Eth}}{\partial x} + D \frac{\partial^2 C_{Eth}}{\partial x^2} + \left[ \frac{q_{VC} X C_{VC}}{C_{VC} + K_{VC} \left( 1 + \frac{C_{DCE}}{I_{DCE}} + \frac{C_{TCE}}{I_{TCE}} \right)} \right] - \xi_{Eth} C_{Eth} \quad \text{Eq. 4-6}$$



$$\frac{dC_{Cl^-}}{dt} = -V \frac{\partial C_{Cl^-}}{\partial X} + D \frac{\partial^2 C_{Cl^-}}{\partial X^2} + \left[ \frac{q_{PCE} X C_{PCE}}{C_{PCE} + K_{PCE}} \right] + \left[ \frac{q_{TCE} X C_{TCE}}{C_{TCE} + K_{TCE} \left( 1 + \frac{C_{PCE}}{I_{PCE}} \right)} \right]$$

$$+ \left[ \frac{q_{DCE} X C_{DCE}}{C_{DCE} + K_{DCE} \left( 1 + \frac{C_{DCE}}{I_{DCE}} \right)} \right] + \left[ \frac{q_{VC} X C_{VC}}{C_{VC} + K_{VC} \left( 1 + \frac{C_{DCE}}{I_{DCE}} + \frac{C_{TCE}}{I_{TCE}} \right)} \right]$$

Eq. 4-7

$$\frac{dX_M}{dt} = -V \frac{\partial X_M}{\partial X} + D \frac{\partial^2 X_M}{\partial X^2} + Y X_M - k_{att} X_M + k_{det} X_{IM}$$

$$+ \left[ \frac{q_{PCE} C_{PCE}}{C_{PCE} + K_{PCE}} \right] + \left[ \frac{q_{TCE} C_{TCE}}{C_{TCE} + K_{TCE} \left( 1 + \frac{C_{PCE}}{I_{PCE}} \right)} \right] +$$

$$+ \left[ \frac{q_{DCE} C_{DCE}}{C_{DCE} + K_{DCE} \left( 1 + \frac{C_{DCE}}{I_{DCE}} \right)} \right] + \left[ \frac{q_{VC} C_{VC}}{C_{VC} + K_{VC} \left( 1 + \frac{C_{DCE}}{I_{DCE}} + \frac{C_{TCE}}{I_{TCE}} \right)} \right]$$

Eq. 4-8

$$\frac{dX_{IM}}{dt} = Y X_{IM} + k_{att} X_M - k_{det} X_{IM} + \left[ \frac{q_{PCE} C_{PCE}}{C_{PCE} + K_{PCE}} \right] + \left[ \frac{q_{TCE} C_{TCE}}{C_{TCE} + K_{TCE} \left( 1 + \frac{C_{PCE}}{I_{PCE}} \right)} \right] +$$

$$+ \left[ \frac{q_{DCE} C_{DCE}}{C_{DCE} + K_{DCE} \left( 1 + \frac{C_{DCE}}{I_{DCE}} \right)} \right] + \left[ \frac{q_{VC} C_{VC}}{C_{VC} + K_{VC} \left( 1 + \frac{C_{DCE}}{I_{DCE}} + \frac{C_{TCE}}{I_{TCE}} \right)} \right]$$

Eq. 4-9

where  $C_i$  (mM) is the aqueous concentration of the compound  $i$  (where  $i$  is either PCE, TCE, DCE, VC, ethene or chloride),  $I_i$  (mM) is the competition coefficient,  $q_i$  (mM (cell  $h^{-1}$ )) is the DHC maximum utilization rate coefficient,  $K_i$  (mM) is the half velocity coefficient,  $X_M$  (Cells/L) is the mobile phase DHC concentration,  $X_{IM}$  (Cells/L) is the immobile phase DHC concentration,  $Y$  (cell (mmol  $L^{-1}$ )) is the yield and  $\xi_i$  ( $h^{-1}$ ) is the back-partitioning coefficient,  $K_{att}$  ( $h^{-1}$ ) is the bacteria cell attachment coefficient and  $K_{det}$  ( $h^{-1}$ ) is the bacteria cell detachment coefficient. The reaction package contains 7 mobile species: PCE, TCE, DCE, VC, Ethene, Chloride and mobile DHC. The only immobile species present in the system is the immobile DHC. The immobile species does not have advection or dispersion term and in the model, all the immobile phase concentrations are calculated first during the reaction phase.

Equations 4-2 – through 4-6 describe biodegradation of PCE into its daughter products by the mobile and immobile DHC. Equation 4-2 describes the degradation of PCE into TCE; Eq. 4-3 describes formation of TCE from PCE and its subsequent degradation into DCE. Similarly, Eq. 4-4 through 4-6 describe the formation DCE, VC and ethene, along with the formation of the daughter products VC and ethene, respectively. The Eq. 4-3 through 4-6 also have a model coefficient ( $\xi$ ), which was incorporated in order to account for possible loss of species due to back-partitioning of the daughter products into the DNAPL, as described in Schaefer et al. (83) and Ramsburg et al. (86). This back-partitioning coefficient was not used in equation 4-2 because PCE does not back-partition onto itself. Calculation of the back-partition coefficient is presented in Appendix A-1. Eq. 4-7 describes the process of generation of chloride where one mole of chloride is formed for every mole of daughter product. Eq. 4-8 and 4-9 describe the process of bacterial growth kinetics along with the attachment and detachment processes of mobile and immobile bacteria respectively.

## 5. RESULTS & DISCUSSION: SINGLE FRACTURE DISSOLUTION EXPERIMENTS

### 5.1 Sorption

Results of the SDBS sorption study indicated that there was no measurable adsorption of SDBS on to either the Colorado or Arizona sandstones, as measured SDBS concentrations in the controls were identical to those in the bottles containing the rock fragments. However, SDBS concentrations in the limestone-amended bottles were below the detection limit (less than approximately 5 mg/L), indicating substantial uptake of SDBS. This uptake was likely due to sorption of the SDBS due to the limestone matrix. As a result, the limestone was rejected as a potential model rock for the laboratory fracture dissolution experiments.

Results of the PCE/TCE/DCE sorption testing indicated that there was no significant sorption of PCE, TCE or DCE onto either the Colorado or Arizona rock, as chlorinated ethene concentrations in the bottles containing the rock fragments were greater than or equal to the concentrations in the controls.

Results of the bromide sorption testing are summarized in Table A-2 of the Appendix. Results indicated that there was no significant sorption of bromide onto either the Colorado or Arizona rock, as chlorinated ethene concentrations in the bottles containing the rock fragments were greater than or equal to the concentrations in the controls.

### 5.2 Matrix Porosity

Water uptake versus time curves for each rock are shown in Figures 5-1 and 5-2. The porosity for each rock was calculated by dividing the volume of water uptake by the rock volume. Experiments were performed in duplicate. The average calculated porosity for the Colorado sandstone was 13.8%; the calculated porosity for the Arizona sandstone was 14.8%. These values are within the range typically observed for sandstones.

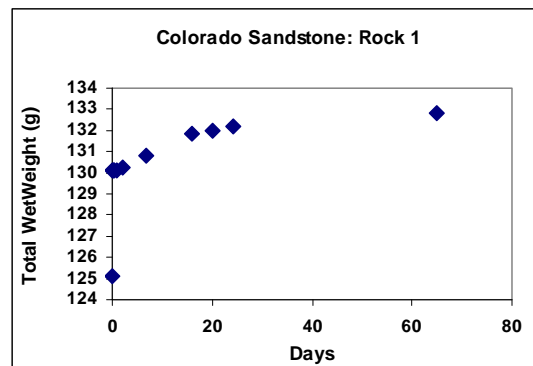


**Figure 5-1.** Water uptake for Colorado sandstone.

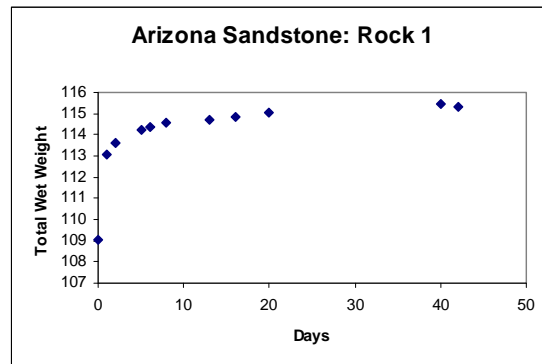


**Figure 5-2.** Water uptake for Arizona sandstone.

### 5.3 Fracture Properties

Typical bromide tracer elution curves for each rock type are shown in Figures 5-3 and 5-4. Elution of the bromide was regressed to the one-dimensional advection-dispersion equation:

$$R \frac{\partial C}{\partial t} = D \frac{\partial^2 C}{\partial x^2} - v \frac{\partial C}{\partial x} \quad \text{Eq. 5-1}$$

where  $R$  is the retardation factor (equal to one for SDBS if PCE DNAPL is absent; and equal to one for bromide with or without PCE DNAPL present),  $C$  is the aqueous solute concentration ( $\text{mg}/\text{cm}^3$ ),  $t$  is the time (sec) minus the approximate residence time in the manifolds,  $v$  is the linear water velocity ( $\text{cm}/\text{sec}$ ),  $D$  is the aqueous dispersion coefficient ( $\text{cm}^2/\text{sec}$ ), and  $x$  is the distance along the line of flow (cm). Bromide elution data were regressed to the solution of Equation 1 using the public domain software CXTFIT (87). Regression results show that the bromide elution is well-described by this model ( $R^2 > 0.97$ ), verifying that any bromide mass transfer between the matrix and fracture does not have a substantial impact on bromide elution (i.e., matrix diffusion effects are negligible for the time scale of the experiments). SDBS, in experiments without residual PCE, co-eluted with the bromide, with no measurable retardation. Thus, consistent with the batch testing, SDBS interactions with the rock surface were negligible. Co-elution of the SDBS with the bromide also indicates that contact with trapped air along the flowpath was negligible, as SDBS also will sorb at the air-water interface (75).

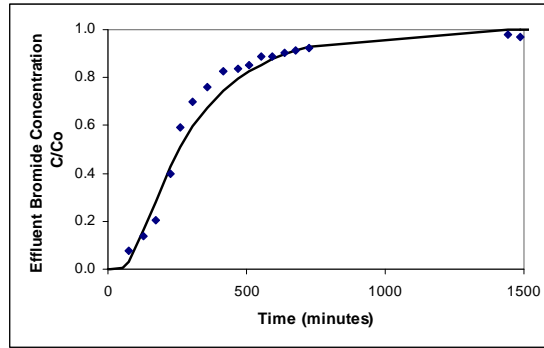


**Figure 5-3.** Bromide elution curves in rock C1 (no residual PCE). The regressed values for the velocity and dispersion coefficient were 0.097 cm/min and 0.61 cm<sup>2</sup>/min, respectively.

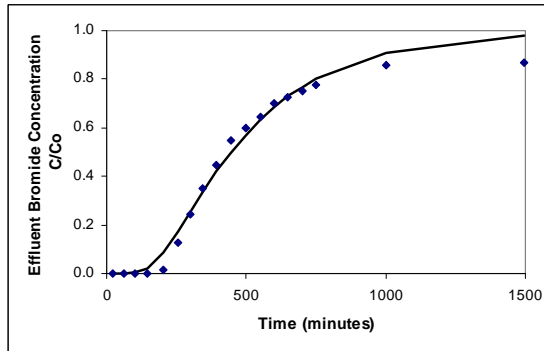


**Figure 5-4.** Bromide elution curves in rock A1 (no residual PCE). The regressed values for the velocity and dispersion coefficient were 0.055 cm/min and 0.31 cm<sup>2</sup>/min, respectively.

Results of the bromide tracer and hydraulic head experiments, in the absence of residual PCE within the fracture, also were used to estimate fracture aperture. A friction loss aperture was calculated as follows (10, 82):

$$\delta_f = L \sqrt{\frac{12\mu}{\rho g |\Delta H| t_m}} \quad \text{Eq. 5-2)}$$

where  $\delta_f$  is the friction-loss aperture (cm),  $L$  is the measured fracture length in the direction of flow (29 cm length of block),  $\mu$  is the water dynamic viscosity (g/cm/s),  $\rho$  is the fluid density (g/cm<sup>3</sup>),  $g$  is the gravitational constant (981 cm/s<sup>2</sup>),  $\Delta H$  is the pressure drop across the fracture (cm H<sub>2</sub>O), and  $t_m$  is the mean residence time (s). Mean residence time was estimated by dividing the fracture length by the regressed velocity. A mass-balance aperture, calculated based on the volumetric flowrate and mean residence time of the bromide tracers, provides an improved estimate of the mean aperture and is calculated as follows (10, 82):

$$\delta_{mb} = \frac{Qt_m}{LW}$$

Eq. 5-3

where  $\delta_{mb}$  is the mass balance aperture (cm),  $Q$  is the measured volumetric flow rate ( $\text{cm}^3/\text{s}$ ), and  $W$  is the measured fracture width perpendicular to flow (29 cm block width). The mass-balance aperture is used to calculate the fracture volume, which is simply  $\delta_{mb}$  multiplied by  $LW$ .

The friction-loss aperture is controlled by small aperture regions, while the mass-balance aperture is controlled by large aperture regions (10, 82). The aperture ratio ( $\delta$ ), defined as the ratio of the friction-loss to mass-balance aperture, serves as a means to characterize a fracture plane in terms of an effective aperture distribution exposed to flow. Values of  $\delta$  approaching unity indicate uniformity of fracture aperture across the fracture plane.

Calculated fracture properties based on initial flow (no DNAPL) and tracer experiments are shown in Table 5-1. Values in Table 5-1 are average values calculated from flow and tracer experiments performed at least in duplicate; all replicate experiments for each rock were within 10% of the average values presented in Table 5-1. Fracture aperture values listed in Table 5-1 are in reasonable agreement with those measured in other laboratory and field studies (10, 88-90), thereby confirming that the fracture apertures used in this study are reasonable. Mass-balance apertures and fracture volumes for all four rocks are similar, although the fracture aperture and fracture volume for A2 were approximately 2-times larger than for the other rocks. This difference likely is due to the natural fracture “roughness” that was induced during the rock splitting process.

**Table 5-1.** Fracture properties for each rock. FV is the mass balance fracture volume, which is calculated by multiplying  $\delta_{mb}$  by the measured length (29 cm) and width (29 cm) of the fracture block. The standard error for the fracture volume was  $\leq 6\%$ .

Rock	$\delta_f$ (cm)	$\delta_{mb}$ (cm)	$\delta$ (-)	FV ( $\text{cm}^3$ )
C1	0.0074	0.038	0.19	31
C2	0.011	0.039	0.28	32
A1	0.0031	0.054	0.057	45
A2	0.0023	0.098	0.023	82

The friction-loss apertures for the two Colorado rocks are approximately three times greater than the Arizona rocks, suggesting that flow through the Colorado rock fractures is less constricted or less controlled by flow through small apertures compared to the Arizona rock fractures. The aperture ratios for the Colorado rocks are also greater than the Arizona rocks, indicating that water flowing through the Colorado rocks experiences narrower aperture distributions than water flowing through the Arizona rocks. This result is somewhat surprising, given the visibly rougher surface of the Colorado rocks compared to the Arizona rocks. As



discussed in the following sections, this may be due to channeled flow within the Colorado rocks that limit water movement to a relatively small fraction of the overall fracture volume.

#### 5.4 DNAPL Architecture

Table 5-2 shows the measured PCE residual saturation (defined as DNAPL volume divided by the  $\delta_{MB}$ -derived fracture volume) and PCE-water interfacial area for each rock. Results of replicate PCE-trapping experiments indicate that measured residual saturation values were reasonably repeatable. Residual saturation values range from an average of 0.18 (C2) to 0.52 (A2). Residual saturation values are within the range reported by others in bench scale fracture experiments (10, 90). Total fracture volumes (the mass balance fracture volume plus residual PCE volume) measured in each rock after attaining residual PCE saturations were approximately equal to the mass balance fracture volumes listed in Table 5-1 (which did not contain residual PCE). This result indicates that the residual DNAPL primarily resided within the flowpath of the fractures, as opposed to pooling or conglomerating in a region that was outside of the zone of flowing water.

**Table 5-2.** Residual saturation and DNAPL-water interfacial area values measured for each rock. Values obtained for replicate experiments are shown. Except where noted, the flow rate was approximately 0.1 cm<sup>3</sup>/min. The calculated standard error of the residual saturation for each computed value in Table 2 is < 12%. The resulting calculated standard error of the interfacial area is less than 28% for each computed value in Table 5-2.

Rock	Residual Saturation (cm <sup>3</sup> /cm <sup>3</sup> )	DNAPL-Water Interfacial Area (cm <sup>2</sup> /cm <sup>3</sup> )
C1	0.22 / 0.26	25 / 19 <sup>a</sup> / 20
C2	0.22 / 0.18 / 0.22	55 / 43 <sup>a</sup> / 45 / 51
A1	0.41 / 0.38 / 0.38	56 / 57
A2	0.52 / 0.38 / 0.38 / 0.45	20 / 20 / 9.1 <sup>c</sup> / 21 <sup>b</sup>

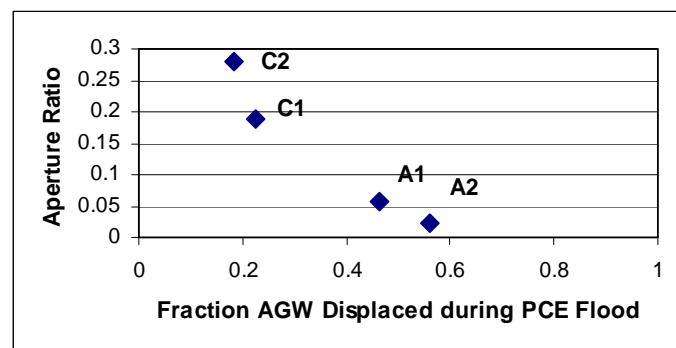
<sup>a</sup> Flow rate was approximately 0.06 cm<sup>3</sup>/min.

<sup>b</sup> Flow rate was approximately 0.5 cm<sup>3</sup>/min.

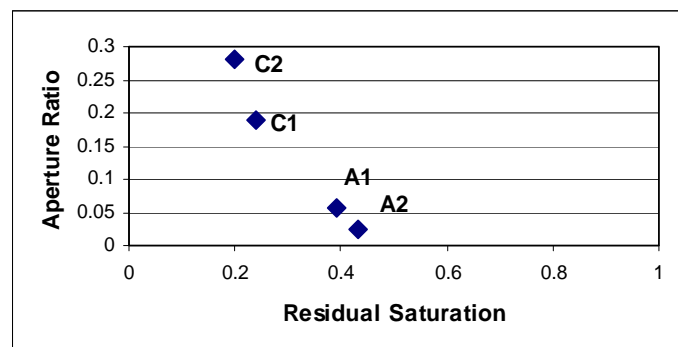
<sup>c</sup> This value was considered an outlier and not used to compute the average interfacial area value used in subsequent calculations.

The large residual saturation values in rocks A1 and A2, relative to rocks C1 and C2, are likely due to connectivity of large apertures within the fractures. Several simulations and experimental observations (90, 91) have shown that percolation of a non-wetting phase through fractures will occur primarily through large aperture regions. The connectivity of these large

aperture regions, and the extent to which large aperture regions are interconnected via small aperture regions, will control the extent to which water is displaced during the PCE flooding and the overall saturation of PCE within the fracture prior to water flooding. The relatively large aperture ratios for C1 and C2 suggest that flow through large aperture regions can occur with limited (compared to A1 and A2) entry into small aperture regions. Because the entry of PCE into small apertures is limited by capillary forces, water displacement and overall PCE saturation (prior to beginning the final water flood) in rocks C1 and C2 are less compared to rocks A1 and A2. This suggests that PCE migrated through discrete pathways within the fractures of the Colorado rocks (more so than in rocks A1 and A2), leaving the majority of the fracture water in place. This is consistent with PCE migration in rocks C1 and C2 occurring through discrete preferential flow pathways that occupied a relatively small fraction of the fracture volume. PCE flowing through A1 and A2 encountered a wider range of aperture regions than in C1 and C2. Consistent with this explanation, the data in Figures 5-5a and 5-5b show that both the water displacement and residual PCE saturation in the rocks are related to the aperture ratio, and injection of PCE into the Colorado rocks was less dispersed (i.e., displaced less water) than the Arizona rocks.



(a)



(b)

**Figures 5-5a and 5-5b.** Aperture ratio plotted as a function of (a) the fraction of artificial groundwater (AGW) displaced during PCE flooding, and (b) PCE residual saturation for each rock.

Table 5-2 also lists the PCE-water interfacial area for each rock. PCE-water interfacial area was calculated by regressing (using CXTFIT)  $R$  in Equation 5-1 to the SDBS elution data (values of  $D$  and  $V$  determined from the corresponding bromide tracer data), and applying the Gibbs Adsorption Equation as follows (6, 79):

$$R = 1 + \frac{a_i K}{\theta} \quad \text{Eq. 5-4}$$

$$K = \frac{\Gamma}{C} = \frac{M_w}{R_g T} \frac{\partial \sigma}{\partial C} \quad \text{Eq. 5-5}$$

where  $K$  is the sorption coefficient for SDBS at the PCE-water interface ( $\text{cm}^3/\text{cm}^2$ ),  $a_i$  is the DNAPL-water interfacial area per fracture volume ( $\text{cm}^2/\text{cm}^3$  fracture volume),  $\theta$  is the volumetric water content within the fracture ( $\text{cm}^3/\text{cm}^3$ ),  $\Gamma$  is the SDBS mass sorbed at the PCE-water interface per unit interfacial area ( $\text{mg}/\text{cm}^2$ ),  $M_w$  is the SDBS molecular weight ( $\text{mg}/\text{mmol}$ ),  $R_g$  is the gas constant ( $\text{dyne-cm}/\text{mmol K}$ ),  $T$  is temperature ( $\text{K}$ ), and  $\sigma$  is the PCE-water interfacial tension ( $\text{dyne}/\text{cm}$ ). Equation 5-5 is evaluated at the influent SDBS concentration (50  $\text{mg}/\text{L}$ ). Regressed values of  $R$  are provided in Table 5-3.

**Table 5-3.** Regressed values of  $R$  from CXTFIT. The standard error for each regressed value of  $R$  from Eq. 1. The standard error for  $R$  calculated for the replicate experiments ( $\delta_R$ ) also is shown in the table.

Rock	Retardation Factor ( $R$ )
C1	1.20 / 1.15 / 1.16 ( $\delta_R = 0.015$ )
C2	1.42 / 1.33 / 1.34 / 1.39 ( $\delta_R = 0.021$ )
A1	1.45 / 1.47 ( $\delta_R = 0.010$ )
A2	1.22 / 1.22 / 1.10 <sup>a</sup> / 1.23 ( $\delta_R = 0.003$ )

<sup>a</sup> Outlier

The slope of the interfacial tension versus SDBS concentration curve was determined by measuring the PCE-water interfacial tension as a function of SDBS concentrations using the Pendant Drop Method (6, 92), then regressing a polynomial expression to the data. Interfacial tension results are shown in Figure 5-6. No PCE was observed in the effluent during the tracer experiments, thus addition of the surfactant and the relatively small reduction in interfacial tension did not result in any measurable DNAPL mobilization.

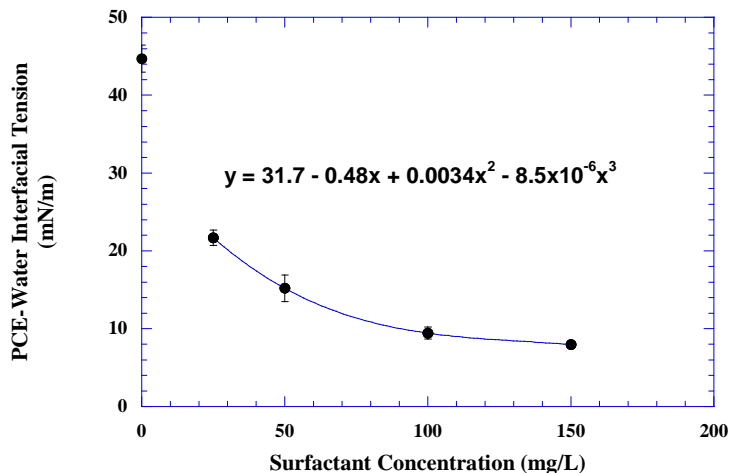


**Figure 5-6** PCE-water interfacial tension as a function of SDBS concentration in water. The polynomial regressed to the data was used to compute the derivative in Equation 5-5.

Measured PCE-water interfacial areas vary by approximately a factor of two among the four rocks, with no apparent correlation to the PCE residual saturation (Table 5-2). This observation suggests that the morphology of the residual PCE in effective contact with mobile water differs among the four rocks. It has been speculated that the aperture ratio is related to the DNAPL-water interfacial area and morphology (10). However there is no observable correlation between fracture aperture and interfacial area for the rocks examined.

Karpyn et al. (90), using micro-computed tomography in Berea sandstone cores with a mean aperture of 0.058 cm, measured an oil-water interfacial area of 52 cm<sup>2</sup>/cm<sup>3</sup> at a residual saturation of 0.58; these measurements are reasonably consistent with values listed in Table 5-2. The interfacial area values in Table 5-2 also are comparable to DNAPL-water interfacial areas in sands with grain diameters similar to the rock apertures. Using a similar surfactant tracer method, Cho et al. (9) measured a DNAPL-water interfacial area of 44 cm<sup>2</sup>/cm<sup>3</sup> in sands with a 0.5-cm diameter. However, the residual DNAPL saturation in the sands was only 0.12, which is two to four times less than the residual saturations measured in the bedrock fractures. Saripalli et al. (79) measured a NAPL-water interfacial area of approximately 90 cm<sup>2</sup>/cm<sup>3</sup> in 0.25-cm diameter sand with a residual saturation of 0.22. Comparisons among these data suggest that the PCE-water interfacial area as a function of PCE residual saturation is greater in sands than in the Colorado and Arizona sandstones. This observation suggests that, for the rocks and sands studied, PCE dissolution rates in rock fractures may be substantially less than in unconsolidated media, as the effective interfacial area per volume of DNAPL in rock fractures is less than in sands.

As noted in Table 5-2, measured PCE-water interfacial areas did not appear to be sensitive to the flowrate of the SDBS tracer solution. If substantial PCE-water interfaces resided in aperture regions that were not contacted with mobile water (e.g., small aperture regions), then decreases in flowrate would likely result in an increase in the measured PCE-water interfacial area, as SDBS would have additional time to migrate to the PCE-water interfaces. Absence of this trend, for the flowrates examined, suggests equilibrium partitioning between the surfactant and the PCE-water interfaces in the fractures, and that the PCE-water interfaces were well-contacted by mobile water regimes (93). Alternately, as discussed in the following section, multiple discrete flow paths within the fracture plane could exist. In this case, assuming that no measurable mixing occurred between the discrete flow paths, the above explanation would be applicable only to the discrete flow path(s) that contained PCE.

## 5.5 DNAPL Dissolution

Results of the DNAPL dissolution experiments for each rock are shown in Figure 5-7. PCE mass within the fractures remained relatively constant during the experiments, as less than 5% of the PCE mass was removed via dissolution. For all four rock experiments, effluent dissolved PCE concentrations approached equilibrium with decreasing flow velocity through the rock, which is consistent with dissolution results observed by others in unconsolidated media (9). These results indicate that PCE dissolution into the mobile water is mass-transfer controlled, and that equilibrium conditions are approached as the flow velocity through the fracture decreases. However, equilibrium concentrations are approached more slowly in the Colorado rocks than the Arizona rocks, especially for rock C1.

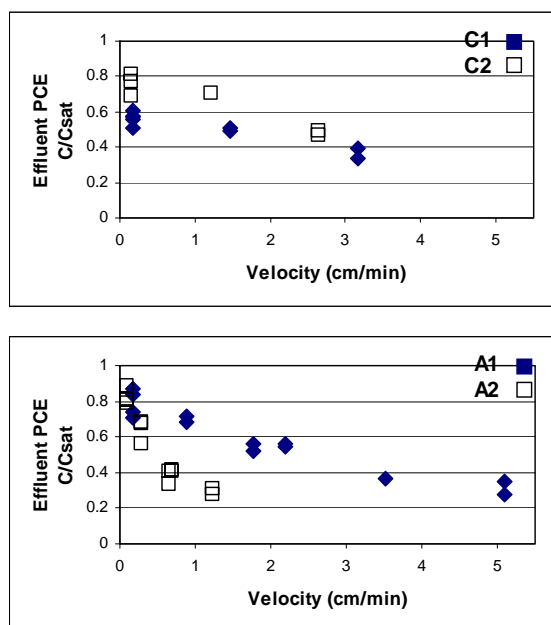


**Figure 5-7.** Effluent dissolved PCE concentration relative to PCE solubility plotted as a function of water velocity for each rock.

To explain this difference in dissolution behavior between the Colorado and Arizona rocks, we consider the DNAPL architecture. PCE in rocks C1 and C2 flowed through preferential pathways of large aperture regions and displaced very little water, as discussed in the previous section. After attaining residual PCE saturation, only a fraction of the water flow through the Colorado rocks likely came into contact with the residual PCE, as a substantial fraction of the water flowing through the rocks were in the “smaller” aperture regions in which PCE never entered. Thus, during dissolution in rocks C1 and C2, the net effluent PCE concentration is reduced due to dilution from flow paths that have not been contacted with PCE. Such flow heterogeneity would likely prevent effluent PCE concentrations in the C1 and C2 rocks from reaching equilibrium until velocities decrease to very small values that would allow diffusion-controlled mixing across flow paths. Thus, fracture planes with preferential flow paths for DNAPL may have reduced dissolved contaminant concentrations relative to fracture planes with a more homogeneous flow field.

To further evaluate the dissolution data, lumped mass transfer coefficients were calculated by assuming: 1) one-dimensional steady-state convection, dispersion, and dissolution in the fractures, 2) a dissolved PCE concentration of zero at the fracture inlet, and 3) a saturated PCE aqueous solution at infinite length (9, 94):

$$K_L = \frac{60\theta}{4D} \left[ \left( v - \frac{2D}{x} \ln \left( 1 - \frac{C}{C_{sat}} \right) \right)^2 - v^2 \right] \quad \text{Eq. 5-6}$$

where  $K_L$  is the lumped mass transfer coefficient (converted to  $\text{min}^{-1}$ ) and  $C_{sat}$  is the DNAPL aqueous solubility ( $\text{mg}/\text{cm}^3$ ). An intrinsic (or, interfacial) mass transfer coefficient,  $K_i$  ( $\text{cm}/\text{min}$ ), is then calculated as follows:

$$K_i = \frac{K_L}{a_i} \quad \text{Eq. 5-7}$$

Calculated values of  $K_L$  and  $K_i$  for each rock were evaluated as a function of the Reynolds number:

$$\text{Re} = \frac{\rho v \delta_f}{\mu} \quad \text{Eq. 5-8}$$

where the friction-loss aperture is used as the characteristic length. This characteristic length was selected because it is assumed that DNAPL-water interfacial mass transfer will occur primarily where small aperture regions intersect large aperture regions (i.e., where DNAPL resides due to capillarity). As previously discussed, measurements of small aperture regions are



better associated with the friction-loss aperture rather than the mass-balance aperture. Mass transfer coefficients as a function of  $Re$  are plotted for each rock in Figure 5-8. In general, values of  $K_L$  and  $K_i$  increase nonlinearly with increasing  $Re$ , and appear to approach an asymptotic value of  $K_L$  and  $K_i$  at higher  $Re$  values. This trend is likely due to higher velocities reducing the thickness of the boundary layer at the DNAPL-water interface, reducing diffusion lengths for mass transfer, and thus increasing the mass-transfer coefficient. Results also indicate that the trends among the four rocks are more similar for  $K_i$  than for  $K_L$ , for flows below an  $Re$  of 0.01. For  $Re$  greater than 0.01,  $K_i$  provided no significant improvement over  $K_L$  for relating mass transfer, likely due to the dissolution becoming increasingly diffusion controlled (i.e., the effective interfacial areas at the elevated flow rates likely were substantially different than those provided in Table 5-2).

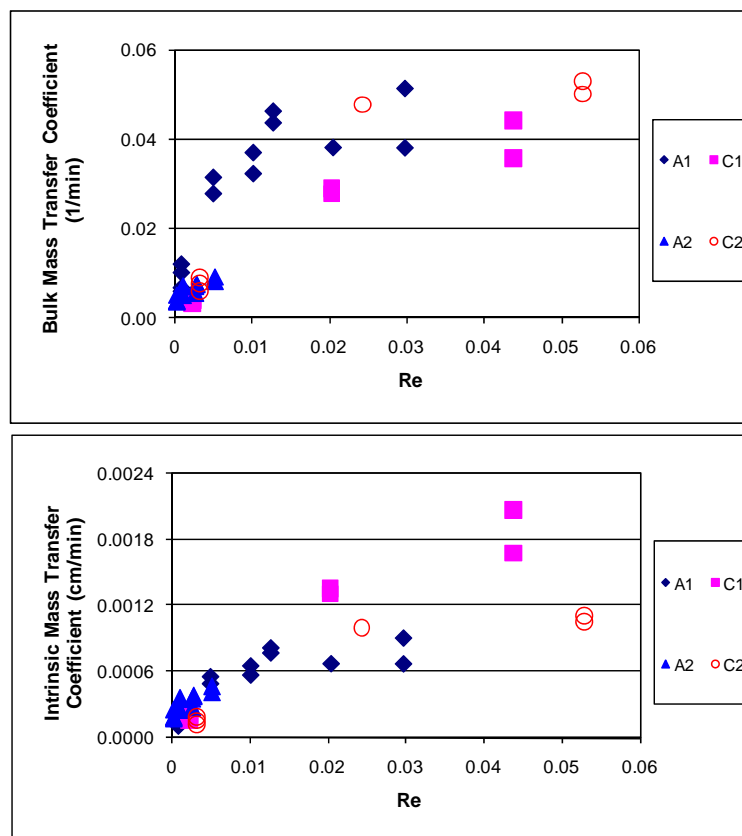


**Figure 5-8.** Lumped and intrinsic mass transfer coefficients plotted as a function of the Reynolds Number for each rock.

By comparison, the lumped mass transfer coefficients measured by Dickson and Thomson (10) in limestone rock fractures at the start of dissolution were approximately 10-times less than those shown in Figure 5-8. DNAPL residual saturations attained by Dickson and Thomson ranged between 0.10 and 0.21, which were significantly less than those measured in the current study, and may explain, in part, the discrepancy in dissolution kinetics between the two studies. The intrinsic mass transfer coefficients measured by Cho et al. (9) in sands were approximately 10-times greater than those shown in Figure 5-8. This comparison suggests that, even when accounting for DNAPL-water interfacial area, DNAPL-dissolution kinetics are substantially slower in the bedrock fracture planes than in sands, possibly due to decreased efficiency of mixing and mass transfer in fractures relative to unconsolidated media. As discussed in the previous section, the PCE-water interfacial area is larger in sands than in discrete bedrock fractures; thus, overall DNAPL dissolution rates in bedrock fractures is likely substantially less than the corresponding rate in unconsolidated sands. Further study using different rock types and fracture networks are needed to attain improved insight into DNAPL dissolution kinetics and morphology in fractured rock systems.

## 5.6 Conclusions – Discrete Fracture Dissolution Experiments

The discrete fracture dissolution experiments have shown that DNAPL dissolution rates in fractures are less than in unconsolidated media of comparable scale, suggesting that DNAPL dissolution in fractures is a relatively slow process compared to DNAPL dissolution in soils. The presence of preferential water and DNAPL flow paths, even within a single fracture plane, was shown to have a significant impact on observed DNAPL dissolution rates, and suggests that heterogeneity and DNAPL distribution at the fracture scale can impede dissolution processes. Examination of the DNAPL architecture relative to the fracture aperture and aperture distribution of the experimental systems was useful in evaluating PCE dissolution behavior. PCE dissolution was reasonably described using a Reynolds number correlation that incorporated DNAPL architecture (the friction loss aperture and the DNAPL-water interfacial area). Development of this Reynolds number correlation and the insights attained into DNAPL dissolution in fractures could serve as useful tools in evaluating DNAPL dissolution in bedrock aquifers.

## 6. RESULTS & DISCUSSION: SINGLE FRACTURE BIOAUGMENTATION EXPERIMENTS

### 6.1 Batch Experiments

Results of the batch testing showed that no dechlorination daughter products (including chloride) were generated over the duration of the experiment in any experiments that contained PCE DNAPL (Figure 6-1). In addition, no fermentation of the lactate was observed, and no sulfate reduction occurred in experiments where DNAPL was present. Thus, the presence of the PCE DNAPL exhibited an apparent inhibitory effect not only on the DHC, but on the fermentative and sulfate reducing bacteria present in the consortium. The addition of hydrogen to the batch reactor systems (900 nM final concentration) did not result in any PCE dechlorination. For the batch experiments containing only dissolved PCE, PCE dechlorination to VC occurred within 20 hours, with continued transformation to ethene over the next several days.

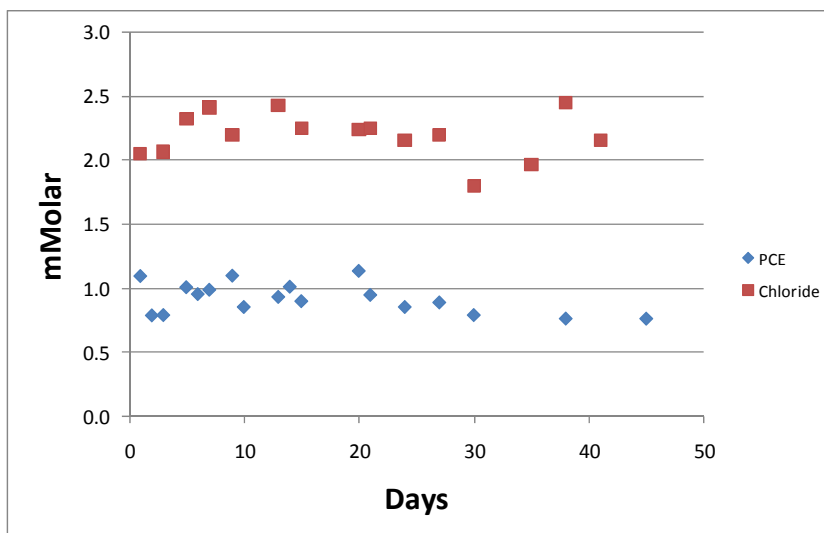


**Figure 6-1.** Batch bioaugmentation experiment with PCE DNAPL. No dechlorination of the PCE was observed over 45 days.

Results for these batch studies indicated that the presence of PCE DNAPL was inhibitory to PCE dechlorination, which is consistent with the results of others (21-23). The lack of PCE dechlorination in the presence of DNAPL could be due to toxicity from the sustained elevated dissolved PCE concentration from the dissolution of the DNAPL, and/or solvation of the DHC into the non aqueous phase.

## 6.2 Dechlorination Kinetics

Initial batch experiments for determination of the Monod kinetic parameters for PCE are shown in Figure 6-2. Results showed that rapid and complete dechlorination of PCE. Using the regression methods described in Schaefer et al. (17), the Monod kinetic parameters were determined for PCE. The regressed half velocity coefficient for PCE is  $0.43 \pm 0.37$  mM, the regressed competition coefficient is  $1.1 \pm 0.012 \times 10^{-2}$ , and the regressed DHC maximum utilization rate coefficient is  $1.7 \pm 0.90 \times 10^{-12}$  mmol Cl<sup>-</sup>(cell h)<sup>-1</sup>. These parameters are used within the bioaugmentation model presented in Section 7.

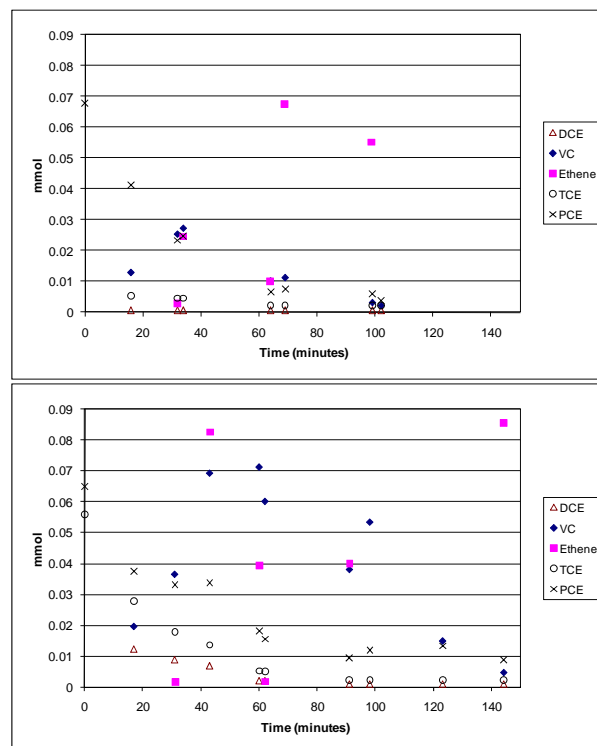


**Figure 6-2.** PCE dechlorination. In the top figure, an initial PCE concentration of approximately 0.07 mM was used. In the bottom figure, initial concentrations of approximately 0.06 mM PCE and TCE were used. Initial DHC concentrations were  $3.8 \times 10^{11}$  cell/L.

## 6.3 General Observations during Bioaugmentation Experiments

Prior to bioaugmentation and during delivery of the lactate and yeast extract amended artificial groundwater, no dechlorination was observed, and DHC levels were below the detection limit ( $<10^5$  DHC/L). Dissolved PCE concentrations measured prior to bioaugmentation (or within a few weeks after bioaugmenting, but prior to observation of measurable dechlorination) generally were in reasonable agreement ( $\pm 20\%$ ) to the abiotic PCE DNAPL dissolution concentrations measured in these same bedrock fractures at the initial flow velocities listed in Table 3-3. The two exceptions were Experiments 1 and 5, where the effluent PCE concentrations varied by up to

40% from those measured during the abiotic experiments (Section 5); this discrepancy may have been due to slight differences in flow paths within the fracture due to introduction of the microbial culture. During all bioaugmentation experiments, effluent pH levels remained at approximately 6.5, and lactate and/or intermediate fermentation products were consistently observed in the fracture effluent indicating that electron donor was present in excess.

## 6.4 Dechlorination Results

### *Arizona Rocks – High Flowrate (Experiments 1 and 2)*

After inoculating with DHC, monitoring showed that dechlorination of PCE occurred in the fractures despite the presence of DNAPL, with generation of measurable quantities of ethene, despite relatively short fracture residence times (270 and 450 minutes for A1 and A2, respectively) (Figure 6-3). DCE initially was the primary dechlorination product in both rocks, but ethene became the predominant dechlorination product at later times. VC and ethene concentrations between days 125 and 195 generally ranged between 0.01 and 0.03 mM. The shift from DCE accumulation to ethene was most apparent in A1, where the DCE to ethene transition correlated with decreases in dissolved PCE concentration to approximately 0.3 mM. These observations suggest that elevated dissolved PCE concentrations limited the further dechlorination of DCE. Similar DCE dechlorination inhibition near PCE DNAPL sources has been observed (22).

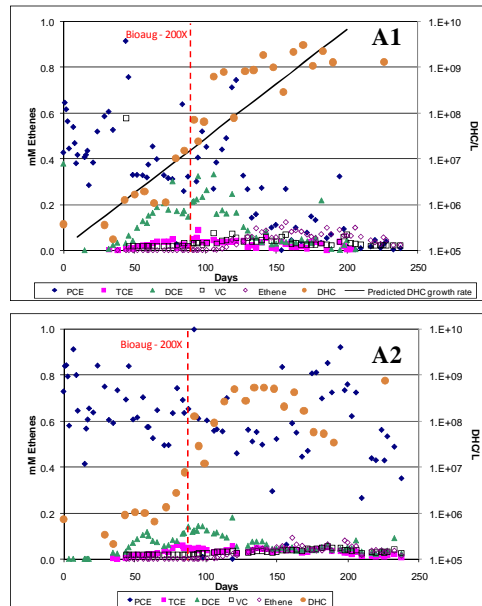


**Figure 6-3.** Effluent concentrations of ethenes and DHC from rock A1 (top) and A2 (bottom) in Experiments 1 and 2, respectively. Fractures were bioaugmented on Day 0. The vertical dashed lines indicate when inoculation with additional culture was performed. The solid line for A1 represents the predicted rate of DHC growth (17). For A2, some interruptions in flow occurred between days 150 and 190. Chloride concentrations were not monitored in Experiments 1 and 2.

DNAPL mass removal was estimated by calculating the mass of dissolved PCE and daughter products exiting the fracture effluent. Approximately 16% of the residual DNAPL was removed in A1 during the experiment (15% as PCE, 1% as reductive dechlorination products). Approximately 8% of the residual DNAPL was removed in A2 during the experiment, with < 1% as dechlorination products (as shown in Table 3-3, A2 contained approximately twice the DNAPL residual volume as A1, which is the primary reason for the large discrepancy in % DNAPL mass removal). While no observable decrease in effluent PCE concentration was observed in A2, effluent PCE concentrations decreased to approximately 0.01 mM in A1, which represents approximately a 98% decrease in effluent PCE concentration with only a 16% decrease in residual PCE DNAPL. This result suggests that most of the residual PCE residing in A1 was in low permeability regions that were not well contacted by migrating water. After day 195, as PCE concentrations continued to decrease in A1, ethene concentrations increased to approximately twice that of PCE, and VC concentrations increased to approximately equal that of PCE. This observation may suggest that the extent of dechlorination within a PCE DNAPL source zone is dependent upon the DNAPL source zone strength function (95). DNAPL sources in bedrock that have dissolved concentrations that decrease rapidly in response to a relatively small fraction of DNAPL source removal may exhibit greater conversion to VC and ethene in response to bioaugmentation treatment than DNAPL sources that maintain elevated dissolved concentrations until nearly all the DNAPL mass is depleted.

An increasing trend in eluted DHC concentrations in both A1 and A2 was observed through 120 days, as effluent DHC levels increased by nearly 4 orders of magnitude. The rate of DHC growth observed in the fracture effluent is well predicted by our previously developed DHC Monod kinetic model (17), as indicated by the solid line for Experiment 1. This model (17) is based on DHC that have been proven capable of complete dechlorination to ethene. These data suggest that the dechlorination and DHC growth in this study are likely due to DHC capable of complete dechlorination. Thus, for the SDC-9 culture and the conditions of this study, the role of any partial dechlorinators likely was limited. It is unclear if adding additional culture had a substantial impact on effluent DHC levels, as effluent DHC levels may have been increasing prior to re-inoculation. DHC concentrations in A1 were slightly greater than in A2, possibly due to the lower dissolved PCE concentration in A1 that may have resulted in decreased inhibition/toxicity on DHC growth and subsequent detachment. Integration of the DHC elution curve and multiplying by the flow rate showed that the amount of DHC eluted from A1 and A2 were 28- and 7-times greater (respectively) than the total amount of DHC inoculated, verifying that DHC growth occurred in the fractures. Some short flow interruptions occurred in A2 between 150 and 190 days, which might explain the decrease in DHC and increase in PCE within this interval.

The influent solution for both A1 and A2 was switched to aerobic artificial groundwater (without lactate) on day 197; 500 ppm hypochlorite was added to the influent solution between days 210 and 212 to remove biomass that may have been sustaining (but at a substantially decreased rate) dechlorination (96, 97). These data suggest that biomass generated in response to bioaugmentation and electron donor addition can serve as a sustained *in situ* electron donor



source after active electron donor addition has ceased. Despite the absence of any substantial dechlorination by the end of the experiment (after 212 days), PCE concentrations remained low in Experiment 1, and did not rebound, indicating that the decreased PCE concentrations were the result of a decrease in DNAPL mass, and were not suppressed due to biological reaction.

#### Arizona Rocks – Low Flowrate (Experiments 3 and 4)

Results of bioaugmentation in the Arizona rocks for Experiments 3 and 4 (Figure 6-4) showed that DCE was the primary dechlorination daughter product, and that DCE concentrations were elevated (~1 mM) compared to DCE concentrations measured in Experiments 1 and 2 (0.1 to 0.3 mM). VC concentrations in Experiments 3 and 4 were 10-times greater than in Experiments 1 and 2. The increased DCE and VC concentrations in Experiments 3 and 4 were likely due to the increased residence time, which allowed for a greater extent of PCE dechlorination within the fractures. Conversely, despite the increased residence time, ethene concentrations in Experiments 3 and 4 were 3-times less than in Experiments 1 and 2. One explanation for this is that VC dechlorination in Experiments 3 and 4 may have been inhibited by the elevated dissolved PCE concentrations, which remained near solubility (approximately 1 mM) throughout the experiment. Alternately, the elevated DCE concentrations in Experiments 3 and 4 may have inhibited VC dechlorination (25).

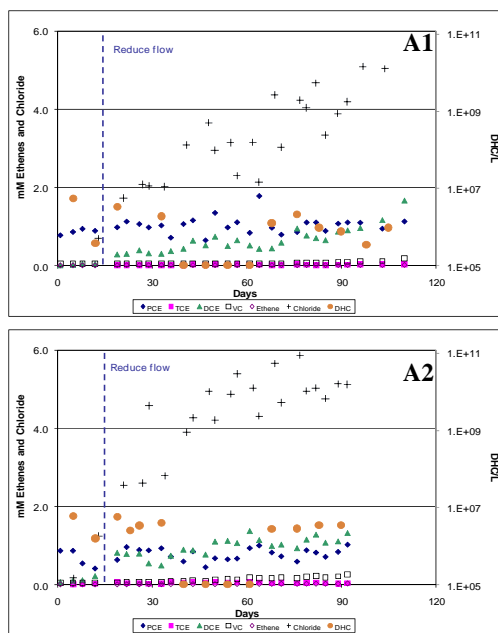


**Figure 6-4.** Effluent concentrations of ethenes, chloride, and DHC from rock A1 (top) and A2 (bottom) in Experiments 3 and 4, respectively. Fractures were bioaugmented on Day 0. The vertical lines indicate when the fractures flow was decreased from approximately 0.10 cm<sup>3</sup>/min to 0.025 cm<sup>3</sup>/min. Experiment 4 was terminated prior to Experiment 3.

Despite the generation of DCE to molar levels near that of the initial PCE effluent concentration, no decreases in effluent PCE concentration were observed during the duration of the experiment. This indicates that biotic dechlorination of the PCE increases the concentration gradient for DNAPL dissolution, thereby enhancing the overall rate of DNAPL dissolution. The quantity of chloride generated was approximately two-times greater than the expected quantity based on the measured chlorinated ethene (and ethene) daughter products. This discrepancy likely is due to back-partitioning of chlorinated ethene daughter products into the DNAPL (28).

The effluent DHC concentrations in Experiments 3 and 4 were 3 orders of magnitude less than in Experiments 1 and 2, despite similar total bioaugmentation dosages. In addition, the total eluted DHC in Experiments 3 and 4 accounted for only 10% of the bioaugmented dosage. These findings suggest that most of the DHC likely became retained within the fractures. However, the increase in DCE concentration was proportional to the increase in residence time in the fracture, suggests that DHC were still controlling dechlorination. However, a contribution from non-DHC partial dechlorinators cannot be completely ruled out. While the absence in DHC concentrations eluting from the fracture suggest that DHC growth was not occurring, the increase in dechlorination rate (as evidenced by the increases in effluent chloride and chlorinated ethene daughters) indicated that DHC levels within the fracture were in fact increasing. As discussed in Section 6.6, increases in immobile DHC (present as biofilms) were likely the cause for the increases in dechlorination rates.

Less than 6% of the initial residual PCE DNAPL was removed from the fractures during the duration of Experiments 3 and 4. PCE mass balance analysis performed on A1 showed that PCE mass removed during bioaugmentation and the post-treatment ethanol flushing accounted for 90% of the initially emplaced DNAPL mass; similar analysis performed for A2 showed 86% PCE mass recovery.

#### *Colorado Rocks – Low Flowrate (Experiments 5 and 6)*

Results for rock C1 (Figure 6-5) were similar to Experiments 3 and 4. Effluent DHC levels decreased from  $10^9$  DHC/L to  $10^6$  DHC/L after reducing the flow rate, consistent with shear-controlled detachment process and consistent with comparison of the low and high flow rate experiments for the Arizona rocks. No increasing trend in effluent DHC was observed throughout the experiment, which is consistent with the low flowrate experiments in A1 and A2. Most of the injected DHC was retained within C1, as the total eluted DHC accounted for approximately 30% of the total bioaugmented cells.

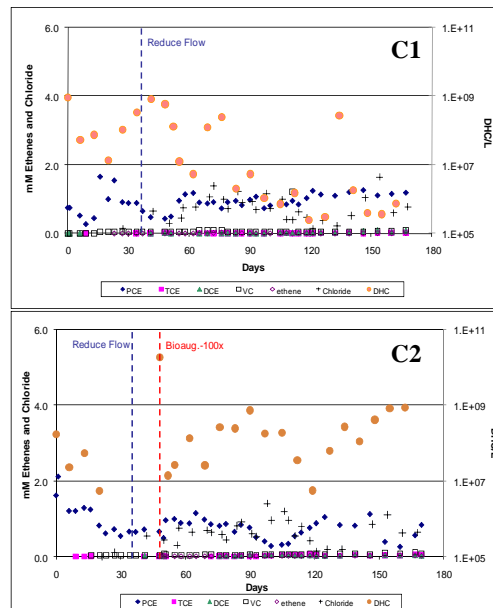


**Figure 6-5.** Effluent concentrations of ethenes, chloride, and DHC from rock C1 (top) and C2 (bottom) in Experiments 5 and 6, respectively. Fractures were bioaugmented on Day 0. The vertical lines indicate when the fractures flow was decreased or when inoculation with additional culture was performed.

Approximately 7% of the residual PCE DNAPL mass was removed (as PCE and reductive dechlorination daughter products) during the C1 experiment (Experiment 5). PCE mass balance analysis performed on C1 showed that PCE mass removed during bioaugmentation and the post-treatment ethanol flushing accounted for 96% of the initially emplaced DNAPL mass.

For C2 (Experiment 6), adding additional culture at a 100-fold greater DHC dosage resulted in elevated DHC concentrations in the effluent. However, less than 1% of the total DHC injected eluted through the fracture. DHC effluent concentrations increased after adding the additional culture, but then remained constant (within an order of magnitude) throughout the remainder of the experiment. Approximately 8% of the residual PCE DNAPL mass was removed (as PCE and reductive dechlorination daughter products). PCE mass balance analysis performed on C2 showed that PCE mass removed during bioaugmentation and the post-treatment ethanol flushing accounted for 59% of the initially emplaced DNAPL mass; this relatively low mass recovery may have been due to losses (leakage, spillage) during the ethanol flushing.

#### *Impact of Increased Flow (Experiment 7)*

qPCR results indicated that no rapid DHC elution or “spike” was observed (greater than 90% of the injected DHC were retained within the fracture), and effluent DHC concentrations were consistent with those obtained in Experiment 5 (Figure 6-6). Initially elevated DHC levels do suggest that some relatively small fraction of DHC were able to rapidly elute through the fracture. Increasing the flow rate resulted in an increase in DHC effluent concentration of

approximately a factor of 5. Combined with the observed decrease in effluent DHC concentrations observed in Experiments 3 and 4 (which were operated at a lower flowrate than in Experiments 1 and 2), these data suggest that DHC detachment and downgradient migration is proportional to the shear.

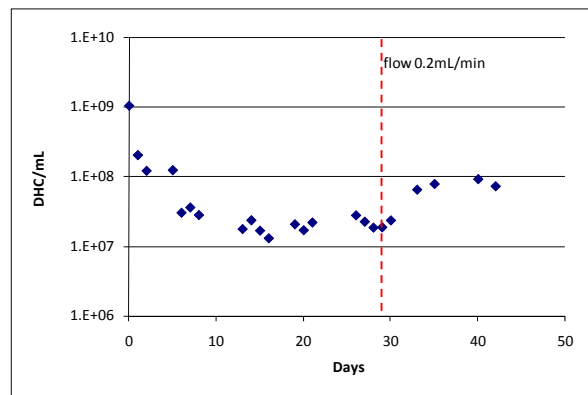


**Figure 6-6.** Effluent DHC levels. DHC levels increase approximately 5-fold after decreasing the flow velocity from 0.044 cm/min to 0.22 cm/min. This suggests that shear forces impact mobile DHC levels within the fractures.

## 6.5 DNAPL Dissolution Enhancement

Similar to the approach employed by others (98), a maximum biotic dissolution enhancement factor (E) to describe the increased rate of DNAPL dissolution during bioaugmentation was calculated as follows:

$$E = \frac{[PCE] + ([TCE] + [DCE] + [VC] + [ethene]) \frac{[Cl^-]_{\text{measured}}}{[Cl^-]_{\text{theoretical}}}}{[PCE]} \quad \text{Eq. 6-1}$$

where the bracketed terms represent measured molar concentration (mM), and the theoretical chloride concentration is the expected chloride concentration based on the measured chlorinated ethene (and ethene) daughter products. The difference between  $[Cl^-]_{\text{measured}}$  and  $[Cl^-]_{\text{theoretical}}$  is assumed to be due to back-partitioning of the organic daughter products into the DNAPL. For [PCE] in Eq. 6-1, the PCE solubility was used for Experiments 3 through 6, since effluent PCE concentrations remained at solubility throughout the duration of the experiment. In Experiments 1 and 2, the PCE concentration measured at 197 days were used, because these concentrations were unchanged after terminating active bioaugmentation.

For the high-flow Experiments 1 and 2, the values of E at the end of bioaugmentation (197 days) were approximately 5 and 1.1, respectively. The reason for the difference in these two

experiments likely is due to the decreased PCE concentrations in Experiment 1 that resulted in less toxicity, which is consistent with observed PCE DNAPL inhibition on dechlorination observed by others (22). It is noted that chloride concentrations were not measured in Experiments 1 and 2, so the actual dissolution enhancement may have been greater than that calculated based on measurement of ethenes alone. For Experiments 3 and 4, the values of E at the end of the experiments were 3.5 and 3.4, respectively. Despite having elevated dissolved PCE concentrations, the dissolution enhancement factor is greater than in Experiment 2 due to the decreased flow rate (longer residence time) in the fracture that provided more time for reductive dechlorination. Daughter product concentrations were gradually increasing at the end of the experiment, so a longer duration experiment would likely have yielded increased values of E.

The calculated values of E for Experiments 1 through 4 generally are within the general range observed by others working with unconsolidated materials (23, 25, 26). However, based on the results of our batch testing and the results others (23), negligible PCE dechlorination would have been expected, due to the presence of DNAPL and dissolved PCE concentrations near 1 mM. The presence of regions within the fracture where the dissolved PCE concentration was reduced (due to flow heterogeneity), thereby facilitating DHC growth and dechlorination activity, is one possible explanation for the observed enhancement factors.

Despite the reduced flow velocities, the dissolution enhancement factors for C1 and C2 (Experiments 5 and 6) were 1.4 and 1.3, respectively. The reason for these relatively low values of E compared to Experiments 3 and 4 (which also were performed at reduced flow velocities) may be due to differences in the effective aperture distribution in each set of rocks. The Colorado rocks have an effective fracture distribution that is substantially more uniform than the Arizona rocks (32). The Arizona rocks contain a comparatively greater number of small aperture regions along the flow path; these small aperture regions likely are devoid of DNAPL, and may serve as optimal locations for DHC biofilm growth and dechlorination activity. Thus, comparison of the Colorado and Arizona bioaugmentation data suggest that aperture distribution (and the distribution of DNAPL within the fractures) may control dechlorination kinetics and overall bioaugmentation effectiveness in these systems.

***When considering the measured dissolution enhancement factors in this bench scale study, it is important to consider the length scale of the experiment. If the length scale of the fracture was 10-times greater, the bioaugmentation residence time correspondingly would be 10-times greater, resulting in approximately a 10-fold increase in dechlorination daughter products. This would result in a calculated value of E that was approximately 10-times greater than those calculated in this study. Thus, results from all six dissolution experiments suggest that bioaugmentation has the potential to substantially increase the rate of DNAPL dissolution at larger scales.***

## 6.6 DHC Migration

As observed by comparing Experiments 1 and 2 to Experiments 3 and 4, effluent DHC concentrations were determined to not be a useful metric for assessing DNAPL dechlorination kinetics. These observations differ from our previous studies that evaluated dissolved phase DCE dechlorination in sand columns (17), where effluent DHC concentrations were correlated to the dechlorination kinetics observed in the column. The presence of the PCE DNAPL, and its inhibitory effects on planktonic DHC at elevated aqueous PCE concentrations, is one possible reason for this discrepancy. DHC present in biofilms, which might be more resistant to toxicity than planktonic cells (99, 100), could have played a dominant role in the observed PCE dechlorination. Additional study is needed to further evaluate the role of DHC in biofilms in bedrock fractures when PCE DNAPL is present.

While increasing the DHC inoculation dosage did not have a measurable impact on dechlorination (as observed by comparing Experiments 5 and 6), the flux of DHC leaving the column was approximately 100-times greater in C2 than in C1. This increased concentration of DHC migrating downgradient of the DNAPL source zone could provide additional remedial benefit for the downgradient plume (25).

## 6.7 Discrete Fracture Bioaugmentation Conclusions

The bioaugmentation experiments for treatment of DNAPL sources in single fracture planes have shown that bioaugmentation using DHC can substantially enhance PCE DNAPL dissolution rates in bedrock fractures. Planktonic DHC in batch systems were unable to dechlorinate PCE when DNAPL was present, but substantial dechlorination was observed in the DNAPL-impacted bedrock fractures. Biofilms and/or the presence of regions with lower dissolved PCE concentrations may have mitigated the inhibitory effects of sustained and elevated PCE levels, resulting in the observed dechlorination. Effluent DHC concentrations did not correlate to observed dechlorination activity, but rather were a function of the flow rate and shear. For the experimental fracture systems and DHC dosages examined, DNAPL dechlorination kinetics were more sensitive to fracture properties than to bioaugmentation dosage, as demonstrated by the differences in the Arizona and Colorado rocks, and the negligible impact on dechlorination rates after increasing the bioaugmentation dosage. However, downgradient migration of DHC, and potential treatment of the dissolved downgradient plume, was impacted by the DHC dosage. Although additional studies are needed to further examine these processes under a wider range of conditions, these results suggest that bioaugmentation may be a viable option for treatment of DNAPL in bedrock, and that bench scale batch testing may not be an appropriate indicator of *in situ* dechlorination kinetics when DNAPL is present.



## 7. RESULTS & DISCUSSION: BIOAUGMENTATION MODEL

### 7.1 Verification Using Batch Data and Simulation

As a preliminary exercise, the kinetic model was first tested to reproduce the batch results reported in Schaefer et al (17). The purpose of this exercise was to validate the numerical code by reproducing a published dataset, and also to test whether a simplified version of the conceptual model presented in the earlier section can sufficiently reproduce a batch experiment. The results from this exercise are summarized in Figure 7-1. The governing reaction kinetic equations used for batch simulations are the same as those presented in Section 4, but with no velocity or dispersion terms (further details of the batch model are presented in Schaefer et al. (17)). The biodegradation parameters used in batch simulations, given in Table 7-1 were obtained from Schaefer et al. (17); our current model produced nearly identical results.

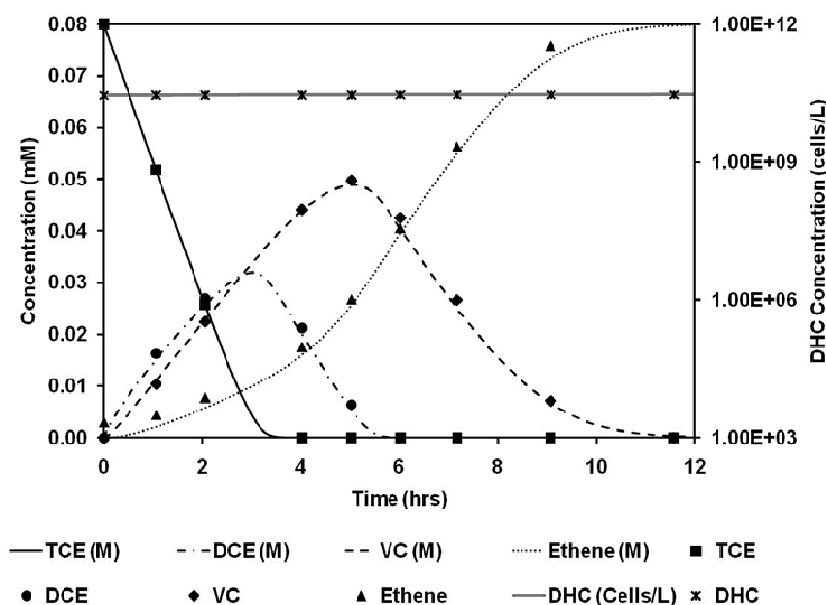


**Figure 7-1.** Model prediction for the batch results reported in Schaefer et al. (17).

**Table 7-1.** Bioaugmentation parameters regressed from batch experiments in Schaefer et al (17), and Section 6. The yield coefficient is  $4.4 \times 10^9$  cell per mM Cl<sup>-</sup>.

Species	K(mM)	q (mmol L <sup>-1</sup> (cell hr) <sup>-1</sup> )	I (mM)
PCE	0.42	1.70E-12	2.50E -01
TCE	0.0032	1.30E-12	1.00E+06
DCE	0.002	7.00E-13	5.20E -03
VC	0.014	1.40E-12	1.00E+06

## 7.2 Model Calibration

The low velocity discrete fracture bioaugmentation experiment, Experiment 3 (Section 6), was used to calibrate the model. The length of the one-dimensional, fracture flow domain was 29 cm, and the domain was discretized using a finite difference grid of 1 cm ( $\Delta x$ ). Other transport parameters used in the simulation are summarized in Table 7-2. It was assumed that the initial inoculation process equally distributed DHC among all the 30 nodes (although the assumption of non-uniform distribution of DHC in the fracture would have little impact on dechlorination rates observed at the effluent). The model was constrained to allow bacterial accumulation at a node to a maximum limiting value of  $1 \times 10^{11}$  cells/L; this is a common approach used for preventing unrealistic accumulation of cells within pore spaces. For example, a parameter  $\theta_{\max}$  has been used to describe the maximum capacity for the adhering bacteria (101). The limiting parameter used in this study employs a similar methodology.

**Table 7-2:** Summary of numerical model parameters used for Experiment 3 (Section 6).

<b>Length (cm)</b>	29
<b>Velocity (cm/hr)</b>	6.45
<b>Simulation time (hr)</b>	5712
<b><math>\Delta x</math> (cm)</b>	1
<b><math>\Delta t</math> (hr)</b>	0.1
<b>Immobile bacteria per node at t=0 (Cells/L)</b>	1.00E+06
<b><math>K_{\text{att}}</math> (1/hr)</b>	0.0018

Two distinct values of DHC maximum utilization rate for DCE degradation,  $q_{\text{DCE}}$ , were used to account for possible inhibitory effects due to presence of high concentrations of PCE (25, 102). When the PCE concentration was less than 0.3mM, the value of  $q_{\text{DCE}}$  was assume to be identical to the batch value. When the concentration of PCE was more than 0.3mM, Yu and Semprini (102) have indicated that the system might show possible inhibitory effects. Therefore,

under high PCE conditions, the value of  $q_{DCE}$  was allowed go below the batch-estimated value. The lower value was estimated as a part of the calibration process.

During the calibration step, we used the Monod parameters from the batch experiments, shown in Table 7-1, as reference values and perturbed them within an order of magnitude and used a trial-and-error process to fit the observed experimental data. In addition to adjusting the Monod parameters, we also fitted the back-partitioning coefficient. It has been shown that a certain fraction of degraded daughter products can back partition to the original DNAPL phases, thus the original DNAPL can serve as a sink for the daughter species (83, 86). We used a back-partitioning coefficient ( $\xi$ ) in our transport model to describe this process. It was observed from the experimental data that DCE was the major daughter product which indicated maximum back partitioning. Hence, the back-partitioning coefficient for DCE was identified as the primary fitting parameter. It is logical to assume that the value of  $\xi$  would depend on the solubility level (which is affinity of the species to remain in the aqueous phase). Based on this assumption, the values of back-partitioning coefficient for the remaining daughter products were simply scaled using their respective values solubility level. The equation used for this scaling process was:

$$\xi_i = \frac{\text{DCE solubility in mM}}{\text{Solubility of daughter product } i} * \xi_{DCE} \quad \text{Eq. 9-1}$$

Appendix A provides various values  $\xi$  and the detailed calculations that employ the above expression.

Figure 7-2 shows compared the final (fitted) model results against the Experiment-A data. The model calibrated values of Monod parameters are summarized in Table 7-3. It can be observed from Figure 7-2 that the results from the model simulations closely follow the trends observed in the experimental results. The model was able to close the mass balance and simulated the chloride ion concentrations very well. Comparison of the values shown in Table 7-3 and Table 7-1 indicate that the fitted model parameters for the transport experiment are within an order of magnitude of the batch parameters. The observed differences in model parameters estimated for the transport and batch model could be due to the heterogeneities present in the fractured system, and/or the elevated PCE and DCE concentrations observed in the fracture experiments compared to the batch experiments that were used to derive the Monod parameters. Several published studies have concluded that batch and column parameters differ due to pore-scale variations and other heterogeneities (103, 104).

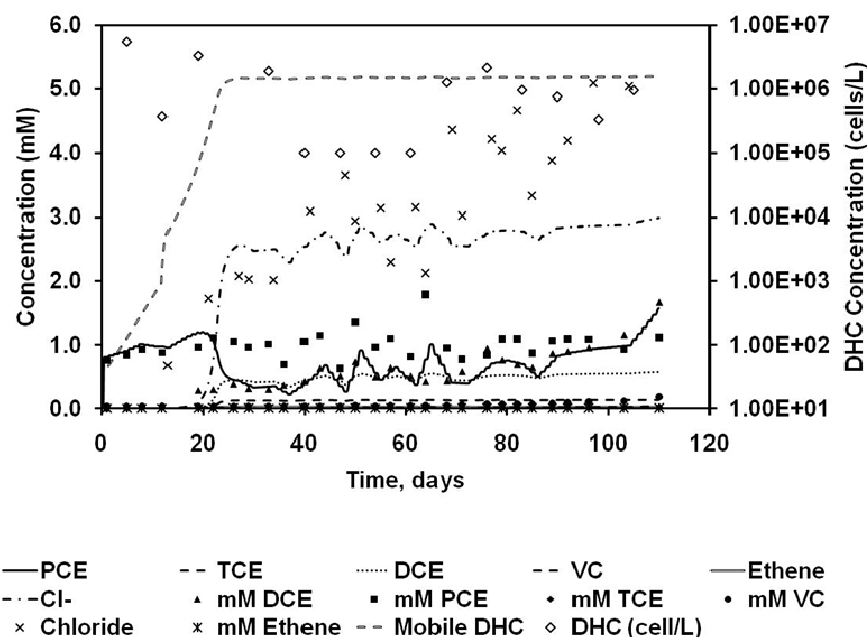


**Figure 7-2.** Model calibration results. Continuous lines represent the model results and the symbols represent Experiment 3 (Section 6) data.

**Table 7-3:** Calibrated Monod parameters for the Experiment 3. The calibrated yield coefficient was  $1.8 \times 10^8$  cell per mM  $\text{Cl}^-$ .

Species	K(mM)	q (mmol L <sup>-1</sup> (cell hr) <sup>-1</sup> )	I (mM)
PCE	0.42	0.87E-12	2.50E -01
TCE	0.0032	1.05E-12	1.00E+06
DCE	0.002	1.85E-13, 7.00E-13	5.20E -03
VC	0.014	1.05E-12	1.00E+06

### 7.3 Model Prediction

The calibrated model developed using the low flow rate data, Experiment 3, was used to simulate the high-flow discrete fracture bioaugmentation experimental system, Experiment 1 in Section 6.. The simulation results along with the experimental data for all daughter products are summarized in Figure 7-3. A comparison of the measured PCE concentration data and the modeled PCE concentrations for Experiment 1 is shown in Figure 7-4. The parent and daughter product data were reported in separate figures for clarity, since the concentrations of PCE were

much higher than any of the daughter products. The results from model-simulations closely follow the experimental data. It should be noted that the all the Monod parameters used in the validation simulation were identical to those estimated in the calibration step. However, the validation step required scaling of two physical transport parameters—the back-partitioning coefficient (for DCE) and the detachment factor to scale for the high velocity conditions. These two parameters likely are a function of the residence time (allowing more time for daughter products to back-partition into the DNAPL) and pore-velocity (which is expected to be proportional to shear forces responsible for bacterial detachment). The modified values of  $\xi_{DCE}$  and  $k_{det}$  are  $0.004 \text{ hr}^{-1}$ , and  $6 \times 10^{-7} \text{ hr}^{-1}$ , respectively. Previously (Section 6), we observed that the detachment process was a function of velocity (which will increase biomass shearing), as increased mobile DHC were measured at the elevated velocity. The high velocity conditions maintained in Experiment 1 caused more bacteria to detach from the immobile phase, when compared to the low velocity condition used for calibration to Experiment 3. This resulted in a relatively high detachment rate for Experiment 1 and also high mobile phase bacterial concentrations which were consistent with the observed experimental data. The reduced regressed value of  $\xi_{DCE}$  in the high velocity (low residence time) experiment is consistent with our conceptual model that the reduced residence time limited the extent to which daughter products were able to back-partition into the DNAPL.

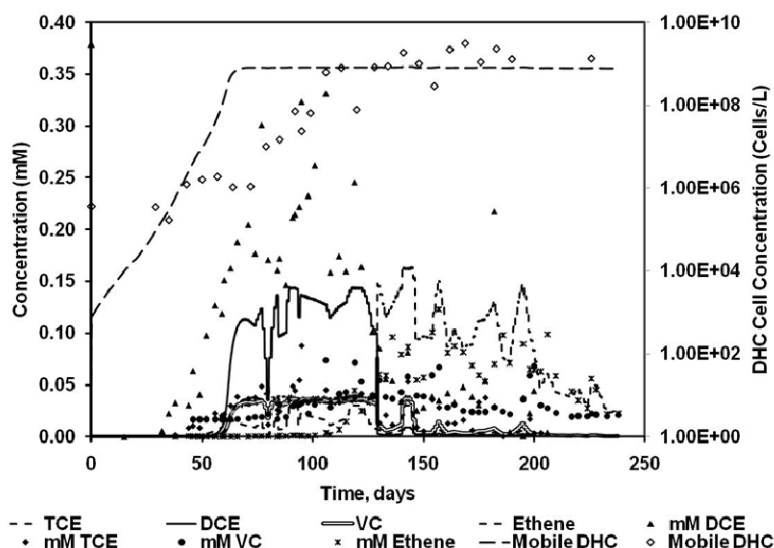


**Figure 7-3.** Model prediction results. Continuous lines represent the model results and the symbols represent Experiment 1 (Section 6) data.

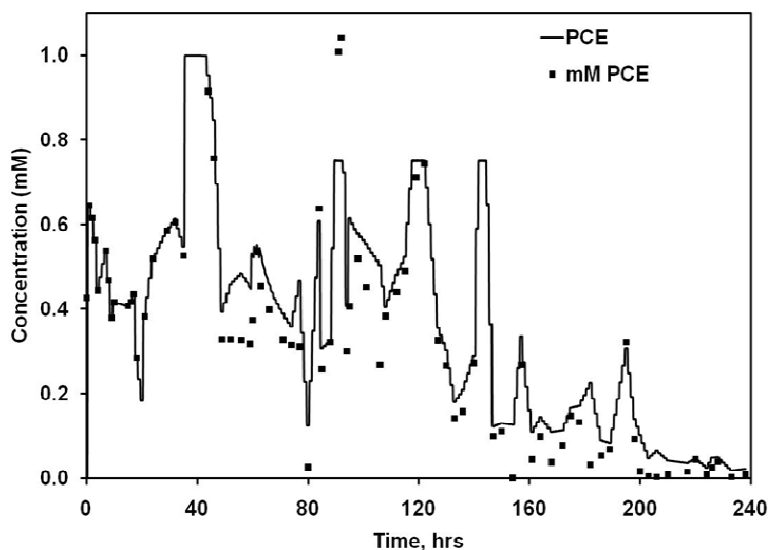


**Figure 7-4.** Comparison of modeled and observed PCE concentration levels (Bioaugmentation Experiment 1)

## 7.4 Sensitivity Analysis

To further understand sensitivity of the model to variations in the parameter values, we performed a sensitivity study. During the calibration step we have identified that the yield coefficient and DHC maximum utilization rate coefficient ( $q$ ) were the most sensitive model parameters. We focused on these model parameters and perturbed them within an order of magnitude and explored its effects on model predicted results for Bioaugmentation Experiment 3. The results are summarized in the following sections.

### 7.4.1 Model response to variations in the yield coefficient

The yield coefficient was varied by the following two factors: 0.5 and 5. Figures 7-5 and 7-6 provide a summary of these simulation results. The yield coefficient governs the rate of growth of the bacteria. It can be observed from these figures that the growth of the bacteria increased with an increase in yield coefficient and thereby causing significant amount of biodegradation. It can also be observed from Figure 7-6 that when the yield coefficient is lowered by 0.5-times, the amount of bacterial growth was considerably lower and the biodegradation is delayed until 50 days instead of the expected 20 days. However, when the yield coefficient is increased by 5-times, the bacterial growth is faster and the biodegradation occurs earlier.



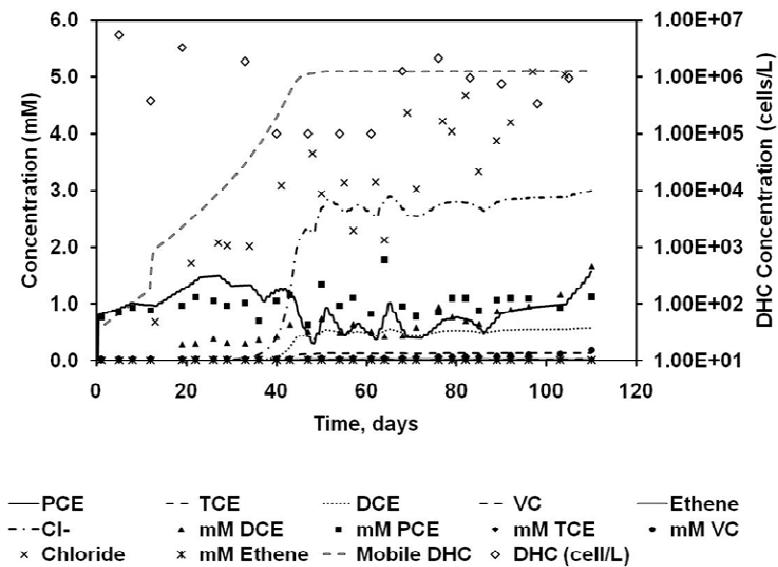


**Figure 7-5.** Model response to an decrease in yield by 0.5 times for Experiment 3.

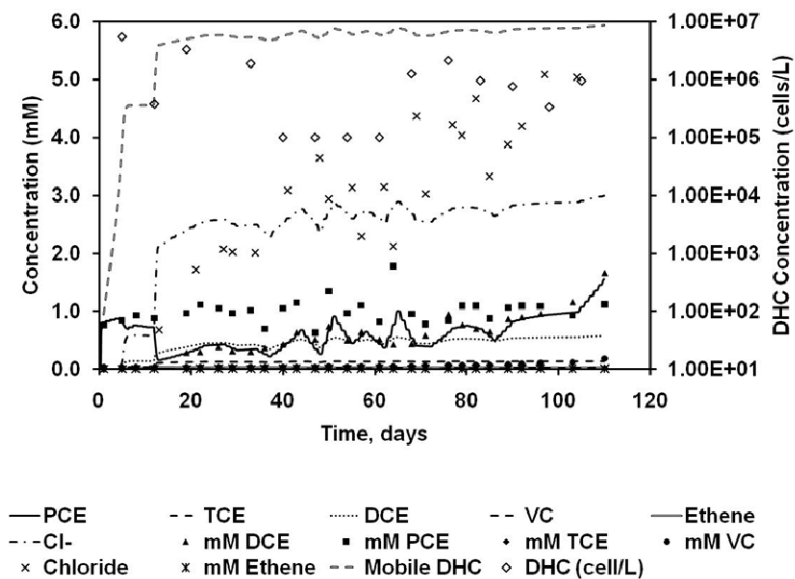


**Figure 7-6.** Model response to an increase in yield by 5 times for Experiment 3.

#### 7.4.2 Model response to variations in the DHC maximum utilization rate constant ( $q$ )

The simulated DHC maximum utilization rate constant ( $q$ ) was varied by the following two factors: 0.5 and 2, as shown in Figures 7-7 and 7-8, respectively. The parameter  $q$  governs the rate at which the chlorinated ethenes are degraded into their daughter products. It can be observed from the figures that when the values of  $q$  were increased, the biodegradation of PCE and its daughter products was higher as shown in Figure 7-8. This increase in dechlorination activity was marked by a significant increase in the chloride ion concentrations. However, a decrease in  $q$  (as shown in Figure 7-7), decreased the observed dechlorination activity. Therefore, the observed aqueous concentrations of PCE and its daughter products are considerably lower when compared to the experimental data.

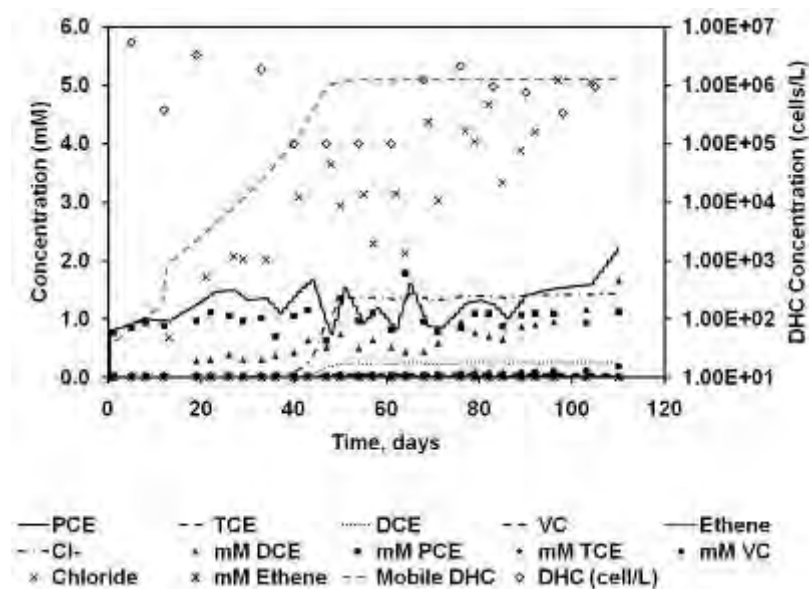


**Figure 7-7.** Model response a decrease in  $q$  by 0.5-times for Experiment 3.

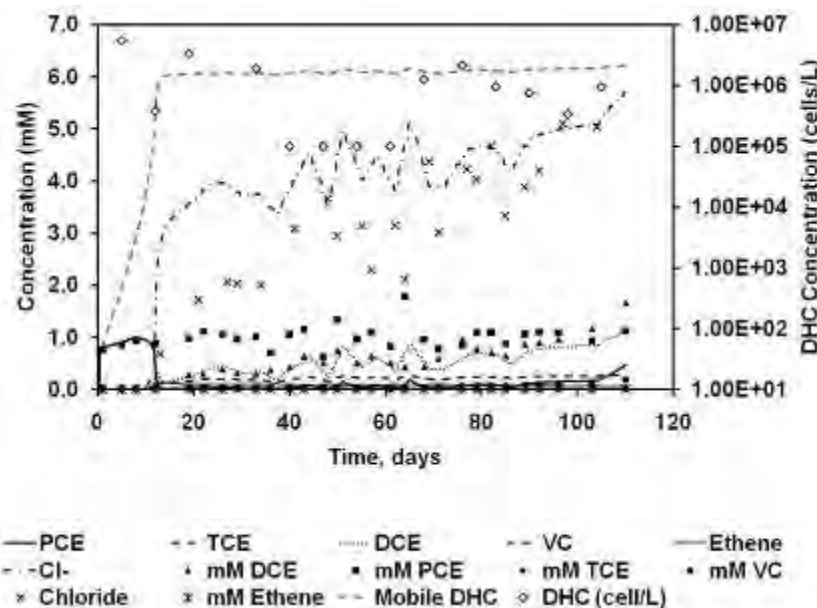


**Figure 7-8.** Model response to an increase in  $q$  by 2 times for Experiment 3.

#### 7.4.3 Bioaugmentation Model Conclusions

The presented mathematical modeling framework can be used to model bioremediation of PCE DNAPL using *Dehalococcoides* in a fracture flow systems. This model was successfully calibrated to our low flow experimental dataset. The performance of the calibrated model was tested by completing a validation simulation where the model was used to predict a transport scenario involving high flow conditions (and comparing it to the high flow dataset). The model was able to predict the high flow rate dataset using the calibrated values of biological process parameter (Monod parameters). The only model adjustments that had to be made for the high flow dataset included the back-partitioning coefficient and the detachment rate, both of which our conceptual model indicates will vary with flow rate. Our sensitivity studies show that the yield coefficient and the DHC maximum utilization rate coefficient are highly sensitive parameters that need to be carefully calibrated. However, the batch estimates of yield coefficient and maximum utilization rate coefficient provide excellent estimates for the calibration process, and final calibrated values were within an order of magnitude of the batch-kinetic values presented in Schaefer et al (17).

## 8. RESULTS & DISCUSSION: SINGLE FRACTURE CHEMICAL OXIDATION EXPERIMENTS

### 8.1 Persulfate Experiments

Results for the persulfate experiments, both alkaline and Fe-EDTA activated, are provided in Figure 8-1. DNAPL treatment rates were based on the mass of chloride generated per unit time, as calculated by measuring the concentration of chloride in the effluent minus the concentration of background chloride in the artificial groundwater. Use of chloride generation to determine PCE or TCE treatment rates has been shown to be appropriate for both permanganate and persulfate (40, 105).

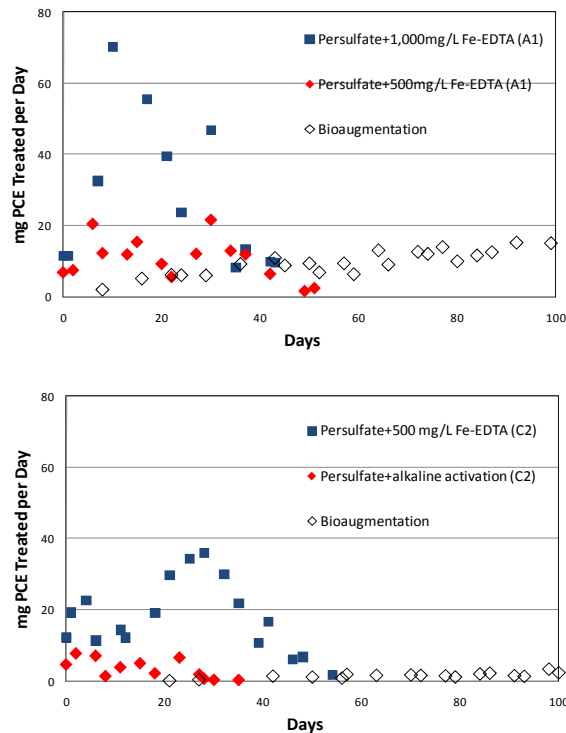


**Figure 8-1.** PCE DNAPL mass removal rates in the persulfate experiments based on chloride generation. Top – A1 rock; bottom – C2 rock. PCE DNAPL mass removal rates measured during bioaugmentation (Section 6) are provided for comparison.

DNAPL mass removal rates for the Fe-EDTA activated treatments were similar in trend for the three experiments, as an initial spike than slow decrease in DNAPL treatment rate was observed. However, the mass of PCE oxidized varied as a function of activation method and rock type. Approximately 1240 mg of PCE were oxidized in A1 using an Fe-EDTA concentration of 1,000 mg/L, corresponding to removal of 4% of the DNAPL mass. In comparison, only 550 mg of PCE were oxidized in A1 using an Fe-EDTA concentration of 500 mg/L, corresponding to removal of 1.8% of the DNAPL mass. In the C2 system, persulfate activation using 500 mg/L of EDTA resulted in 980 mg of PCE removal, corresponding to removal of 20% of the DNAPL mass. The pH values during the maximum rates of DNAPL mass removal were approximately 2, but increased to 4 as the DNAPL mass removal rates decreased.

Results using the alkaline activated persulfate in C2 showed a decreasing trend in DNAPL mass removal similar to that observed for the Fe-EDTA activated persulfate experiments, but the PCE mass removed during treatment was much less, with only 2% of the residual DNAPL removed. Effluent pH remained at or above 12 throughout the duration of the experiment.

Persulfate elution for each of the four persulfate experiments is shown in Appendix A-2. Based on the maximum chloride generation observed in the experiments, and the following stoichiometry:



the maximum decrease in persulfate concentration was expected to be less than 1,500 mg/L. Batch experiments also showed that the persulfate demand of the sandstone rock was negligible, and did not impact elution of the oxidant through the fracture (i.e., no measurable consumption of persulfate due to reaction with rock minerals). However, ferrous iron activation of persulfate (and the generation of sulfate radicals) can result in additional consumption of persulfate, thus the stoichiometry shown in Eq. 8-1 likely underestimates persulfate consumption during ferrous iron activation (105). Consistent with this, our results showed increased persulfate consumption (compared to that predicted by Eq. 8-1) for the Fe-EDTA activated experiments. Our data also show that two weeks lapsed before persulfate was measured in the effluent for the Fe-EDTA activated experiments, indicating that DNAPL treatment rates were likely oxidant-limited for these experiments during this period. For the A1 experiments, persulfate consumption using the 1,000 mg/L Fe-EDTA solution (21,900 mg) was greater than that observed using the 500 mg/L Fe-EDTA (16,100 mg) solution during the elevated period of PCE mass removal (the first 20 days). These results are consistent with the results obtained in batch tests with dissolved phase TCE, using similar ratios of persulfate to ferrous iron, by Liang et al. (105). A molar persulfate:PCE ratio of 15 was observed in the 1,000 mg/L Fe-EDTA experiment for A1, and a molar persulfate:PCE ratio of 25 was observed in the 500 mg/L Fe-EDTA experiment for A1. These molar ratios are within the range previously reported for TCE in batch and column systems using chelated ferrous iron (38, 105), and are substantially greater than the 2:1 molar ratio predicted by Eq. 8-1. These A1 results suggest that chloride generation and DNAPL mass

removal rates may have been greater in the Fe-EDTA activated C2 experiment if an increased Fe-EDTA concentration was used.

Dissolved effluent PCE concentrations prior to oxidant addition for A1 and C2 were approximately 130 mg/L (Figure 8-2); these data are consistent with our previous dissolution studies performed without the addition of chemical oxidants (Section 5). Activated persulfate addition resulted in a decrease in the dissolved PCE effluent concentration during the duration of the oxidant delivery. However, dissolved PCE concentrations increased after oxidant addition ceased as artificial groundwater only was pumped through the fracture. Elution of dissolved phase PCE accounted for approximately 1% removal of the residual DNAPL mass initially emplaced in the A1 experiments, and less than 9% removal of the residual DNAPL mass initially emplaced in the C2 experiments.

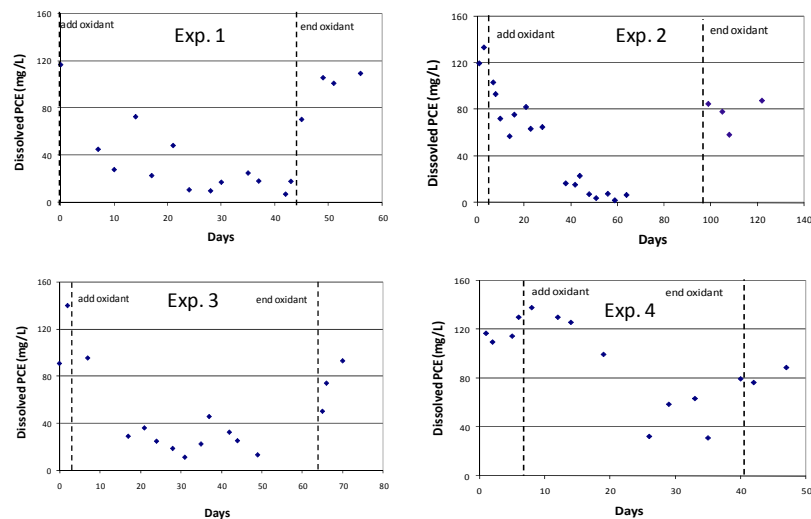


**Figure 8-2.** Dissolved effluent PCE concentrations for each persulfate experiment. The first vertical line indicates when oxidant delivery was initiated, and the second vertical line indicate when oxidant delivery ceased and artificial groundwater only was injected into the fracture.

## 8.2 Permanganate Experiment

DNAPL removal rates for the permanganate experiment are provided in Figure 8-3. Results are similar to those obtained for the Fe-EDTA persulfate experiments in trend, but the peak DNAPL mass removal rate was several times greater than observed in the persulfate experiments. Permanganate was measured in the fracture effluent at approximately half the influent concentration within 24 hours. Approximately 1100 mg of PCE DNAPL was removed, corresponding to a 2% decrease in DNAPL mass. Dissolved PCE concentrations decreased after permanganate addition at a rate similar to that obtained in the persulfate experiments. However,



flow through the fracture ceased by 11 days due to plugging. Substantial generation of MnO<sub>2</sub> precipitates was observed as a dark precipitate in the effluent.

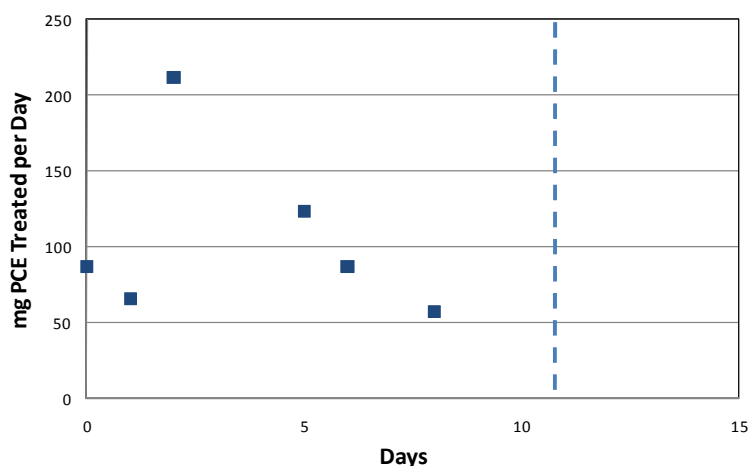


**Figure 8-3.** PCE DNAPL mass removal rates in the permanganate experiment based on chloride generation. The vertical dashed line indicates when the fracture became plugged.

PCE oxidation by permanganate is assumed to occur by the following reaction for pH > than 3 (40, 106-108):



Based on the total mass of permanganate consumed within the fracture (approximately 5,800 mg) and the stoichiometry in Eq. 8-2, 4600 mg of PCE should have been oxidized, which is 4-times the measured mass of DNAPL removal, with a permanganate:PCE molar ratio of 5.3. This increased permanganate consumption was likely due to the oxidant demand of the rock itself, as batch experiments performed at a pH of 3 showed permanganate consumption by the rock; no permanganate consumption by the rock was observed at neutral pH.

### 8.3 Post-Oxidation Tracer Testing and DNAPL Recovery

Bromide and SDBS tracer tests were performed after each persulfate experiment. Tracer testing could not be performed in the permanganate experiment because the fracture became plugged. Results of the SDBS tracer could not be analyzed in the Fe-EDTA activated C2 experiment because of interference (color/particulate) in the effluent. Tracer results for the persulfate experiments showed that no substantial decrease in the effective fracture volume occurred due to persulfate application. However, as exemplified in the tracer results for A1

(1,000 mg/L Fe-EDTA activated) and C2 (alkaline activated persulfate) presented in Figure 8-4, no measurable retardation of the SDBS tracer (relative to bromide) was observed after chemical oxidation; these two compounds co-eluted through the fracture. Similar results were observed in the 500 mg/L Fe-EDTA activated A1 experiment. These results indicate that the effective DNAPL-water interfacial areas listed in Table 5-2 were diminished to the point where, given the conditions of the experiments, the interfacial tracer method could no longer be used to estimate these values.

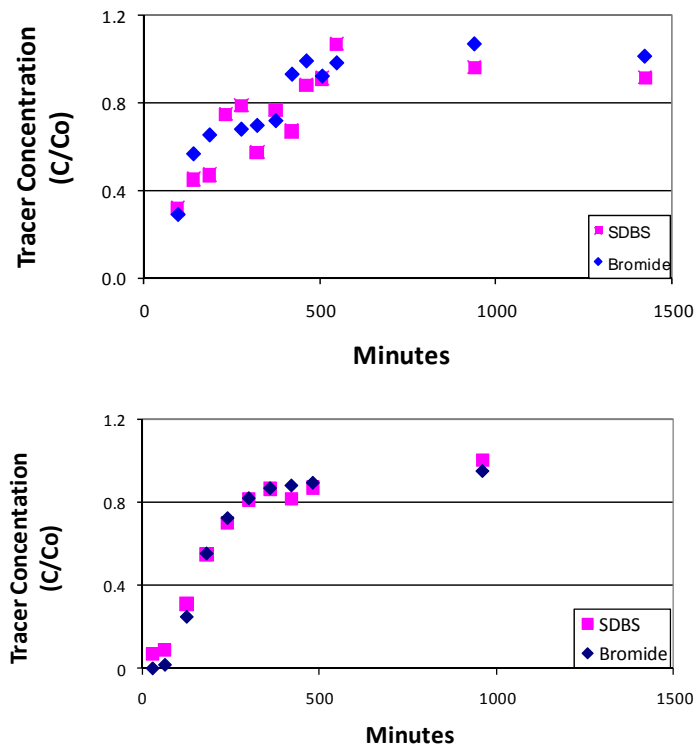


**Figure 8-4.** SDBS and bromide elution curves. The top figure is for Persulfate Oxidation Experiment 1 (A1 rock with persulfate and 1,000 mg/L Fe-EDTA); the bottom figure is for Persulfate Oxidation Experiment 4 (C2 rock with alkaline activated persulfate). Similar results were obtained for Persulfate Oxidation Experiment 2. No measurable sorption or retardation of the interfacial SDBS tracer occurred.

Overall PCE DNAPL mass balances obtained by ethanol flushing at the end of the experiments ranged from approximately 10 to 72%. These recoveries are low compared to those obtained in our previous studies. Previously, we typically obtained greater than 80% DNAPL mass recovery in these fracture systems (Sections 5 and 6); the majority of this recovery occurred within the first few pore volumes of ethanol flushing at flushing flow rates in excess of

1 mL/min; substantial DNAPL free product typically was recovered. In our current study, such rapid DNAPL mass removal typically was not observed, likely due to mass transfer limitations due to precipitate formation. As a result, very low ( $\sim 0.1$  mL/min) ethanol flow rates were employed to flush the fractures. Long term collection of the ethanol flush effluent into open collection vessels likely resulted in substantial volatilization of the PCE, and ultimately the poor mass recoveries.

#### 8.4 PCE Oxidation Rates

Maximum observed rates of PCE oxidation in the persulfate experiments normalized to the water-filled volume of the fractures ranged from 2,600 mg/L/d (1,000 mg/L Fe-EDTA in A1) to 480 mg/L/d (alkaline activated in C2); the maximum observed PCE rate of oxidation was 4,700 mg/L/d in the permanganate experiment (measured on day 2 – prior and subsequent data indicate a rate that is nearly half this value). By comparison, in columns packed with glass beads, and using a similar permanganate concentration and flow velocity to those used for the A2 experiment, a PCE DNAPL oxidation and mass removal rate that was approximately 10-times greater than observed in our permanganate study was observed (49). This observation corresponds to our previous findings regarding DNAPL dissolution, where we observed that DNAPL dissolution rates in our fracture systems were 10-times less than in corresponding sand systems (32). The TCE DNAPL oxidation rate in the bench scale limestone fracture system of Tunncliffe and Thomson (33) was approximately one-third that observed in our fracture system permanganate experiment. Considering that the aqueous solubility of TCE is approximately 6-times that of PCE, our results are in reasonable agreement.

The overall rate of DNAPL mass removal was greatest in the permanganate experiment, and permanganate had a lower oxidant:PCE molar ratio than persulfate. However, the treatment duration was relatively short-lived due to plugging. The total DNAPL mass removal using persulfate with 1,000 mg/L Fe-EDTA was comparable to that of permanganate, and plugging of the fracture did not occur; however, a longer treatment time was needed. Alkaline persulfate activation was substantially less effective than Fe-EDTA activation in our experiments. Thus, despite the fact that the persulfate treatments did not plug the fracture, use of persulfate did not result in a substantial improvement in overall DNAPL mass removal compared to permanganate.

The increased rate of DNAPL treatment observed for the permanganate was due to the more rapid elution of the permanganate through the fracture compared to the Fe-EDTA activated experiments, rather than the increased aqueous phase PCE reaction rate associated with the permanganate; the slightly lower flow velocity (and corresponding increased residence time) for A2 may also have contributed to the increased treatment rate for permanganate. Similarly, the increased Fe-EDTA dosage improved DNAPL removal rates because of increased ferrous iron distribution through the fracture, rather than an increase in the aqueous phase PCE reaction rate. Ferrous iron concentrations during the first 20 days averaged approximately 40 mg/L in the fracture effluent for the 1,000 mg/L Fe-EDTA solution, but only 5 mg/L 500 mg/L Fe-EDTA solution, which is below that needed for sufficient activation (38).

As shown in Table 3-4, mass removal in C2 (persulfate + 500 mg/L Fe-EDTA) was substantially greater than in the corresponding A1 treatment with 500 mg/L Fe-EDTA. Based on the similarity in effective DNAPL-water interfacial areas (Table 5-2), water-filled fracture volume, and DNAPL dissolution rates (Section 5), a similar DNAPL mass removal rate via chemical oxidation was expected for these two systems. However, this was not observed. The difference in DNAPL removal rate via oxidation between these two systems is attributed to their differences in aperture distribution, and the location of the DNAPL sources relative to this distribution. Based on our prior assessment of the fracture aperture distributions, residual DNAPL in A1 is likely surrounded by a greater number of “small” aperture regions compared to that in C2 (Section 5). Oxidation by-products (discussed in the following section) may have obstructed flow in these small aperture regions within A1, resulting in diminished contact with DNAPL sources compared to C2. Interestingly, DNAPL mass removal in these two experiments was similar through the first 10 days, which is consistent with their DNAPL-water interfacial areas. Thus, at early times prior to significant accumulation of oxidation products that could potentially reduce contact between the oxidant and the DNAPL, the DNAPL-water interfacial area appears to control the extent of DNAPL oxidation for a given oxidant.

Comparing the DNAPL mass removal rates during bioaugmentation to DNAPL mass removal rates during chemical oxidation (Figure 8-1), the rate of DNAPL removal via chemical oxidation was substantially greater than that obtained via bioaugmentation in the experimental fracture systems through the first 20 to 40 days. However, as chemical oxidation rates decreased (due to diminished contact with the DNAPL sources, as discussed in the following section), the DNAPL mass removal rate obtained via bioaugmentation began to match or exceed the DNAPL removal rates obtained via chemical oxidation due to increases in biomass. Thus, for the conditions of our study, application of permanganate or persulfate may have less long term effectiveness for removal of DNAPL than bioaugmentation.

## 8.5 Contact with Residual DNAPL

Use of permanganate for treating DNAPL in bedrock fractures has been shown to reduce the effective fracture volume and obstruct flow near DNAPL sources (33). Consistent with this previous study, permanganate results observed herein showed complete flow obstruction through the fracture within 11 days. Based on the reaction stoichiometry in Eq. 8-2, and the mass of permanganate consumed in the fracture, up to 0.8 cm<sup>3</sup> of MnO<sub>2</sub> precipitate were generated; some of the reduced manganese may have eluted as dissolved phase due to the low pH conditions. The volume of generated precipitates comprises a very small fraction of the water-filled fracture volume (up to 0.017), but may have limited contact due to localized obstruction at the DNAPL-water interface and/or obstructed the flow through a narrow aperture region of the flow field. Based on the stoichiometry shown in Eq. 8-2, as well as the mass of PCE consumed, approximately 200 cm<sup>3</sup> of CO<sub>2</sub> were generated. While most of this volume may have dissolved into the aqueous phase, the presence of any gas bubbles may have facilitated flow obstruction.

For the persulfate experiments, fractures did not become plugged. However, as shown in Figure 8-4, the effective DNAPL-water interfacial area was reduced. This decreased DNAPL-

water interfacial area indicated that contact between the persulfate and DNAPL became substantially diminished during treatment (despite the fact that only a small fraction of the DNAPL mass was removed), and explains why persulfate became ineffective for DNAPL mass removal. While this reduction in DNAPL-water interfacial area resulted in greater than a 90% decrease in the DNAPL oxidation rates, the data in Figure 8-2 show that the DNAPL dissolution rates (post oxidation) decreased by only 30%. This observation suggests that, for the flow conditions of our experiments, mass transfer limitations were much more important during chemical oxidation than during dissolution alone. The aqueous oxidation reactions occurred very rapidly relative to the rate of dissolution, which is why the dissolved PCE concentrations in Figure 8-2 were well below their saturation values. DNAPL mass removal was limited by mass transfer into the aqueous phase, and (prior to breakthrough of the oxidant) oxidant availability. As such, efforts to increase the rate of reactivity of persulfate (or any oxidant) likely would have marginal benefits on enhancing the DNAPL dissolution. For the Fe-EDTA amended experiments, this decrease in DNAPL-water interfacial area (and corresponding decrease in DNAPL removal rate) likely was due to precipitation of ferric iron that was generated during the persulfate activation (105, 109). Analysis of the total iron in the effluent for the 500 mg L Fe-EDTA amended experiment in A1 indicated that approximately 0.3 cm<sup>3</sup> of iron (assumed in the form of Fe(OH)<sub>3</sub>) precipitated within the fracture. Based on the stoichiometry in Eq. 8-1 and the mass of PCE consumed, approximately 300 cm<sup>3</sup> of CO<sub>2</sub> was generated, which also may have contributed to the diminished DNAPL-water contact. The volume of manganese oxide precipitates was nearly 3-times that of the iron precipitates, thus serving as a plausible explanation as to why flow obstruction was more severe in the permanganate experiment compared to the Fe-EDTA-amended persulfate experiments.

The cause for the reduction in DNAPL mass removal and DNAPL-water interfacial area for the alkaline activated persulfate experiment was not readily explained. A fine orange precipitate (similar in color to that of the sandstone block) was observed after persulfate and base addition had ceased, and after the pH had returned to near neutral. Using X-ray diffraction, the precipitate was determined to be primarily ferric oxides (goethite / lepidocrocite). We speculate that localized acidity was generated via the reaction shown in Eq. 8-1. This acidity likely caused two effects. The first of which is the leaching of iron oxides from the sandstone, which were then rapidly neutralized due to the alkaline activation, which caused localized precipitation of ferric iron near the residual DNAPL sources. The second effect was that localized acidity near DNAPL inhibited the alkaline activation of persulfate and reduced oxidation effectiveness.

## 8.6 Discrete Fracture Chemical Oxidation Conclusions

Assessment of persulfate and permanganate oxidation of DNAPL sources in the discrete fracture systems has shown that chemical oxidation using either permanganate or persulfate for treatment of PCE DNAPL in sandstone fractures resulted in relatively high initial rates of mass removal. However, treatment effectiveness greatly diminished due to decreases in the effective DNAPL-water interfacial area. Decreases in the DNAPL-water interfacial area and the DNAPL removal rate were observed for all oxidants and activators examined. Results indicated that DNAPL removal is controlled by mass transfer at the DNAPL-water interface. However, the



limits of DNAPL mass removal are controlled by both the available DNAPL-water interfacial area, as well as the aperture distribution. Overall, the chemical oxidants tested were not very effective in removing DNAPL mass or substantially reducing dissolved PCE concentrations. By comparison, bioaugmentation is likely better technical and economic long term option.



## 9. RESULTS & DISCUSSION: FRACTURE NETWORK DISSOLUTION

### 9.1 Rock Matrix Characterization

#### 9.1.1 Diffusion of Solutes into Rock Matrix

Matrix diffusion calculations (described in Section 3.3.3) for  $M_w/M_f$  provided a maximum value of  $10^{-4}$  for all solutes, indicating that mass uptake into the matrix is substantially less than the rate of mass migration through the fractures and can be neglected in evaluating solute transport in the fracture network experiments.

#### 9.1.2 Adsorption on to Rock

Results of the sorption testing revealed that sorption/interaction of SDBS, PCE, and bromide to the CO Red was negligible (<5% of solute mass sorbed to the rock). In addition, we performed screening level calculations to assess the potential impact of matrix diffusion on tracer and PCE migration through the fractures.

### 9.2 Fracture Network Properties

Tracer test results were used to determine the fracture network physical properties such as, linear velocity, aperture size and variability and dispersivity were quantified using the conservative tracer tests. Bromide and SDBS tracer test elution curves were regressed to the one-dimensional advection dispersion equation using the public domain analytical transport model, CXTFIT:

$$R \frac{\partial C}{\partial t} = D_L \frac{\partial^2 C}{\partial x^2} - v \frac{\partial C}{\partial x} \quad \text{Eq. 9-1}$$

where  $R$  is the solute retardation factor (equal to one for SDBS if DNAPL is not present, and equal to one for bromide with or without DNAPL present),  $C$  is the aqueous solute concentration (milligrams per  $\text{cm}^3$ ) and  $t$  is time (minutes) and  $v$  is the linear groundwater velocity (cm/minute),  $D_L$  is the hydrodynamic dispersion coefficient ( $\text{cm}^2/\text{min}$ ) and  $x$  is the distance along the line of flow (cm). CXTFIT regression analysis was performed for all tracer tests, both with and without residual PCE DNAPL present. The co-elution of the SDBS and bromide in conservative tracer tests suggests that presence of residual air in the networks was minimal. Consistent with matrix diffusion calculations that matrix diffusion effects can be neglected without a large mass balance error, regressed elution curves for bromide exhibited an average  $R^2$  value of 0.92 (standard error of 0.02) with SDBS exhibiting an average  $R^2$  value of 0.80 (standard error of 0.03). The lower  $R^2$  value for SDBS elution curves was attributed to reconstitution of the aqueous SDBS samples prior to analysis but may also be a result of analytical limitation or sorption of SDBS to DNAPL located in dead-end fractures.

Data from bromide and SDBS tracer testing was used to quantify the aperture size and variability in terms of mass balance, frictional loss, hydraulic aperture and aperture ratio of the fracture network prior to and following DNAPL injection. Table 9-1 presents fracture network properties prior to DNAPL injection. According to Dickson and Thompson (10) the mass balance aperture provides the best estimate of the arithmetic mean aperture for the network because the mass balance aperture is sensitive to the storage of tracer in the void space of the larger fracture aperture regions. The mass balance aperture,  $e_{mb}$ , which represents an average aperture of the larger aperture regions along the flow path, is calculated as follows (82):

**Table 9-1.** Summary of fracture network properties prior to DNAPL injection

Experiment	$e_{mb}$ (cm)	$e_f$ (cm)	$\delta$	Flow Path FV (cm <sup>3</sup> )
<i>Network A</i> <i>Without DNAPL</i>	0.6 (0.06)	0.005 (0.0002)	0.008 (0.001)	353 (36)
<i>Network A</i> <b>WITH DNAPL</b>	0.7 (0.05)	0.004 (0.0001)	0.006 (0.0006)	368 (37)
<i>Network B</i> <i>Without DNAPL</i>	0.15 (0.05)	0.005 (0.0007)	0.04 (0.01)	144 (42)
<i>Network B</i> <b>WITH DNAPL</b>	<b>0.08</b> <b>(0.01)</b>	<b>0.005</b> <b>(0.001)</b>	<b>0.07</b> <b>(0.001)</b>	<b>73</b> <b>(12)</b>
(Section 5) CO Red1	<b>0.04</b>	<b>0.007</b>	<b>0.19</b>	<b>31</b>
(Section 5) CO Red2	<b>0.04</b>	<b>0.011</b>	<b>0.28</b>	<b>32</b>
(Section 5) Arizona1	<b>0.05</b>	<b>0.003</b>	<b>0.06</b>	<b>45</b>
(Section 5) Arizona2	<b>0.10</b>	<b>0.002</b>	<b>0.02</b>	<b>82</b>
(10) – Exp. 1	<b>0.13</b>	<b>0.018</b>	<b>0.14</b>	<b>205</b>
(10) - Exp 2	<b>0.10</b>	<b>0.009</b>	<b>0.10</b>	<b>61</b>

\*Flow Path FV calculated is equal to  $e_{mb}$  multiplied by the length and width of the fracture experiment. Acronyms listed in this table are defined in the text. Standard error presented in parenthesis.

$$e_{mb} = \frac{Q t_m}{LW}$$

Eq. 9-2

where  $Q$  represents the volumetric flow rate (centimeters<sup>3</sup>/minute),  $t_m$  (minutes) is the mean residence time which calculated by dividing the fracture length by the regressed linear velocity,  $L$  (centimeters) is the length of the fracture network parallel to flow and  $W$  (centimeters) is the width of the fracture network perpendicular to flow. The values for  $e_{mb}$  were used to determine flow path fracture volume (FV), where FV is equal to  $e_{mb}$  multiplied by the length and width of the fracture experiment. The frictional loss aperture,  $e_f$ , represents the average aperture of the smaller apertures of the flow path and is calculated by the following (82):

$$e_f = L \sqrt{\frac{12\mu}{\rho g \Delta H t_m}}$$

Eq. 9-3

where  $\mu$  is the dynamic viscosity (grams/ centimeter-minute),  $\rho$  is the fluid density (grams/centimeter<sup>3</sup>)  $g$  is the acceleration due to gravity (centimeters/minute<sup>2</sup>) and  $\Delta H$  (centimeters) is the hydraulic head difference across the experiment . The frictional loss aperture is sensitive to the difference in hydraulic head across the fracture network. The mass balance aperture and frictional loss apertures are then used to calculate the aperture ratio. The aperture ratio is a measure of the range of extreme aperture regions encountered along the flow path (10). The dimensionless aperture ratio,  $\delta$ , is an indicator of uniformity between the  $e_f$  and  $e_{mb}$  regions along the flow paths and is calculated as (10):

$$\delta = \frac{e_f}{e_{mb}}$$

Eq. 9-4

As described in Dickson and Thompson (10), small  $\delta$  values indicate a larger variability between the extreme aperture regions, while large values of  $\delta$  indicate a smaller variability exists between extreme aperture regions (e.g. a parallel plate fracture would have  $\delta$  equal to one). Effectively, as the value of  $\delta$  approaches one, the variability between the extreme regions of flow,  $e_f$  and  $e_{mb}$  becomes negligible.

A summary of fracture network properties with and without residual DNAPL present are provided in Table 9-1. The Network A  $\delta$  is at least an order of magnitude less than the  $\delta$  for Network B. For the Network A experiments, the flow path FV and  $e_{mb}$  values without residual DNAPL present were similar to the values with residual DNAPL present , while  $e_f$  and  $\delta$  were larger prior without residual DNAPL present. In Network B, the flow path FV and  $e_{mb}$  without residual DNAPL were greater than the values with residual DNAPL, while the  $e_f$  remained unchanged and  $\delta$  increased with residual DNAPL present. The Network A flow path FV and  $e_{mb}$  results were not expected but may be attributed to the highly variable nature of the fracture apertures within the Network A flow regime. DNAPL flow through fractures is influenced by

aperture size and roughness (110-112). The size and/or geometry of the larger aperture regions in Network A may have impeded DNAPL trapping in these regions forcing residual DNAPL to be trapped in the smaller aperture regions, which resulted in the reduced  $e_f$  with the presence of residual DNAPL. The Network B results were in accordance with what was expected since DNAPL is expected to preferentially migrate through the water-saturated fractures with larger aperture since they offer the least capillary resistance to movement.

A comparison of the fracture network  $\delta$  values to single fracture experiments indicates that there is generally a greater variability between the large and small aperture regions in network experiments compared to the single fracture experiments. Increased aperture variation contributes to larger variations in velocity distribution where flow channels develop and may become virtually independent, in the plane of a fracture (113). The comparatively large  $e_{mb}$  values with small  $\delta$  observed in the fracture network is attributed to the presence of fracture intersections in the fracture network, which do not exist in single fracture experiments. Keller et al. (61) obtained images of intersecting fractures in a granite rock core that demonstrated that fracture intersections are large aperture regions that can impact contaminant transport.

### 9.3 DNAPL Architecture in Fracture Networks

SDBS retardation relative to bromide was used to determine DNAPL interfacial area,  $a_i$ , and is calculated using the Gibbs adsorption equation (32, 75, 79):

$$a_i = \frac{(R_{SDBS} - 1)\theta}{K} \quad \text{Eq. 9-5}$$

where

$$K = \frac{M_w \theta}{R_g T \theta} \quad \text{Eq. 9-6}$$

where  $a_i$  is the DNAPL-water interfacial area ( $\text{centimeter}^2 / \text{centimeter}^3$ ),  $R$  is the SDBS retardation,  $\theta$  is the volumetric water content within the fracture ( $\text{centimeter}^3 / \text{centimeter}^3$ ).  $K$  is the sorption coefficient for SDBS at the DNAPL-water interface ( $\text{centimeter}^3 / \text{centimeter}^2$ ) in Equation 9-6, where  $M_w$  is the molecular weight of SDBS (milligrams per mole),  $R_g$  is the gas constant (Newton-meters/ Kelvin-mole),  $T$  is the temperature (degrees Kelvin), and  $\sigma$  is the PCE NAPL-water interfacial tension. Table 9-2 summarizes the DNAPL dissolution characteristics of the fracture network.

**Table 9-2.** Summary of DNAPL dissolution results for each of the fracture network dissolution experiments. Standard error reported in parentheses as applicable.

Network	Exp.	DNAPL emplaced	Aqueous Diss. Testing (days)	CXTFIT Linear velocity (cm/min) *	$S_N$	$K_L$ ( $\text{min}^{-1}$ )	$a_i$ ( $\text{cm}^3/\text{cm}^2$ )	$K_i$ (cm/min)
A	1	Influent	5	0.6 (0.04)	0.14	0.03 ( $\pm 0.01$ )	111 ( $\pm 6$ )	0.0003 ( $\pm 0.0001$ )
A	2	Influent	5	1.3	0.46	0.09	169	0.0006
A	3	Influent	5	1.0	0.27	0.03	178	0.0003
A	4	Top	100	0.3	0.13	0.02	20	0.001
B	5	Top	60	1.5 (0.3)	0.32	0.02 ( $\pm 0.01$ )	39 ( $\pm 10$ )	0.0005 ( $\pm 0.0001$ )
B	6	Top	35	1.6	0.16	0.01 ( $\pm 0.01$ )	10	0.0001
B	7	Top	12	0.7 (0.1)	0.27	0.02 ( $\pm 0.01$ )	29 ( $\pm 7$ )	0.0005 ( $\pm 0.0002$ )
B	8	Top	13	1.2 (0.2)	0.19	0.02 ( $\pm 0.01$ )	18 ( $\pm 1$ )	0.0009 ( $\pm 0.0004$ )

\*Standard Error reported in parenthesis for averaged values.

The  $a_i$  for Network A varies from 20 to 169  $\text{cm}^2/\text{cm}^3$  and the Network B  $a_i$  ranges from 10 to 39  $\text{cm}^2/\text{cm}^3$ . The variation in network experiment  $a_i$  values is attributed to DNAPL delivery method as well as  $e_{mb}$  and  $e_f$ . The mechanism of DNAPL delivery directly influences how DNAPL infiltrates the fractures and impacts DNAPL distribution within the fracture network while  $e_{mb}$  and  $e_f$  impact the trapping of DNAPL during infiltration. The lowest  $a_i$  observed in Network A was observed during Experiment 4, where DNAPL was delivered from the top influent fracture, as in the Network B experiments. The  $a_i$  from Network A Experiment 4 was within the range of  $a_i$  observed in all the Network B experiments, suggesting that the DNAPL delivery method impacted the  $a_i$ . The higher values of  $a_i$  observed in Network A (Experiments 1 through 3) may be the result of DNAPL being delivered directly into the horizontal fractures.

The average  $a_i$  and related values for the fracture network and single fracture experiments from the literature are presented in Table 9-3. The  $a_i$  values for Network A are at least twice as large as those from the analogous single fracture studies while  $a_i$  values for Network B are comparable to the single fracture studies. Our method of DNAPL delivery for the single fracture study (Section 5) was similar to the DNAPL delivery method used for Network A. Therefore, in

single fracture experiments the size of the  $e_f$  and  $e_{mb}$  aperture regions controls the volume and availability of the trapped DNAPL. Aperture is the most important factor controlling the migration of DNAPL through a single fracture (64). The similarity in  $a_i$  between our single fracture experiments (Section 5) and the Network B experiments is attributed to the similarity in  $e_f$  and  $e_{mb}$  for these experiments (Table 9-3).

**Table 9-3.** Characteristics of fracture experiments compared in this study. All values are presented as averages for fracture network experiments during DNAPL dissolution experiments.

Experiment	$S_N$	CXTFIT $D_L$ ( $\text{cm}^2/\text{min}^{-1}$ )	CXTFIT $v$ ( $\text{cm}/\text{min}$ )	$K_L$ ( $\text{min}^{-1}$ )	$K_i$ ( $\text{cm}/\text{min}$ )	$a_i$ ( $\text{cm}^3$ )	$Da$
Network-A*	0.23 (0.01)	20 (9)	0.9 (0.04)	0.05 (0.02)	0.0004 (0.0001)	117 (19)	0.04 (0.02)
Network-B*	0.25	13 (2)	0.6 (0.05)	0.02 (0.002)	0.0007 (0.0001)	28 (5)	0.0001 (0.00002)
(Section 5) CO Red1	0.24	4.4	1.5	0.03	0.001	25	0.0008
(Section 5) CO Red2	0.21	3.2	1.1	0.05	0.001	55	0.002
(Section 5) Arizona1	0.39	2.5	0.9	0.04	0.0007	56	0.003
(Section 5) Arizona2	0.43	3.5	1.2	0.01	0.0005	20	0.001
(10) – Exp. 1	0.15	3.6	1.2	0.003	N/R	N/R	0.0003
(10) - Exp 2	0.15	26.7	4.9	0.005	N/R	N/R	0.0001

\* = Fracture network standard error among all datasets from the experiments in the two fracture networks are reported in parenthesis. <sup>a</sup> Note: Our Section 5 data and the data of Dickson and Thompson (10) are single fracture experiments; for standard error in these experiments refer to original reference. <sup>b</sup> FV is the mass balance fracture volume, which is calculated by multiplying  $e_{mb}$  by length parallel to the flow path and width of the fracture(s) perpendicular to the flow path(s). The  $v$  and  $D_L$  are values regressed to the one-dimensional advection dispersion equation based on tracer test elution curves using the CXTFIT analytical transport model. N/R = data not reported.

The average  $S_N$  value was 24.8% (standard error 0.03%) for the fracture network experiments. The values of  $S_N$  for network experiments are typical of the  $S_N$  values observed in porous media studies (9, 110, 114-116) and within the  $S_N$  range presented in single fracture



experiments (10, 32). The  $S_N$  values Network A Experiments 1 through 3, which had high  $a_i$  values, were similar to the other network and single fracture experiments. This observation from Network A, combined with the flow path FV being unchanged after the introduction of residual DNAPL, suggests that DNAPL trapping in Network A experiments occurred outside the primary flow paths.

In fracture network experiments the DNAPL  $a_i$  is primarily influenced by the DNAPL delivery method while the  $S_N$  is impacted by the size of the  $e_f$  and  $e_{mb}$  aperture regions. In single fracture experiments both the  $a_i$  and the  $S_N$  appear to be influenced by size of the  $e_f$  and  $e_{mb}$  aperture regions. The DNAPL may actually be better contacted in the single fracture experiments due to the lack of intersections and limited dispersion. Dispersivity (D) was observed to be an order of magnitude greater than single fracture experiments, which is attributed to the increased availability of alternate flow paths in the fracture network setting. Once DNAPL is introduced to the fracture network experiments, aqueous flow can disperse into regions outside the primary flow path while aqueous flow in the single fracture experiments would be forced out of the fracture plane at an increased rate to accommodate the change in available pore space. Decreased uniformity between the size of the  $e_f$  and  $e_{mb}$  aperture regions in the fracture network experiments, or decreased  $\delta$ , may have lead to decreased trapping of DNAPL within the primary flow path. Interphase mass transfer from the entrapped DNAPL phase occurs by diffusive and advective transport from the DNAPL interface into the aqueous phase flowing through the fracture in the case of fractures bounded by a low porosity/permeability matrix (31). This interface where interphase mass transfer occurs is typically located at the intersection of the  $e_f$  and  $e_{mb}$  regions, as DNAPL is trapped in the  $e_{mb}$  regions (32).

#### 9.4 DNAPL Dissolution in Fracture Networks

Results of network dissolution tests are presented in Figure 9-1. The bulk dissolution mass transfer and interfacial area results for fracture network experiments are presented in Table 9-2 and the average values for each fracture network are presented in Table 9-3. Dissolution data were evaluated in terms of a bulk mass transfer coefficient and an intrinsic mass transfer coefficient. The bulk mass transfer coefficient is calculated using a steady state solution of the advection-dispersion equation, which includes a first-order, driving force expression for DNAPL-water mass transfer in the following equation (9, 32):

$$K_L = \frac{1}{4D} \left[ \left( v - \frac{2D}{x} \ln \left( 1 - \frac{C}{C_{sat}} \right) \right)^2 - v^2 \right] \quad \text{Eq. 9-7}$$

where  $K_L$  is the bulk mass transfer coefficient ( $\text{minute}^{-1}$ ), and  $C_{sat}$  is the aqueous solubility of the PCE DNAPL used in the experiment (milligrams per liter). The  $K_L$  observed in network dissolution experiments ranged from 0.03 to 0.09  $\text{min}^{-1}$  for Network A and 0.01 to 0.02 for Network B. The 0.09  $\text{min}^{-1}$  value for  $K_L$  in Network A corresponds to a high value of  $S_N$  at 0.46 during the experiment. All network experiments with an  $S_N$  of 0.14 to 0.32 exhibited values of

$K_L$  with a very small range, 0.01 to 0.03  $\text{min}^{-1}$ . The  $K_L$  values for the network experiments are comparable to those calculated for the single fracture study (Section 5) and are an order of magnitude larger than the  $K_L$  observed in the single fracture experiment by Dickson and Thompson (10). The lower  $K_L$  from the single fracture study by Dickson and Thompson compared to the fracture network are expected since the presence of fracture intersections in the network would improve mixing conditions, increasing interphase mass transfer rates. However, the similarity in  $K_L$  values between our single fracture study (Section 5) when compared to the fracture network are unexpected (due to the lack of intersections). The comparable  $K_L$  between the fracture network experiments and our single fracture study may be a result of similarity in experimental conditions  $a_i$ ,  $S_N$ , and  $e_f$  between the single fracture and the fracture network experiments. The  $K_L$  differences between the Dickson and Thompson (10) single fracture experiment and fracture network experiments may actually be driven by the  $e_f$ , since interphase mass transfer occurs at the intersection of the  $e_f$  aperture regions with  $e_{mb}$ . In addition,  $e_f$  values are the primary experimental difference between the Dickson and Thompson (10) single fracture experiments compared to the fracture network experiments and our single fracture experiments.

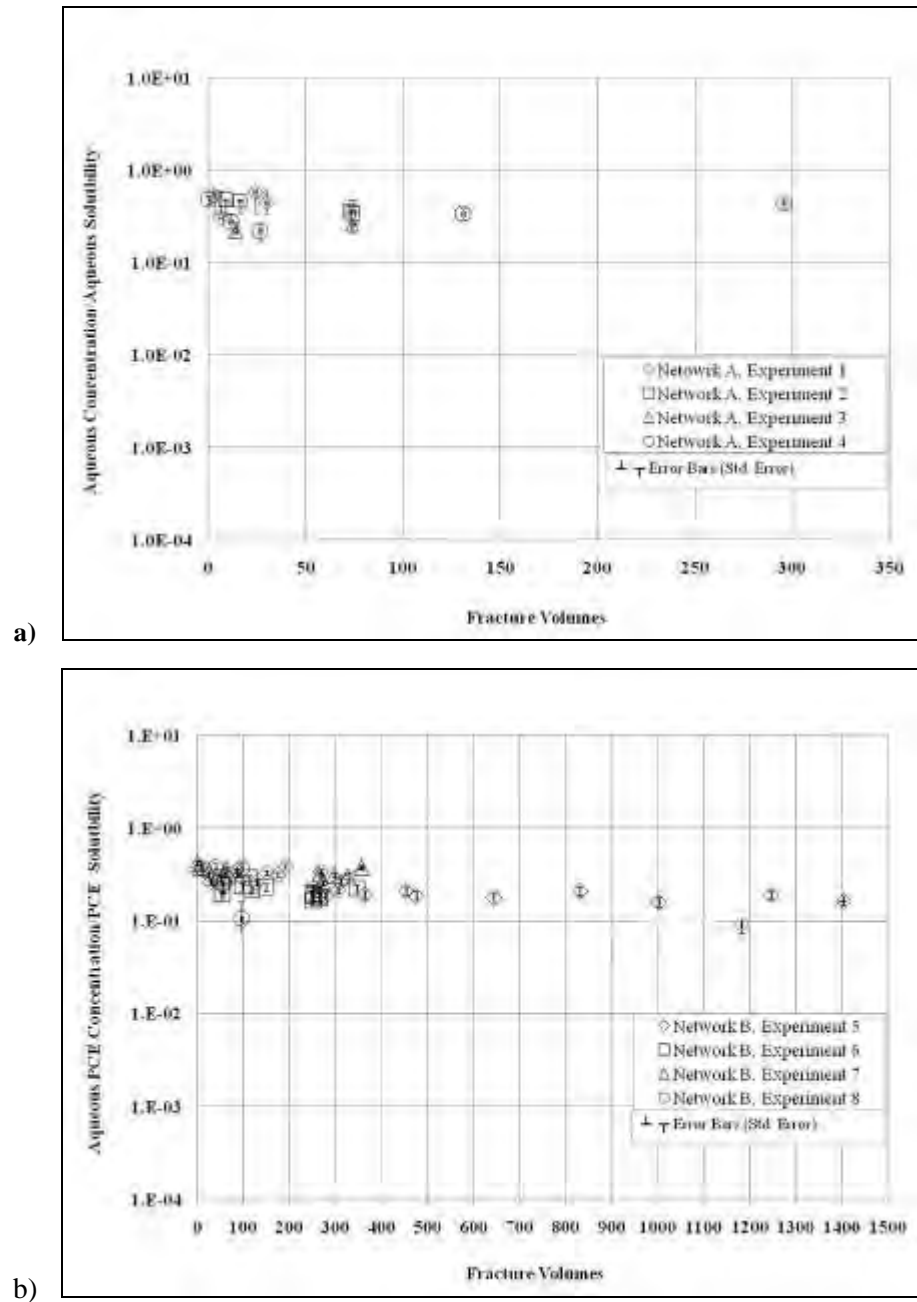


**Figure 9-1.** Aqueous phase PCE DNAPL concentrations (normalized to aqueous solubility of PCE DNAPL) plotted against fracture volumes of AGW flushed through the fracture network for a) Network A, Experiments 1 through 4 and b) Network B, Experiments 5 through 8.

The  $K_L$  (calculated from the advection-dispersion equation as described above) can be used with  $a_i$  to calculate the intrinsic mass transfer  $K_i$  (cm/min) (9, 32):

$$K_i = \frac{K_L}{a_i} \quad \text{Eq. 9-8}$$

The dissolution mass transfer descriptors ( $K_L$ ,  $K_i$ ) are commonly evaluated against the Reynolds number (Re) in fracture studies (10, 32, 116) and in porous media studies (9, 114) to facilitate a description of fluid flow and mass transport phenomena in the absence of fundamental theoretical models. Re is calculated as follows (55, 117):

$$Re = \frac{\rho v e_f}{\mu} \quad \text{Eq. 9-9}$$

where  $\rho$  is the fluid density (grams/centimeter<sup>3</sup>),  $v$  is the linear velocity (cm/min) and  $\mu$  is the dynamic viscosity (grams/ centimeter-minute). The  $e_f$  is used as characteristic length characteristic because mass transfer will occur primarily where small aperture regions intersect large aperture regions occupied by DNAPL (32). Re is useful for approximating flow through a variable aperture fracture (31) and was used in the statistical evaluation of the experimental fracture properties.

## 9.5 Statistical Evaluation of DNAPL Dissolution in Fracture Networks

Pearson product- moment correlation analysis (correlation), using JMP 8.0 statistical software was used to evaluate DNAPL dissolution descriptors ( $K_L$  and  $K_i$ ) against DNAPL dissolution properties ( $a_i$  and  $S_N$ ) and fracture experiment physical properties ( $v$ , Re,  $\alpha$ ,  $e_{mb}$ ,  $e_f$  and  $\delta$ ) for the fracture network and single fracture experiments. Pearson correlations are calculated using the following (118):

$$r = \frac{1}{n-1} \sum_{i=1}^n \left( \frac{x_i - \bar{x}}{s_x} \right) \left( \frac{y_i - \bar{y}}{s_y} \right) \quad \text{Eq. 9-10}$$

where  $r$  is the Pearson correlation,  $n$  is the number of observations,  $x_i$  and  $y_i$  are the response variables along the x-axis and y-axis, respectively;  $\bar{x}$  and  $\bar{y}$  are the average values of the x-axis and y-axis, respectively; and  $s_x$  and  $s_y$  are the standard deviations of the x and y axes. Following correlation analysis of the fracture network, the fracture network correlations are then compared to those from our single fracture experiments and those of Dickson and Thompson (10). In evaluating the datasets, correlation coefficient and significance probabilities (p-values) were used to determine the strength of the linear relationship between two variables. P-values less than 0.05 were considered statistically significant and correlative relationships between the given parameters were probable (Table 9-4).

**Table 9-4.** Summary of Pearson-product moment correlations observed in fracture experiments from DNAPL dissolution experiments. P-values less than or equal to 0.05 are considered statistically significant.

Experimental Variable	Experimental Variable	Pearson Correlation	Number of Studies	P value
$K_L$	$S_N$	0.78	7	0.03
$K_L$	$a_i$	0.76	7	0.03
$\alpha$	$e_{mb}$	0.70	7	0.05
$S_N$	$e_f$	-0.02	7	0.97
$K_L$	$e_{mb}$	0.52	7	0.19

<sup>a</sup> Single fracture analysis has four studies since interfacial area information was not reported in Dickson and Thompson (10).

In the fracture network experiments positive correlations were observed between 1)  $K_L$  with  $a_i$ ; 2)  $K_L$  with  $S_N$ ; and 3)  $\alpha$  with  $e_{mb}$ . The relationship between  $K_L$  and  $a_i$  have been repeatedly established in porous media studies (9, 80, 119). The relationship between  $K_L$  and  $a_i$  suggests mass transfer within the fracture network experiments is limited by the availability of the DNAPL interface to the aqueous flow.

Annabelle et al (80) described  $a_i$  as the primary determinant of NAPL removal efficiency. The relationship positive correlation between  $\alpha$  and  $e_{mb}$  maybe related to the presence of fracture intersections in the fracture network setting. As described by Bear et al. (120), an increase in the number of fracture intersections aligned along the hydraulic gradient leads to longer contaminant arrival times, and greater macroscopic dispersion. A porous media study by Miller et al. (121) also determined  $K_L$  was directly related to  $S_N$  and aqueous phase velocity. The corresponding relationship between  $S_N$  and  $K_L$  in the fracture network would be expected, as aqueous saturation is reduced and replaced with DNAPL phase, the increased presence of DNAPL would yield increased steady state  $PCE_{aq}$  concentrations which would increase  $K_L$ . Statistical evaluation of velocity testing conducted during Experiment 1 in Network A was also performed. During the velocity test, the changes in effluent  $PCE_{aq}$  concentrations were evaluated against changes in velocity while all other experimental parameters remained constant; statistical analysis revealed a positive trending, though statistically insignificant, relationship existed between  $v$  and  $K_L$  in the fracture network ( $R^2=0.69$ ). The lack of statistically significant correlation between  $K_L$  and  $v$  in the fracture network analysis was unexpected but may result from the presence of fracture intersections. Park et al (53) determined that flow and transport in 3-D fracture intersections may contribute to the re-distribution of solute according to the mixing rule and/or the delay of solute in local flow cells. The influence of these local flow cells in the fracture network may diminish the influence of velocity in the fracture network. Preferential flow through flow paths that are

saturated (with respect to dissolved PCE), and therefore may not vary with flow velocity, also may contribute to this lack of observable correlation.

## 9.6 Fracture Network DNAPL Dissolution Conclusions

Two experimental low porosity fracture networks were used to investigate and quantify steady state DNAPL dissolution kinetics and were compared to findings from two single fracture experiments in the literature. The fracture network relationships observed in this study reveal that DNAPL dissolution kinetics within the fracture network experiments is primarily influenced by  $S_N$  and  $a_i$ . The correlation between  $K_L$  and  $a_i$  in the fracture network experiments indicates  $K_L$  is limited by the availability of the DNAPL interface to the aqueous flow. The presence of fracture intersections increased experimental dispersivity and appears to have diminished the quantifiable correlation between velocity or aperture with dissolution kinetics in the fracture network experiments. This fracture intersection assertion is supported by the observed correlation between aperture size with  $K_L$  and  $S_N$  in the single fracture experiments, where fracture intersections are absent.

Dissolution mass transfer in fractured network setting, similar to porous media experiments, is primarily dependant on the volume of DNAPL in the network how well contacted it is with the flowing aqueous phase. Aperture size and uniformity appear to influence DNAPL trapping and interfacial area, but the aperture properties appear to only secondarily affect DNAPL dissolution in a fractured network setting. Detailed characterization of the impact fracture intersections, aperture size and aperture uniformity have on  $K_L$  at specific velocities and DNAPL saturations in a three-dimensional fracture network setting may further clarify variation of mass transfer often observed in field settings.



## 10. RESULTS & DISCUSSION: FRACTURE NETWORK BIOAUGMENTATION

### 10.1 Fracture Network Bioaugmentation

Results for the fracture network bioaugmentation experiment are present in Figure 10-1. Initial bioaugmentation results showed a decrease in effluent dissolved PCE concentrations (although a declining trend in PCE concentration was observed prior to bioaugmentation, thus it is unclear as to the extent to which bioaugmentation impacted dissolved PCE concentrations) and an accumulation of relatively low concentrations of *cis*-DCE. Low levels of dissolved ethene and TCE also were observed in the effluent. Vinyl chloride (VC) was not observed in the effluent until the very end of the 310-day experiment. The primary daughter products detected were *cis*-DCE and ethene, which is consistent with results obtained in the discrete fracture experiments (Section 6).

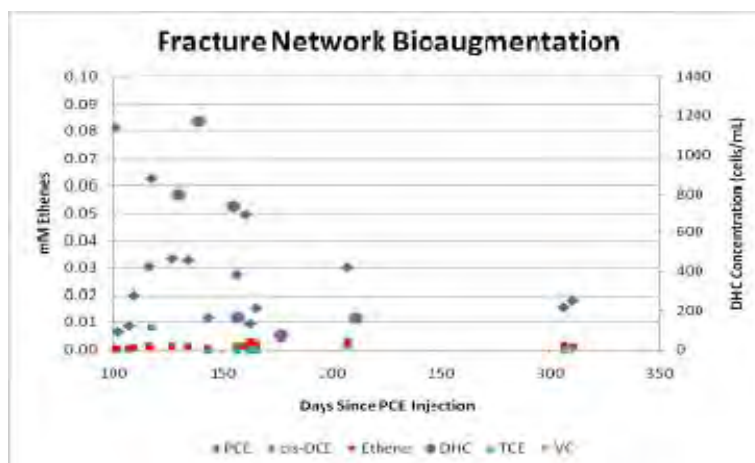


**Figure 10-1.** Fracture network bioaugmentation. Bioaugmentation occurred at t=100 days.

Figure 10-2 shows measured effluent chloride concentrations compared to theoretical chloride concentrations, where the theoretical chloride concentrations were calculated stoichiometrically based on the molar quantities of TCE, DCE, VC, and ethene generated. Similar to the results observed in the discrete fracture experiments (Section 6), the measured rate of chloride generation was much greater than the chloride generation rate based on chlorinated ethene and ethene daughter products. This is attributed to back-partitioning of the chlorinated ethene and ethene daughter products into the DNAPL, thereby causing an under-estimate of the extent of dechlorination based on the presence of these compounds in the aqueous phase. The discrepancy between the theoretical and measured chloride concentrations is several times greater in the fracture network experiment than in the discrete fracture experiments, thereby

indicating that mass transfer between the bulk aqueous phase where dechlorination is occurring and the DNAPL is much greater in the fracture network in the discrete fractures.

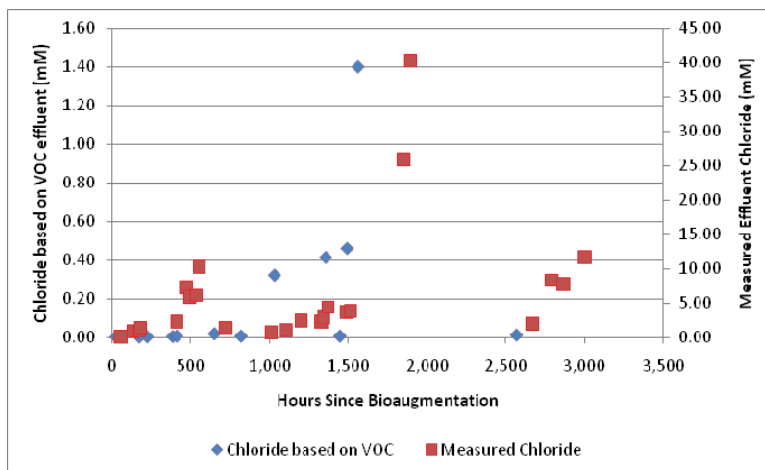


**Figure 10-2.** Chloride generation during the fracture network bioaugmentation experiment. Theoretical chloride generation is based on the amount of daughter products (TCE, DCE, VC, and ethene) generated.

Applying the chloride-based DNAPL dissolution enhancement factor developed for the discrete fracture experiments (Eq. 6-1), a DNAPL dissolution enhancement factor of 3.1 is calculated for the fracture network. This enhancement factor falls within the range of those for the discrete fracture bioaugmentation experiments. Thus, bioaugmentation is effective for enhancing the removal of DNAPL sources in a fracture network. Similar to the discussion for discrete fractures in Section 6, enhancement factors at the field scale likely would be substantially greater.

Overall DNAPL mass removal prior to bioaugmentation (i.e., prior to day 100 in Figure 10-1) was 8.4% of initially emplaced DNAPL mass, which was removed via abiotic dissolution into the aqueous phase. During the first 100 days post-augmentation, 12.5% of the initially emplaced DNAPL mass was recovered (sum of dissolved PCE and PCE-equivalents present as chloride). After 310 days (100 days abiotic dissolution and 210 bio-enhanced dissolution), a total of 30.5% of the initially emplaced DNAPL mass was recovered. Thus, these results confirm that DNAPL dissolution was enhanced as a result of bioaugmentation.

The dotted lines in Figure 10-3 represent the flow during the bioaugmentation experiments and illustrate periods of interrupted flow due to leakage caused by pressure buildup from deposits blocking the effluent tubing. As indicated by the ovals in the figure, there are peaks in effluent chloride concentrations immediately following the return of flow through the system. In order to evaluate if these peaks in concentration were due to a build-up within the system during

interrupted flow that is washed out when flow is returned, the measured chloride data was first compared to the theoretical chloride concentrations in order to see if the spikes appeared in both sets of data. This was done to eliminate the possibility of a chloride analytical error. A chloride generation rate was then calculated for the periods prior to each period of no flow. Assuming the chloride generation rate was constant during times of no flow, the amount of mass generated within the system was calculated and compared to the mass recovered once flow was returned (Table 10-1). For the first spike in chloride, the mass recovered post flow-stop (0.31 mol) is in reasonable agreement with the calculated chloride mass generation during the time of no flow (0.25 mol). For the second spike, the calculated mass generated was roughly 0.51 mol; however, the mass recovered was only 0.19 mol. This discrepancy is likely due to the almost back-to-back stops in flow (Figure 10-3) that made capturing all the mass generated nearly impossible. These calculations suggest that these spikes in effluent concentrations are due to the build-up during interrupted flow and are not representative of other phenomena occurring within the system.

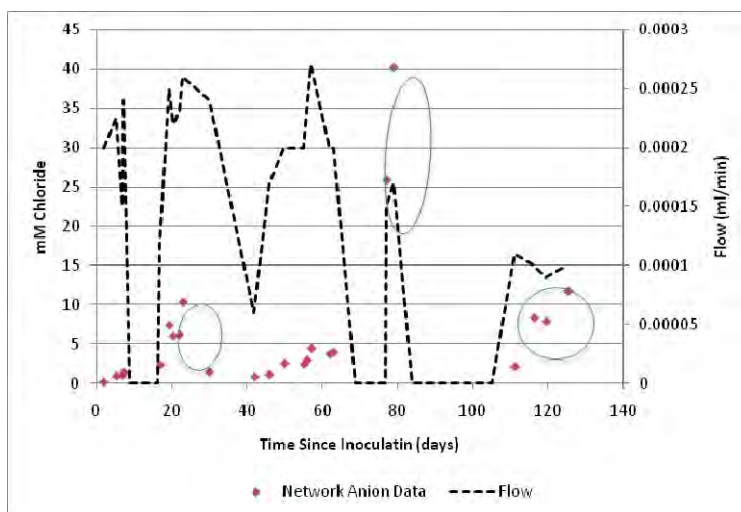


**Figure 10-3.** Chloride generation correlated to flow (and flow stoppages) during the fracture network bioaugmentation experiment.

**Table 10-1.** Chloride concentration spike assessment.

Chloride Spike Investigation				
	Rate Prior to No Flow	Conc. Of Chloride	Chloride Mass	Chloride Mass Recovered
	mM/day	Generated during No Flow*	Generated	during spike (mol)
Spike 1	0.10	0.90	0.31	0.25
Spike 2	0.21	1.46	0.51	0.19
*Assuming rate of Chloride generation remains constant				

## 11. RESULTS & DISCUSSION: FRACTURE NETWORK CHEMICAL OXIDATION

The effluent  $PCE_{aq}$  and chloride concentration data, interfacial areas, and mass transfer coefficients obtained from these experiments were used to evaluate the effectiveness of KISCO for removing PCE DNAPL in the fracture network setting, and the KISCO-related changes in mass-transfer. The results are discussed in terms of mass removal, implications to mass transfer, the formation of reaction byproducts and post-KISCO evaluation.

### 11.1 Mass Removal during KISCO

PCE mass removal during KISCO was evaluated relative to mass removal from steady state DNAPL dissolution prior to KISCO to determine if KISCO improved PCE mass removal in the fracture network (i.e., compare KISCO to pump-and-treat). In addition, the mass removal results for each experiment are compared to the other KISCO experiments. The mass removed during the fracture network KISCO experiments is evaluated against analogous experiments from the literature.  $PCE_{aq}$  concentrations relevant to the dissolution calculation are presented in Figure 11-1(a -c). The maximum decrease in effluent  $PCE_{aq}$  concentrations during KISCO was: 88 % for KISCO-1; 99% for KISCO 2a; and 71 % for KISCO 2b. During KISCO-3 the effluent  $PCE_{aq}$  concentrations were not observed to decrease. A summary of the results from KISCO applications in the experimental fracture network are summarized in Table 11-1.

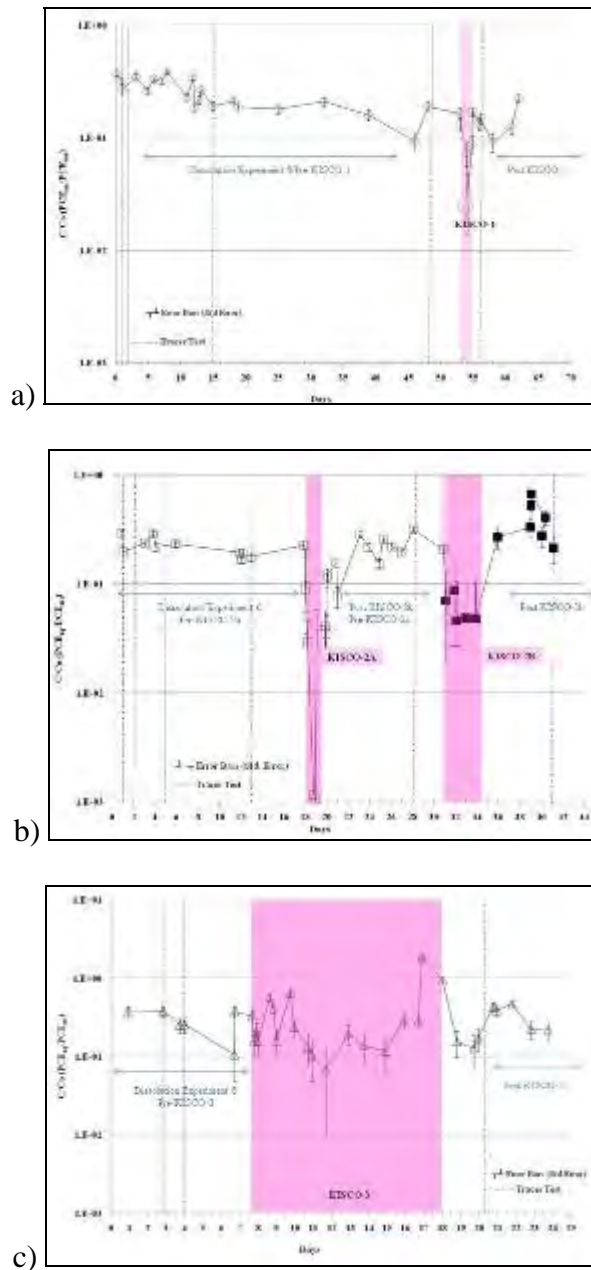


**Figure 11-1 (a.-c.).** Aqueous phase PCE concentrations prior to KISCO, during dissolution testing, during KISCO (pink regions) and following KISCO: a) KISCO- 1; b) KISCO-2a and 2b; c) KISCO-3. Point of interfacial area tracer testing is indicated by dashed line (tracer tests were completed within 4 hours). Error bars represent the standard error of the data point (standard deviation of the concentration from the mean concentration of all the samples collected from the pre-KISCO samples).

**Table 11-1.** Experimental conditions of KISCO applications in the fracture network.

	KISCO-1	KISCO-2A	KISCO-2B <sup>a</sup>	KISCO-3
Average Pre-KISCO Effluent PCE <sub>aq</sub> Concentrations (mg/L)	43 (±3.0 mg/L) <sup>a</sup>	38 (±2.2 mg/L)	32 (±4.0 mg/L)	51 (±7.8 mg/L)
Average Pre-KISCO Mass Removal Rate or MRR <sub>D</sub> (mg/day)	226 (±15 mg/day)	176 (±36 mg/day)	99 (±13 mg/day)	158 (±22 mg/day)
Experimental velocity (cm/min)	1.5	1.5	1.7	1.2
Permanganate concentration (g/L)	7.5	7.5	1.5	1.5
Duration of KISCO application (days)	1.6	2.1	4.8	10.3
Duration of effective KISCO (days)	0.5	2.0	0.6	0.2
Fracture Volumes of KISCO Applied	47	30	69	147

Notes: <sup>a</sup>Standard error reported in parenthesis beneath value, where appropriate.

Mass removal rates from KISCO experiments are presented in Figure 11-2 (a -c) and results are summarized in Table 11-1. The range of peak PCE mass removal rates achieved during KISCO applications was between 350 milligrams removed per day (mg/day) to 1100 mg/day. Typically, the PCE removal rate reached the maximum rate within the first day of KISCO application and was maintained for less than 1 hour. During both KISCO-1 and 2, the removal rate decreased rapidly once the peak rate was reached. During KISCO-3 the PCE removal rate decreased gradually and was probably due to the lower oxidant concentration applied which decreased reaction byproduct formation. A collective comparison of factors impacting oxidation and dissolution is further developed in Section 11.4. The maximum mass removal rate for KISCO-1 was 425 mg/day with 100 mg of total PCE DNAPL mass removed (Figure 11-2a), which was equivalent to 0.1% of the mass of PCE DNAPL present in the fracture network. The maximum PCE DNAPL mass removal rate observed was 1100 mg removed/day during KISCO-2a, with 868 mg of total PCE DNAPL mass removed (Figure 11-2b), which represented 1.8 per cent of total residual PCE DNAPL present in the fracture network. The second application in KISCO-2, KISCO-2b, had a maximum mass removal rate of 308 mg removed/day with 96 mg of PCE DNAPL mass removed, representing 0.2% of the total DNAPL mass present in the fracture network. KISCO-3 had a maximum mass removal rate of 425 mg/day with 60 mg of PCE DNAPL mass removed, representing 1.3% of the total PCE DNAPL mass present in the fracture network (Figure 11-2c).



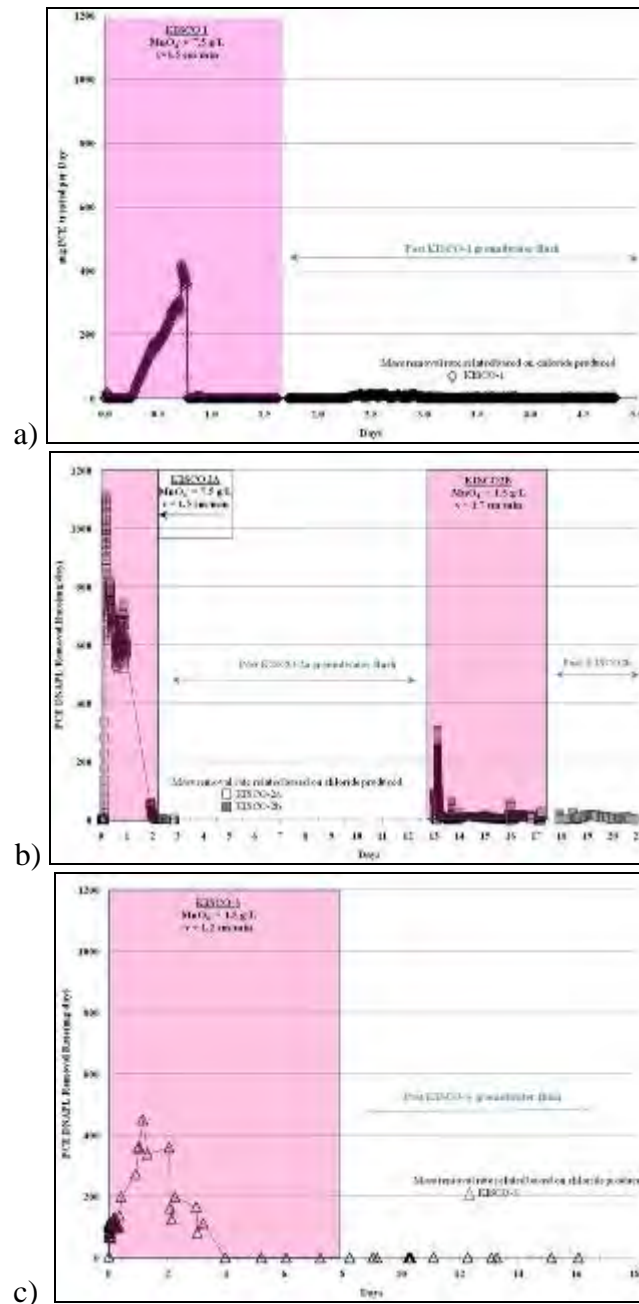


**Figure 11-2.** PCE DNAPL mass removal rates during KISCO: a) KISCO- 1 at  $7.5 \text{ g/L MnO}_4^-$  and  $1.5 \text{ cm/min}$  linear velocity; b) KISCO-2a at  $7.5 \text{ g/L MnO}_4^-$  and  $0.7 \text{ cm/min}$  linear velocity and KISCO-2b at  $1.5 \text{ g/L MnO}_4^-$  and  $0.7 \text{ cm/min}$  linear velocity c) KISCO-3 at  $1.5 \text{ g/L MnO}_4^-$  and  $0.7 \text{ cm/min}$  linear velocity. Error bars represent the standard error of the data point (standard deviation of the concentration from the mean mass removal rate observed during dissolution).

To evaluate whether KISCO improved mass removal rates compared to steady state dissolution the enhancement factor was evaluated. KISCO-1, KISCO-2b and KISCO-3 all exhibited low enhancement factors (0.3, 0.2, 0.5, respectively) indicating that more PCE DNAPL mass would have been removed had steady state dissolution conditions remained (Table 11-2). However, the enhancement factor for KISCO-2a was 2.5, indicating that increased PCE mass was removed during KISCO-2a compared to dissolution experiments. The increased enhancement factor during KISCO-2a was attributed to the KISCO application being terminated shortly after decreased effectiveness of KISCO was observed (once chloride reductions reached background levels). Therefore, each experiment that exhibited low enhancement factors were reevaluated using only the period of time when KISCO was effective to determine if improved enhancement would have been obtained during the shorter duration.

**Table 11-2.** Mass removal comparison and post-KISCO conditions from KISCO applications.

	KISCO-1	KISCO-2A	KISCO-2B	KISCO-3
PCE DNAPL Mass removed during KISCO (g)	0.10	0.87	0.09	0.80
PCE DNAPL Mass removed by dissolution had KISCO not been applied. Calculated using $MRR_D$ (g)	0.37	0.37	0.48	1.62
Post-KISCO aperture (cm, pre-acid, peroxide and ethanol flush)	0.10	0.03	0.02	0.03
% decrease in aperture following KISCO	0%	50%	33%	50%
Average Post-KISCO Effluent $PCE_{aq}$ Concentrations (mg/L)	26 ( $\pm 3.2$ mg/L) <sup>a</sup>	32 ( $\pm 4.0$ mg/L)	71 ( $\pm 12.1$ mg/L)	48 ( $\pm 8.3$ mg/L)
Average Post-KISCO Mass Removal Rate or $MRR_D$ (mg/day)	78 ( $\pm 23$ mg/day)	96 ( $\pm 13$ mg/day)	214 ( $\pm 82$ mg/day)	145 ( $\pm 33$ mg/day)
KISCO Enhancement Factor 1 (duration of KISCO)	0.3	2.5	0.2	0.5
KISCO Enhancement Factor 2 (during effective KISCO removal only)	0.8	2.5	1.5	27.2

Notes: <sup>a</sup>Standard error reported in parenthesis beneath value, where appropriate.

To assess the duration of time when KISCO was effective for each of the applications, the time period where chloride produced was above 10% of background chloride (experiment dependant but generally between 2 and 10 mg/L) was selected and recalculated as “Enhancement Factor 2” (Table 11-2). Once the ineffective time of KISCO application was removed, the enhancement factor for KISCO-2b and 3 increased from below 1 to 1.53 and 27.2, respectively.

These numbers indicate that if the KISCO application was ceased once chloride was no longer being produced (from PCE removal) that the KISCO would have successfully removed more PCE than dissolution alone. Effectiveness was significantly improved in the case of KISCO-3 (a low oxidant concentration application) and even for the sequential KISCO application, which was previously believed to be ineffective. The KISCO-1 application remained ineffective compared to dissolution alone. The reasons for the ineffectiveness of KISCO-1 may result from the distribution of DNAPL in KISCO-1.

### 11.2 Sequential KISCO experiment

The sequential KISCO application, KISCO-2b, was used to determine if reaction byproducts from the prior KISCO application affected the efficiency of the subsequent KISCO applications. Potentially, flushing the network with AGW could remove a sufficient volume of byproducts that increased mass removal would be achieved again. However, it was hypothesized that persistence of reaction byproducts in the fracture network would limit KISCO effectiveness for a sequential application. A reduced KISCO concentration in KISCO-2b (1.5 g/L  $\text{MnO}_4^-$ ) was used to minimize formation of reaction byproducts. As a result of oxidation byproduct formation during KISCO-2a, the average fracture aperture had decreased by 50% prior to KISCO-2b (Table 11-2), suggesting significant byproduct formed during KISCO-2a and remained in the network during the KISCO-2b application. Prior to KISCO-2b, effluent  $\text{PCE}_{\text{aq}}$  rebounded to steady state concentrations. However, once the 1.5 g/L  $\text{MnO}_4^-$  was introduced during KISCO-2b, effluent  $\text{PCE}_{\text{aq}}$  steadily declined to the concentrations previously observed in KISCO-2a until the KISCO-2b application ceased (Figure 11-2b). The cause of the rebound in post-KISCO-2a  $\text{PCE}_{\text{aq}}$  is discussed in Section 11.5. The reestablished reduction in contact between the oxidant and PCE DNAPL during KISCO-2b (likely due to reaction byproducts being re-deposited at the DNAPL interface), indicates that though sequential KISCO applications removed additional DNAPL mass from the fracture network the mass did not exceed what would be expected from dissolution alone in the experimental setting. However, as previously, if the sequential KISCO application had been ceased once increased chloride production was no longer observed, the sequential application would be considered effective (enhancement factors, Table 11-2). Interestingly, the post-KISCO-2b  $\text{PCE}_{\text{aq}}$  concentrations rebounded to more than double the pre-KISCO-2b concentrations. Therefore, as discussed in Section 11.5, the DNAPL-water mass transfer actually increased following KISCO-2b, which was unexpected because reaction byproducts have been commonly observed to cause mass transfer limitations during KISCO.

### 11.3 Fracture Network Mass Removal Compared to Four Literature Studies

KISCO mass removal in four different experimental systems reported in the literature were evaluated, including two single-fracture experiments (discrete fracture study presented in Section 8, and in Tunnicliffe and Thomson (33)) and three porous media studies (42, 49, 50). For all experiments evaluated, the experimental mass removed was normalized by the solubility of the DNAPL (~200 mg/L for PCE and 1100 mg/L for TCE) and the specific experimental fracture or pore volume reported.

In the single fracture KISCO study results presented in Section 8, approximately 1100 mg of PCE was removed at 10 g/L  $\text{KMnO}_4$  and a linear velocity of 3.2 cm/min. As presented in Table 11-3, the normalized mass removed for the experiment was 67 (unitless). In the fracture network experiments, the normalized mass of PCE DNAPL oxidized during KISCO-1 was 5.8, KISCO-2a was 51, KISCO-2b was 10 and for KISCO-3 was 77 (Table 11-3). The normalized mass of PCE removed in the fracture network experiments KISCO-2a and -3 was comparable to the normalized mass removed in the single fracture experiments (Section 8). The KISCO-1 and -2b normalized masses removed were an order of magnitude less than the mass removed in the single fracture permanganate experiment (Section 8) but were similar to the normalized mass removed in the single fracture experiments by Tunnicliffe and Thomson (33). In the two vertical single fracture KISCO experiments by Tunnicliffe and Thomson (33), a total of 220 mg and 180 mg of PCE were removed in 50 day and 70 day experiments, respectively (using 10 g/L  $\text{KMnO}_4$  or 7.5 g/L  $\text{MnO}_4^-$ ). The normalized masses removed equate to 8.7 and 4.1, respectively. Generally, the normalized mass of PCE removed during KISCO in the fracture network experiments was within the range of normalized mass removed in the single fracture experiments. Potentially, the distribution and increased interfacial area of DNAPL during KISCO-1 and persistence of reaction byproducts in KISCO-2b may have potentially limited mass transfer more rapidly than in the subsequent experiments.

**Table 11-3.** Summary of the mass removed by experiment normalized to the experimental fracture volume. For experimental volume, volume of void space for the reaction to occur in the experiment was used.

	<b>Experiment Description</b>	<b>DNAPL (solubility mg/L)</b>	<b>Experimental Fracture or Pore Volume (L)</b>	<b>Mass removed (mg)</b>	<b>Normalized Mass removal</b>
KISCO-1	Fracture Network	PCE (176) <sup>a</sup>	0.094	96	5.8
KISCO-2a	Fracture Network	PCE (176)	0.096	868	51.4
KISCO-2b	Fracture Network	PCE (176)	0.049	87	10.1
KISCO-3	Fracture Network	PCE (176)	0.060	816	77.3
Discrete Fracture (Section 8)	Single Horizontal Fracture	PCE (200)	0.082	1100	67.1
Tunncliffe and Thompson, (33) (Frac I)	Single Vertical Fracture	TCE (1100)	0.023	220	8.7
Tunncliffe and Thompson, (33) (Frac II)	Single Vertical Fracture	TCE (1100)	0.040	180	4.1
Petri et al. (49)	1D porous media	PCE (200)	0.023	443	96.3
Heiderscheidt et al. (42)	2D porous media	PCE (200)	1.181	6097	25.8

<sup>a</sup>PCE solubility is 176 mg/L for the fracture network experiments (as opposed to 200 mg/L for the other PCE experiments) because it was experimentally determined for the specific PCE DNAPL batch used.

Two porous media KISCO experiments were compared to the fracture network experimental results. The normalized mass PCE oxidized using KISCO in a one-dimensional (1D) residually saturated porous media study by Petri et al. (49), was similar to the KISCO-2a and KISCO-3.

The normalized mass from the Petri et al. (49) experiment, which had comparable experimental  $S_N$ ,  $MnO_4^-$  concentrations and groundwater velocities to KISCO-2b, was approximately 1.5 times normalized mass of KISCO-2a. In a two-dimensional (2D), residual pooled DNAPL porous media tank experiment by Heiderscheidt et al. (42) using an  $MnO_4^-$  concentration of 2.1 g/L (similar to KISCO-3), the normalized mass of PCE removed per experimental volume, 4.0 mg/ml was comparable to the amount of PCE removed in the fracture network during the less effective KISCO applications, KISCO-1 and KISCO-2b. The velocity of the Heiderscheidt et al. (42) experiment was not reported so a velocity comparison cannot be made. Based on these literature data sets, the normalized DNAPL mass removals appear to be within a similar range for the fracture and porous media KISCO experiments evaluated. The slight differences in mass removals for porous media experiments and fracture network experiments may result from morphology of the emplaced DNAPL (the pooled porous experiment had lower mass removals) and/or solute mixing in the fracture network increasing the formation of reaction byproducts,  $MnO_2$  and  $CO_2$  and inhibiting enhanced mass transfer from oxidation.

#### 11.4 DNAPL Dissolution Mass Transfer during KISCO in Fracture Networks

To analyze the impact of KISCO on DNAPL dissolution, the observed changes in bulk mass transfer coefficient ( $K_L$ ) prior to and following KISCO are evaluated. Tunnicliffe and Thompson (33), determined that permanganate flushing of DNAPL source zones in fractured rock may offer some beneficial results since the development of an insoluble product adjacent to DNAPL within a fracture could effectively encapsulate portions of the free phase and reduce the ability of the remaining DNAPL to generate a plume. However, limited beneficial impacts to dissolution were observed in the fracture network experiments. The pre- and post-KISCO  $K_L$  values are presented in Table 11-4 for each KISCO experiment. Post-KISCO  $PCE_{aq}$  concentrations (and  $K_L$ ) rebounded rapidly to pre-KISCO conditions following the end of the KISCO application (Figure 11-1, a-c) therefore the post-KISCO  $K_L$  values represents post-rebound conditions. The pre-KISCO  $K_L$  for the KISCO experiments, with the exception of KISCO-2b, the sequential experiment, was larger prior to KISCO application. However, the reduction in  $K_L$  following KISCO in the network experiments was not large. KISCO-1 removed the least PCE mass and the greatest reduction in  $K_L$  was observed (~58% decrease was observed). During KISCO-2a and KISCO-3, the decrease observed was 17 and 18%, respectively, suggesting limited impact of KISCO on  $K_L$  or encapsulation of the DNAPL. However, the  $K_L$  unexpectedly increased by 250% percent following the sequential KISCO application, KISCO-2b. Possibly, the increase in  $K_L$  following KISCO-2b resulted from a shift in preferential flow paths, to previously uncontacted regions of the fracture network, that resulted from the build up of reaction byproducts in the sequential experiments. The shift in preferential flow paths may have enabled the aqueous flow to access DNAPL zones that were not as hydraulically accessible (smaller aperture regions outside the primary flow paths) prior to KISCO-2b. An increase in post-KISCO effluent concentrations was also observed in Heiderscheidt et al. (42), which was attributed to  $MnO_2$  deposition around co-located residual pool sources creating more complex flow patterns, increasing mixing and maintaining flow in contact with adjacent residual DNAPL. Heiderscheidt et al. (42), proposed that increases in  $PCE_{aq}$  following oxidation resulted from a combination of source mass depletion



and changes in source mass depletion rates due to changes in the flow field due to  $\text{MnO}_2$  deposition.

Urynowicz and Siegrist (51) found the effects of interfacial  $\text{MnO}_2$  deposition may be more pronounced under increased mixing conditions, because mixing may increase the rate of interfacial mass transfer. Increased mixing was expected in the fracture network as a result of fracture intersections within the flow field. Correspondingly, Park et al. (53) determined that flow and transport in 3-D fracture intersections may contribute to the re-distribution of solute according to the mixing rule and/or the delay of solute in local flow cells. Mixing at the fracture intersections in the fracture network would have increased reaction byproduct formation and decreased DNAPL mass removed compared to the porous media experiments. This assertion is supported by the immeasurable interfacial area following each KISCO applications (Table 11-4). Increased mixing was expected to increase oxidant byproduct formation in the fracture network, which would impact flow fields. The decrease in  $K_L$  following KISCO-1 may have from  $\text{MnO}_2$  formed at the DNAPL-water interface, and/or within the source zone causing flow bypassing, effectively cutting off mass flux. The reason for increased  $\text{MnO}_2$  formation during KISCO-1 is unclear, particularly in the absence of increased PCE mass removal; however, it may be related to the larger interfacial area observed prior to the KISCO-1 application.

**Table 11-4.** Impacts of KISCO on fracture network dissolution

	KISCO-1	KISCO-2A	KISCO-2B	KISCO-3
DNAPL-Water Interfacial Area Pre-KISCO ( $\text{cm}^2/\text{cm}^3$ )	39 (10)	10	<i>nm</i>	19 (1)
DNAPL-water interfacial area Post-KISCO ( $\text{cm}^2/\text{cm}^3$ ) <sup>a</sup>	<i>nm</i>	<i>nm</i>	<i>nm</i>	<i>nm</i>
Bulk Mass Transfer Coefficient Pre-KISCO ( $\text{min}^{-1}$ )	0.019 (0.01)	0.012 (0.006)	0.014 (0.05)	0.017 (0.02)
Bulk Mass Transfer Coefficient Post-KISCO ( $\text{min}^{-1}$ )	0.008 (0.001)	0.010 (0.001)	0.049 (0.002)	0.014 (0.001)
Measured $\text{MnO}_2$ generated(g) <sup>b</sup>	n/a	6.4	0.6	1.1
Expected $\text{MnO}_2$ in system (g) <sup>c</sup>	9	22.6	6.1	10.8
Calculated $\text{CO}_2$ generated (ml)	29	250	27	235

<sup>a</sup> Post-KISCO interfacial area was not measureable (*nm*) for all experiments and is attributed to reaction byproducts. Standard error is reported in parenthesis beneath the value and is listed in the same units as the value. <sup>b</sup> KISCO consumption was not monitored during KISCO-1, n/a indicates not available. <sup>c</sup> Expected  $\text{MnO}_2$  in system was calculated based on reaction stoichiometry and measured  $\text{MnO}_4^-$  consumed for each experiment.

### 11.5 Relating Changes in Interfacial Area to Dissolution in KISCO Fracture Networks

Based on the KISCO and fracture network dissolution discussion, the influence of  $a_i$  on changes in mass transfer behavior resulting from KISCO becomes apparent. It is necessary to examine the changes in  $a_i$  prior to and following KISCO. Interfacial area tracer testing was conducted before and after the KISCO applications. The timing of tracer testing relative to KISCO applications (and dissolution experiments) is represented by the vertical dashed lines in Figures 11-1 (a –c). The post-KISCO interfacial area tracer results were compared to the pre-KISCO steady state dissolution conditions to determine if changes in  $a_i$  were observable. Post-KISCO interfacial area tracer testing was conducted once all  $\text{KMnO}_4$  had been flushed from the fracture network, at least two days following return to AGW (as indicated the in Figures 11-1, a -c) to eliminate interference of the KISCO with the tracer solution analyses. Following each KISCO application, the  $a_i$  was not measurable in the fracture network experiments (Table 11-4). This result was surprising since less than 5% of the DNAPL was removed and, following the return to AGW,  $\text{PCE}_{\text{aq}}$  concentrations rapidly rebounded to previously established steady-state concentrations (prior to tracer testing) and were continued for the remainder of the experiments (Figure 11-1, a-c). The immeasurable  $a_i$ , combined with the rebound in  $\text{PCE}_{\text{aq}}$  concentrations, appear to be contradictory. A decrease in effluent  $\text{PCE}_{\text{aq}}$  concentrations would be expected with the  $a_i$  reduction.

Rebound of effluent  $\text{PCE}_{\text{aq}}$  concentrations, in the absence of measurable  $a_i$ , was likely related to preferential flow paths established (or altered) from the deposition of reaction byproducts and DNAPL trapped in the fracture network, outside the primary flow paths, adjacent to the effluent manifold (Figure 3-8). Furthermore, this finding explains the divergence of  $\text{PCE}_{\text{aq}}$  concentration and mass removal rates observed in KISCO-3 (Figure 11-1c). During KISCO-3, as in all KISCO applications, the effluent chloride concentrations and PCE DNAPL mass removal rates were observed to peak and drop off as the formation of reaction byproducts limited the oxidation of dissolved phase DNAPL in the primary flow path of the fracture network (Figures 11-2a through c). However, formation of reaction byproducts formed during KISCO did not reduce the  $\text{PCE}_{\text{aq}}$  mass flux from DNAPL pooled in areas outside of the primary flow path that were located adjacent to the effluent manifold in the fracture network. The observed rebound in effluent  $\text{PCE}_{\text{aq}}$  concentrations following KISCO, with no measurable  $a_i$ , was attributed to the DNAPL adjacent to the effluent. The heterogeneous nature of the flow paths, combined with the DNAPL located outside the primary flow path of the interfacial area tracer (and probably lingering  $\text{MnO}_2$  in the fracture network), likely inhibited sorption of the interfacial area tracer to the DNAPL interface while allowing effluent concentrations to readily rebound.

The  $a_i$  may also be related to the mass of PCE removed during KISCO, and the observed changes in  $K_L$  pre- and post-oxidation. The  $a_i$  was large prior KISCO-1, compared to the other KISCO experiments, which may have lead to the rapid buildup of  $\text{MnO}_2$  at the interface of the DNAPL (Table 11-4). In evaluating the interfacial deposition of  $\text{MnO}_2$  formed during oxidation experiments using  $\text{MnO}_4$  for TCE removal, Urynowicz and Siegrist (51) proposed that during KISCO, the rate of chemical oxidation is relatively rapid and that  $\text{MnO}_2$  deposition occurs when

the reaction takes place in local proximity to the DNAPL interface. Additionally, McKinnon and Thompson (50) asserted that the lack of complete oxidation resulted from precipitation and deposition of reaction by-products at the free phase/aqueous phase interface that increased the mass transfer resistance. The higher  $a_i$  (Table 11-4) prior to KISCO-1 may have caused significant deposition of  $MnO_2$  at the surface of the DNAPL. The larger  $a_i$  prior to KISCO-1 may have allowed for increased deposition of  $MnO_2$  at the surface of the DNAPL, limiting contact between the oxidant and the DNAPL, which rapidly reduced the mass removal rates (Figure 11-3). Results from the vertical single fracture experiment by Tunnicliffe and Thompson (33) and the porous media study by Heiderscheidt et al. (42) found that  $MnO_2$  caused flow bypassing of DNAPL sources. The mass of PCE removed using KISCO -1 was not substantial. As discussed in Chapter 5, the increase in  $a_i$  would be associated with increased  $K_L$ ; however, it appears that in the case of KISCO, this relationship may not be beneficial to PCE removal. The increased  $K_L$  associated with the  $a_i$  in dissolution experiments appears to generate reaction byproducts more rapidly during KISCO, in the fracture network setting. Three likely scenarios to describe this interaction are 1) the large  $a_i$  generated sufficient  $MnO_2$  which accumulated on the surface of the DNAPL down-gradient and diverted the flow; 2) as  $a_i$  increased production and accumulation of reaction byproducts were deposited directly on the surface of the DNAPL, which limited PCE removal; and/or 3) a large volume of DNAPL was accessible to the flow, prior to KISCO application, which rapidly accumulated  $MnO_2$  at the surface and diverted flow around the large volume of DNAPL. In each of the possible scenarios, the common concept is that the large pre-KISCO  $a_i$  increased the formation of reaction byproducts and resulted in flow bypassing (shifting of the pre-KISCO flow paths).

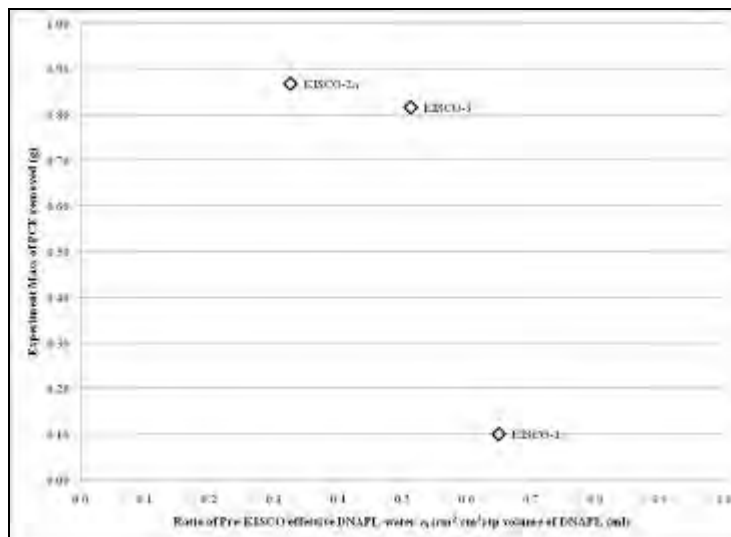


**Figure 11-3.** Relationship between experimental mass of PCE removed during KISCO to the pre-KISCO  $a_i$  normalized to the volume of DNAPL present. KISCO-2b is not shown because the  $a_i$  was immeasurable prior to the KISCO application.

The smaller  $a_i$  observed prior to KISCO-2a application may have limited the rate of reaction byproduct formation. This scenario would have allowed the oxidation reaction to proceed for a longer period of time increasing the mass of PCE removed. The trapped DNAPL for KISCO-2a, may have been located in more remote areas of the fracture network during KISCO-2a (compared specifically to KISCO-1), which limited the interfacial deposition of reaction byproducts and allowed more time for KISCO to oxidize dissolving DNAPL in the network. The increased PCE removal from KISCO-2a increased the formation of reaction byproducts and the altered the existing preferential flow paths. The pre-KISCO-2b  $a_i$  was not measureable, as a result of the reaction byproducts remaining in the network from KISCO-2a, so this KISCO application cannot be included in the analysis. Finally, as presented in Figure 11-3, these observations relating  $a_i$  to PCE mass removal may be further supported by the slightly larger  $a_i$  observed prior to KISCO-3 and the slightly smaller PCE mass removed (816 mg in KISCO-3 versus 868 mg from KISCO-1). The observed trend in Figure 11-3 is interesting since the KISCO-3 application was conducted at a lower experimental velocity and lower concentration than KISCO-1 or -2a, suggesting that in the fracture network the pre-KISCO  $a_i$  may impact the efficiency of the reaction to a greater extent than the experimental velocity or the  $\text{MnO}_4^-$  concentrations. Though a trend between pre-KISCO  $a_i$  and mass of PCE removed is observable, the relationship requires further investigation before a correlation between the parameters can be considered conclusive. The changes in aperture size observed following KISCO applications, as a result of reaction byproduct formation, particularly  $\text{MnO}_2$ , are discussed further in the following Section.

## 11.6 Experimental Mass Balances

The mass of  $\text{MnO}_2$  generated for each KISCO experiment was based on measured effluent concentrations of  $\text{MnO}_2$  and oxidant consumption (discussed below). As presented in Table 11-5 the mass of  $\text{MnO}_2$  measured was: 6.4 g (73.0 mmol) for KISCO-2a; 0.6 g (6.9 mmol) for KISCO-2b (measured at effluent during KISCO application) and 1.1 grams (12.6 mmol) for KISCO-3. Based on a comparison of the measured mass of  $\text{MnO}_2$  and the expected presented in Table 11-4, significant  $\text{MnO}_2$  remained in the fracture network during KISCO applications. Therefore, the mass of  $\text{MnO}_2$  eluted was less than the stoichiometric equivalent. The  $\text{MnO}_2$  that remained in the network and was not eluted was expected to reduce aperture size and alter fracture network flow paths.

The flow field is also impacted by  $\text{CO}_2$  as a reaction byproduct. The volume of  $\text{CO}_2$  produced was assumed to remain stoichiometrically balanced with the PCE DNAPL mass removed, because  $\text{CO}_2$  was produced as a result of the PCE DNAPL- $\text{MnO}_4^-$  reaction. The volume of  $\text{CO}_2$  produced is presented in Table 11-3 and was: 29 ml for KISCO-1; 250 ml for KISCO-2a; 27 ml for KISCO-2b; and 235 ml for KISCO-3. Tunnicliffe and Thompson (33) found that during KISCO applications  $\text{CO}_2$  was built up beneath the colloidal  $\text{MnO}_2$  rind and intermittently released through the colloidal  $\text{MnO}_2$  rind. Even if  $\text{CO}_2$  was released during KISCO,  $\text{MnO}_2$  would continue to be accumulate or be deposited as KISCO was consumed (33), which would maintain the low effluent  $\text{PCE}_{\text{aq}}$  concentrations observed in the fracture network experiments.

The post-KISCO-1 aperture was calculated from tracer tests prior to the conclusion of the test and flushing of the network with solutions to remove  $\text{MnO}_2$  buildup and/or remaining  $\text{CO}_2$ . Li and Schwartz (122) determined  $\text{CO}_2$  bubbles in the subsurface can dissolve into the aqueous phase but the rapid accumulation of  $\text{CO}_2$  early in the flushing and flow bypassing also reduced the possibility for water to contact and dissolve the bubbles. Based on the timing of interfacial area tracer tests following the KISCO applications (Figures 11-1, a-c), the aqueous solubility of  $\text{CO}_2$  (1.5 g/L), the volume of  $\text{CO}_2$  produced and the experimental velocities (Table 11-4), the  $\text{CO}_2$  was expected to have been flushed from the network prior to tracer testing. Given the persistence of  $\text{MnO}_2$  in the fracture network, this KISCO reaction byproduct is believed to be the primary driver of changes observed in aperture following KISCO. The consistency in observed aperture for KISCO-1 (Table 11-2) between pre-KISCO and post-KISCO applications indicates that the deposition of reaction byproducts associated with the large pre-KISCO-1  $a_i$  was sufficient to reduce PCE mass removal but was not significant enough to alter the aperture size or that the pre-KISCO flow paths were shifted to new regions of similar aperture size. Alternatively, the decreased  $a_i$  prior to KISCO-2a application may have reduced the initial rate of reaction byproduct formation at the DNAPL interface. This scenario would have allowed the oxidation reaction to proceed for a longer period of time increasing the mass of PCE removed and the reaction byproducts generated (Table 11-4). The trapped DNAPL may also have been located in more remote areas of the fracture network during KISCO-2a (compared specifically to KISCO-1), which limited the rapid initial production of reaction byproducts, allowed more time for KISCO to oxidize dissolving DNAPL in the network and increased the total  $\text{MnO}_2$  and  $\text{CO}_2$  generated. The increased formation of reaction byproducts in the fracture network resulted in the 50% decrease in average aperture following KISCO-2a. The reaction byproducts that remained in the fracture network following KISCO-2a likely limited contact of the oxidant with the remaining DNAPL and inhibited significant PCE mass removal during KISCO-2b. Following KISCO-2b, the aperture was reduced by 33% or 0.01 cm, as a result of additional  $\text{MnO}_2$  and  $\text{CO}_2$  generated. KISCO-3 had a slightly larger pre-KISCO  $a_i$  than KISCO-2a and following the KISCO-3 application, the aperture was also observed to decrease by half (from 0.06 to 0.03 cm), as in KISCO-2a. These findings indicate the hypothesis that the formation of reaction byproducts using KISCO for PCE DNAPL removal in fractured-rock networks decreases the KISCO treatment efficiency and reduces mass removal effectiveness of PCE.

In a porous media experiment by Heiderscheidt et al. (42) that examined changes in permeability resulting from KISCO, a concentration of 0.1 g  $\text{MnO}_2$ /kilogram unconsolidated media was needed to alter flow paths in unconsolidated media and these areas were observed in and around DNAPL source zones. While this value does not directly translate to fractured media, the concentration of  $\text{MnO}_2$  needed to alter flow paths in unconsolidated media was determined to be significantly below the concentration of  $\text{MnO}_2$  required to fill the pore space and was attributed to  $\text{MnO}_2$  deposition at the pore throats rather than the pore body (123). This porous media finding regarding  $\text{MnO}_2$  is significant since the primary area where mass transfer occurs in a fracture is the intersection of the small aperture regions with the large aperture regions (discussed in Section 5). The primary mass transfer areas at the intersection of the small and larger apertures along the primary flow paths of the fracture network setting could mimic the



pore throats in porous media and concentrate  $\text{MnO}_2$  deposition, which would rapidly alter the flow field (65, 124). Additionally, the mass of  $\text{MnO}_2$  eluted indicates a significant amount of  $\text{MnO}_2$  remained in the system as a result of  $\text{MnO}_4^-$  consumption, which would have the ability significantly alter flow paths.

The mass of oxidant consumed exceeded the mass that would be expected based on the PCE removed (determined from chloride generation). Excess oxidant consumption was also observed in the single fracture KISCO experiment (Section 8). The discrepancy between the expected  $\text{MnO}_4^-$  mass consumed and the measured mass consumed is attributed to the acidic pH condition (average 2.7) that occurs during ISCO (see hydrogen ion generation in equation 6-1). Under acidic conditions where pH drops below 3.5, permanganate can react with the  $\text{MnO}_2$ , forming  $\text{Mn}^{2+}$  which can further react to consume permanganate (108, 125). Based on the measured consumption of  $\text{MnO}_4^-$  during the KISCO applications and the reaction stoichiometry (Equation 8-2), the mass of PCE DNAPL theoretically expected to oxidize ranged was up to 31 times the measured amount of PCE DNAPL oxidized for the KISCO experiments.

The PCE DNAPL recovery at the end of the KISCO experiments ranged from approximately 40 to 62%. These values represent the volume of PCE recovered divided by the volume of PCE DNAPL emplaced. The volume of PCE recovered was equal to the volume of DNAPL collected when the network was drained plus, the PCE dissolved in the flushing solutions (minus the PCE removed during dissolution and KISCO experiments). These percentages of DNAPL mass recovered are low compared to those obtained in the DNAPL dissolution studies (Chapter 5). The lower mass recoveries may result from the dissolution of reaction by products with a 5% acetic acid and hydrogen peroxide solution that is assumed to have also oxidized PCE DNAPL. Following removal of oxidation reaction byproducts, the remaining DNAPL was dissolved using an ethanol flush. The ethanol was flushed through all open ports and through the primary flow paths and captured in an uncapped glass filtering flask. Between ethanol flushing, ethanol remained in the fracture network to ensure the solvent was dispersed throughout the network and had time to dissolve the remaining DNAPL. Presumably, PCE was volatilized from the open filtering flask over the course of the network flushing, which resulted in the poor mass recoveries. Flushed ethanol and, once AGW flow was returned, aqueous effluent samples were collected during flushing of the experiment and analyzed for dissolved phase PCE concentrations on the GC-FID to quantify DNAPL mass recoveries from the experimental fracture network.

### 11.7 Fracture Network Chemical Oxidation Conclusions

The objectives of chemical oxidation study in the fracture network were to 1) evaluate PCE mass removal during KISCO relative to mass removal achieved during pre-KISCO steady state DNAPL dissolution experiments; and 2) evaluate the impact of KISCO on DNAPL dissolution. The formation of reaction byproducts ( $\text{MnO}_2$  and  $\text{CO}_2$ ) cut off contact of the oxidant with the DNAPL and altered the preferential flow paths during KISCO. Alteration of the flow field during KISCO limited the DNAPL-oxidant contact and reduces mass transfer rates. The presence of fracture intersections in the fracture network may lead to increased mixing and the generation of additional reaction byproducts, which further limited mass transfer in the fracture network



during the KISCO applications, after an initial period of effective mass removal. When comparing total PCE mass removed with KISCO, the large pre-KISCO  $a_i$  appears to increase the formation of reaction byproducts and lead to flow bypassing but this conclusion requires further evaluation. Experimentally, the relationship between  $a_i$  and PCE DNAPL removal with KISCO in a fracture network could be evaluated by looking at the efficiency of the KISCO at different  $a_i$  for the same DNAPL saturation, linear velocity and  $\text{MnO}_4^-$  concentration. Additionally, examining the permeability changes in the flow field under the different  $a_i$  conditions would be insightful. Even though  $a_i$  was observed to decrease following KISCO, trapping of PCE DNAPL in the larger aperture regions of the fracture network, adjacent to the effluent, enabled post-KISCO  $\text{PCE}_{\text{aq}}$  concentrations to rapidly rebound.

Based on the limited PCE DNAPL mass removal in fracture network experiments, additional research regarding the application of  $\text{MnO}_2$  mitigation measures with KISCO in fracture networks, may also improve observed KISCO efficiency. Additional research regarding into the effectiveness of KISCO on PCE DNAPL mass removal in a fracture network setting at intensely varied velocities may be also insightful in evaluating KISCO at a specific oxidant concentration. Given the variation in conditions surrounding DNAPL in fractured bedrock setting (DNAPL saturation, trapping, interfacial area combined with variability of the fracture network), it appears the overall effectiveness of KISCO for DNAPL depletion in a fractured bedrocks setting is uncertain at best. Further investigation of the effectiveness of stopping the KISCO application when improved mass removal is no longer observed (i.e. chloride concentrations return to background conditions) may be insightful when comparing KISCO to pump-and-treat scenarios. This investigation would be insightful since steady state dissolution conditions were readily established, and in one instance, improved following KISCO.

## 12. OVERALL CONCLUSIONS AND FINDINGS

The overall goal of the project was to measure and evaluate the architecture, dissolution rate, and impact on groundwater quality of residually trapped PCE DNAPL from both discrete bedrock fractures and fracture networks. We investigated DNAPL dissolution during groundwater flow, as well as the dissolution during both bioaugmentation and chemical oxidation. Our approach utilized single fracture plane experiments, as well as 3-dimensional fracture networks consisting of features such as fracture intersections and dead-end fractures.

This project included four primary tasks:

Task 1: Construction and characterization of single fracture plane and 3-dimensional fracture network systems;

Task 2: Assessment of DNAPL architecture and dissolution in the single plane fracture systems. Subtasks included assessment of DNAPL dissolution during bioaugmentation and chemical oxidation (permanganate and persulfate);

Task 3: Assessment of DNAPL architecture and dissolution in the 3-dimensional fracture network systems. Subtasks included assessment of DNAPL dissolution during bioaugmentation and chemical oxidation (permanganate);

Task 4: Development of models to describe DNAPL dissolution into bypassing water, as wells DNAPL dissolution during bioaugmentation and chemical oxidation.

A brief overview of the project conclusions are provided in this paragraph, followed by the bulleted conclusions required by the reporting format. Our research during this project revealed that DNAPL dissolution, even at the single fracture scale, is strongly controlled by mass transfer. Mass transfer limitations in the examined bedrock fracture systems are more severe than in analogous unconsolidated porous media. For single fracture systems, DNAPL dissolution was related to the effective DNAPL-water interfacial area, and was well described using a mass transfer coefficient that was normalized to the DNAPL-water interfacial area and was a function of the Reynolds number. For fracture networks, the DNAPL dissolution behavior was more complex, likely due to the influence of fracture intersections and preferential flow paths. Bioaugmentation, at both fracture scales, was shown to be effective for enhancing the rate of DNAPL dissolution, despite dissolved PCE concentrations at or near solubility. A model was developed and validated that described the DNAPL dissolution and dechlorination kinetics; the effects of chlorinated ethene and ethene back-partitioning into the DNAPL and shear-induced detachment of DHC biomass were incorporated within the model. Finally, chemical oxidation was shown to be generally ineffective for both removal of DNAPL mass and improving groundwater quality (with respect to dissolved PCE concentrations). While initial DNAPL mass removal rates were high immediately following delivery of the oxidant (either permanganate or

persulfate), mass transfer inhibitions caused a relatively rapid decreases in PCE oxidation and DNAPL mass removal. Interfacial tracer testing confirmed that this decrease in DNAPL removal rate was due to a decrease in contact between DNAPL sources and mobile water, likely due to accumulation of manganese or iron oxides, or possibly CO<sub>2</sub> gas, at the DNAPL water interface. Several peer review papers have been recently published or are in the review/preparation phases (Appendix B).

Bulleted conclusions from each Task are provided below.

#### **DNAPL Architecture in Single Fracture Plane Conclusions**

- Pore structure within the fracture plane, particularly the aperture ratio, controlled the extent of residual DNAPL present.
- Due to preferential (channeled) flow through high permeability pathways, DNAPL entered only a portion (<60%) of the effective fracture volume. Thus, within a single fracture plane, DNAPL likely resides within only a fraction of the fracture volume.
- It was demonstrated that residual DNAPL in the single plane systems primarily resides within the primary water flowpaths
- Effective DNAPL-water interfacial area was significantly less than in analogous unconsolidated systems.
- DNAPL-water interfacial area was not correlated to DNAPL saturation (mL DNAPL/mL fracture volume), fracture aperture, or aperture ratio. This suggests that the effective DNAPL-water interfacial area is controlled by a complex interaction of flow path, DNAPL distribution, and aperture structure, and is not readily predicted. Interfacial and/or partitioning tracer measurements will likely be required to determine this parameter.

#### **DNAPL Architecture in 3-Dimensional Fracture Network Conclusions**

- Residual DNAPL saturations were in the range typically observed for both unconsolidated media and for those measured in the single fracture systems.
- The effective DNAPL-water interfacial area, when considering a DNAPL injection scheme similar to that for the single fracture systems, is significantly greater than for the single fracture systems. This is likely due to the enhanced contact associated with fracture intersections.
- It was demonstrated that a sizeable fraction of the residual DNAPL mass was in the fracture networks was not along the water flow path, indicating that much of the DNAPL was not well contacted by water (i.e., dead-end fractures).
- No correlation was discernable among DNAPL-water interfacial area, DNAPL saturation, and fracture aperture structure.

#### **DNAPL Dissolution in Single Fracture Plane Conclusions**

- DNAPL dissolution was controlled by mass transfer between the mobile water and residual DNAPL
- Preferential flow paths existed even at the single fracture scale

- DNAPL dissolution was controlled by the effective DNAPL-water interfacial area.
- Effective DNAPL-water interfacial area was significantly less than in analogous unconsolidated systems. Accordingly, the DNAPL dissolution rates in the single fracture systems were less than in analogous unconsolidated media systems. These results indicate that DNAPL removal in bedrock fractures is considerably more difficult, due to mass transfer limitations, than in unconsolidated porous media.
- A DNAPL-water interfacial normalized mass transfer coefficient was found to be a well-described function of the Reynolds number, with results for all four fracture plane systems falling along a similar curve.

### **DNAPL Dissolution in Fracture Network Conclusions**

- Intrinsic mass transfer coefficients, for DNAPL loading that was through the influent (analogous to the single fracture experiments) were substantially less in the fracture networks than in the single fracture experiments. This indicates that DNAPL dissolution in fracture networks is more impacted by bulk mass transfer limitations than in single fracture systems and unconsolidated media.
- On the bulk or aggregate scale, mass transfer is not correlated to the effective DNAPL-water interfacial area.
- Overall findings from the DNAPL dissolution studies in the fracture networks indicate that DNAPL dissolution in the fracture networks is governed by preferential flow paths. In these flow paths, PCE becomes saturated (or near-saturated), while PCE concentrations remain low in other flow paths. Thus, small to moderate changes in interfacial area or flow rate will not have a substantial impact on effluent dissolved concentrations, which is consistent with the experimental data.
- These data further suggest that reactions that will consume dissolve PCE in the aqueous phase will likely have a substantial impact on overall DNAPL dissolution – more so than in the single fracture experiments.

### **Bioaugmentation for Enhancement of DNAPL Dissolution in Single Fracture Plane Conclusions**

- In preliminary batch experts with PCE DNAPL present and dissolved PCE concentrations at saturation, no dechlorination was observed after bioaugmenting. Thus, batch microcosms may not be a good test of bioaugmentation effectiveness when DNAPL is present.
- Bioaugmentation was effective for facilitating the microbially-enhanced (DHC) dechlorination of PCE DNAPL in the fractures. We hypothesized dechlorination was observed in the fractures but not the batch system due to the presence of biofilms in the fracture (which typically are more resistant to toxic inhibitions) and/or localized areas of lower dissolved PCE concentrations within the heterogeneous fracture.
- Bioaugmentation was shown to enhance DNAPL dissolution by up to 5-fold. This dissolution enhancement, normalizing for scale, would likely be several times greater in the field.
- Due to back-partitioning into the DNAPL, chlorinated ethene and ethene are poor indicators of the PCE dechlorination rate. Chloride serves as a much better indicator.
- Although some VC and ethene were generated, DCE was shown to be the primary daughter

product, as elevated PCE and/or DCE levels are likely inhibitory to the rate of DCE dechlorination.

- DHC growth was demonstrated, as evidenced by increasing DHC levels in the fracture effluent of the high flow rate experiments, and by the increasing dechlorination rates with time in other experiments.
- Dependence of effluent DHC levels upon the flow velocity was demonstrated, consistent with a microbial biomass shearing mechanism. Thus, distribution of DHC downgradient of the DNAPL source area will likely be dependent upon flow velocity.
- DHC growth was well predicted using our previously developed Monod kinetic model, which was based upon batch kinetic data.
- DHC facilitated dechlorination was primarily due to immobile DHC (presumably associated with biomass) rather than mobile DHC.
- It was demonstrated that residual biomass can serve as an electron donor after active addition of electron donor is terminated.

#### **Bioaugmentation and DNAPL Dissolution Numerical Model Conclusions**

- Based on Monod kinetic parameters determined from batch experiments, DNAPL dechlorination rates and DHC growth were well predicted by the model.
- Back-partitioning accounted for the discrepancies between theoretical and measured chloride concentrations.
- DHC migration and detachment was shown to be a function of the velocity, which is consistent with a shear mechanism for DHC detachment from biofilms.
- The developed DNAPL bioaugmentation model can be used to estimate DNAPL dissolution rates in bedrock fractures.

#### **Bioaugmentation for Enhancement of DNAPL Dissolution in 3-Dimension Fracture Networks Conclusions**

- Bioaugmentation was demonstrated to be effective for the dechlorination of PCE DNAPL, with demonstrated dissolution enhancement factors greater than 3.
- Back-partitioning of the chlorinated ethenes and ethene into the DNAPL made these compounds a poor indicator for the extent and rate of DNAPL dechlorination that was occurring.
- The extent of back-partitioning was substantially greater in the fracture network than the single fracture systems, indicating that mass transfer at the locations of biological reaction was enhanced in the fracture network relative to the single fracture systems. This was likely due to the enhanced mixing at fracture intersections.
- The rate of dechlorination was substantially greater in the fracture network compared to the single fracture systems. Again, this was likely due to the enhanced mixing at fracture intersections.

### **Chemical Oxidation for Enhancement of DNAPL Dissolution in Single Fracture Plane Conclusions**

- Both permanganate and persulfate resulted in an initially high rate of DNAPL removal, followed by a decline in DNAPL mass removal.
- Neither permanganate nor persulfate were effective for removing a significant fraction of the DNAPL mass, or improving groundwater effluent quality (with respect to dissolved PCE concentrations).
- Application of permanganate resulted in clogging of the fracture, likely due to  $\text{MnO}_2$  formation.
- It was demonstrated that the effective DNAPL-water interfacial area decreased after persulfate addition; this decrease likely was due to accumulation of iron oxides and/or carbon dioxide at the DNAPL-water interface.
- Rebound in dissolved PCE concentrations occurred after persulfate treatment ended.
- DNAPL mass removal rates during bioaugmentation, after several weeks, exceeded mass removal rates during chemical oxidation. Thus, bioaugmentation is likely a more effective long term treatment approach than permanganate or persulfate for treating DNAPL in fractured bedrock.

### **Chemical Oxidation for Enhancement of DNAPL Dissolution in 3-Dimensional Fracture Networks Conclusions**

- Application of permanganate for treatment of DNAPL in fractures results in an initially high mass removal rate, followed by a rapid decline in mass removal.
- Application of permanganate did not result in any measurable loss of fracture volume or clogging. This differed from observations at the single fracture scale, and was likely the result of redirected flow paths in the much larger fracture network system.
- It was shown that application of permanganate resulted in a decrease in the effective DNAPL-water interfacial area, which likely is the cause for the observed reduction in mass transfer that occurred following the initial spike in PCE mass removal.  $\text{MnO}_2$  solids and/or  $\text{CO}_2$  were the likely causes for the reduction in DNAPL-water contact.
- Permanganate will likely be ineffective for treating residual DNAPL sources in fracture networks.



### 13. IMPLICATIONS FOR FUTURE RESEARCH

The results from this study, overall, highlight the importance of mass transfer and flow heterogeneity for DNAPL dissolution processes in fractured rock systems, the ineffectiveness of chemical oxidants for treating DNAPL sources in fractures, and the potential effectiveness of bioaugmentation/bioremediation as an effective treatment approach for addressing DNAPL sources in fractured bedrock. We envision three primary areas of future research that emanate from the work performed within this project:

- ***Assessment of DNAPL dissolution and treatment processes at the field scale.*** The insights into the DNAPL dissolution and treatment processes obtained during this study are expected to provide relevant understanding with respect to field scale processes. However, the surrogate bench scale systems evaluated in this project certainly are not expected to provide a complete representation of DNAPL dissolution processes that can occur at the field scale. Similar studies performed at the field scale, perhaps using tools such as partitioning and interfacial tracer tests, passive flux meters, borehole logging techniques, and discrete interval samplers, are needed to provide a more comprehensive understanding of these processes, incorporating an appropriate scale of heterogeneity, in fractured bedrock aquifers.
- ***Investigation of the impacts of water velocity and shear and DHC mobility.*** Our bioaugmentation study showed that detachment of DHC, and ultimately the extent to which DHC could migrate downgradient of the source area, was dependent upon the water velocity. This finding has important implications for the design and assessment of bioaugmentation and biostimulation at the field scale. Being able to better predict, or even design, the extent to which DHC can be distributed in an aquifer (bedrock or overburden) would be an important tool. We believe that additional bench scale and field scale studies are needed to better understand this relationship.
- ***Development of methods to limit precipitate formation at the DNAPL-water interface during application of chemical oxidants.*** Formation of reaction products at the DNAPL-water interface limited the effectiveness of permanganate and persulfate with respect to treatment of DNAPL sources in bedrock fractures. Development of technologies to limit this reaction product accumulation has the potential to greatly improve the effectiveness of chemical oxidants for treatment in DNAPL source areas.

## 14. REFERENCES

- (1) Held, R.J., Celia, M.A. Modeling support of functional relationships between capillary pressure, saturation, interfacial area and common lines. *Adv. Water Resour.* **2001**, 24, 325-343.
- (2) Dillard, L.A., Essaid, H.I., Blunt, M.J. A functional relation for field-scale nonaqueous liquid dissolution developed using a pore network model. *J. Contam. Hydrol.* **2001**, 48, 89-119.
- (3) Dalla, E., Hilpert, M., Miller, C.T. Computation of the interfacial area for two-fluid porous medium systems. *J. Contam. Hydrol.* **2002**, 56, 25-48.
- (4) Clement, T.P., Gautam, T.R., Lee, K.K., Truex, M.J., Davis, G.B. Modeling coupled NAPL-dissolution and rate-limited sorption reactions in biologically active porous Media. *Bioremediation Journal.* **2004**, 8, 47-64.
- (5) Powers, S.E., Abriola, L.M., Weber, W.J. An experimental investigation of nonaqueous phase liquid dissolution in saturated subsurface systems: Transient mass transfer rates. *Water Resources Res.*, **1994**, 30, 321-332.
- (6) Schaefer, C.E., DiCarlo, D.A., Blunt, M.J. Determination of water-oil interfacial area during 3-phase gravity drainage in porous media. *J. Coll. Interface Sci.*, **2000**, 221, 308-312.
- (7) Sahloul, N.A., Ioannidis, M.A., and Chatzis, I. Dissolution of residual non-aqueous phase liquids in porous media: Pore scale mechanisms and mass transfer rates. *Adv. Water Resourc.* **2002**, 25, 33-49.
- (8) Jeong, S.W., Wood, A.L., Lee, T.R. Enhanced removal of DNAPL trapped in porous media using simultaneous injection of cosolvent with air: Influencing factors and removal mechanisms. *J. Hazard. Mater.* **2003**, 101, 109-122.
- (9) Cho, J, Annable, M.D., Rao, P.S.C. Measured mass transfer coefficients in porous media using specific interfacial area. *Environ. Sci. Technol.* **2005**, 39, 7883-7888.
- (10) Dickson, S.E., Thomson, N.R. Dissolution of entrapped DNAPLs in variable aperture fractures: Experimental data and empirical model. *Environ. Sci. Technol.* **2003**, 37, 4128-4137.
- (11) Detwiler, R.L., Glass, R.J., Rajaram, H. An investigation of the parameters controlling interphase mass transfer in variable aperture fractures. *Eos. Trans. AGU*, **83**(47):F496, Fall Meet. Suppl., Abstract H62G-08, 2002. *American Geophysical Union Fall meeting*, Dec.6–10, **2002**, San Francisco UCRL-JC-149856-ABS.



- (12) Rubin, H., K. Rathfelder, K., Abriola, L.M., Spiller, M., Köngeter, J. Using continuum approach to quantify the remediation of nonaqueous phase liquid contaminated fractured permeable formations. *J. Environ. Engin.* **2004**, 130, 1345-1356.
- (13) Maymó-Gatell, X.; Chien, Y.; Gossett, J.M.; Zinder, S.H. Isolation of a bacterium that reductively dechlorinates tetrachloroethene to ethene. *Science* **1997**, 276, 1568-1571.
- (14) Harkness, M.R.; Bracco, A.A.; Brennan Jr., M.J.; De Weerd, K.A.; Spivack, J.L. Use of bioaugmentation to stimulate complete reductive dechlorination of trichloroethene in Dover soil columns. *Environ. Sci. Technol.* **1999**, 33, 1100-1109.
- (15) Major, D.W.; McMaster, M.L.; Cox, E.E.; Edwards, E.A.; Dworatzek, S.M.; Hendrickson, E.R.; Starr, M.G.; Payne, J.A.; Buonamici, L.W. Field demonstration of a successful bioaugmentation to achieve dechlorination of tetrachloroethene to ethene. *Environ. Sci. Technol.* **2002**, 36, 5106-5116.
- (16) Lendvay, J.M.; Löffler, F.E.; Dollhopf, M.; Aiello, M.R.; Daniels, G.; Fathepure, B.Z.; Gebhard, M.; Heine, R.; Helton, R.; Shi, J.; Krajmalnik-Brown, R.; Major, Jr., C.L.; Barcelona, M.J.; Petrovskis, E.; Hickey, R.; Tiedje, J.M.; Adriaens, P. Bioreactive barriers: a comparison of bioaugmentation and biostimulation for chlorinated solvent remediation. *Environ. Sci. Technol.* **2003**, 37, 1422-1431.
- (17) Schaefer, C.E.; Condee, C.W.; Vainberg, S.; Steffan, R.J. Bioaugmentation for chlorinated ethenes using *Dehalococcoides* sp.: comparison between batch and column experiments. *Chemosphere* **2009**, 75, 141-148.
- (18) United States Environmental Protection Agency. Demonstration of bioaugmentation of DNAPL through biostimulation and bioaugmentation at Launch Complex 34 Cape Canaveral Air Force station, Florida. **2004**, EPA/540/R-07/007.
- (19) Interstate Technology & Regulatory Council. Overview of in situ bioremediation of chlorinated ethene DNAPL source zones. **2005**, BioDNAPL-1. Washington, D.C.
- (20) Interstate Technology & Regulatory Council. 2007. In situ bioremediation of chlorinated ethene DNAPL source zones: case studies. **2007**, BioDNAPL-2. Washington, D.C.
- (21) Yang, Y.; McCarty, P.L. Biologically enhanced dissolution of tetrachloroethene DNAPL. *Environ. Sci. Technol.* **2005**, 34, 2979-2984.
- (22) Adamson, D.T.; McDade, J.M.; Hughes, J.B. Inoculation of a DNAPL source zone to initiate reductive dechlorination of PCE. *Environ. Sci. Technol.* **2003**, 37, 2525-2533.

- (23) Amos, B.K.; Suchomel, E.J.; Pennell, K.D.; Löffler, F.E. Microbial activity and distribution during enhanced contaminant dissolution from a NAPL source zone. *Water Res.* **2008**, 42, 2963-2974.
- (24) Huang, D.; Becker, J.G. Dehalorespiration model that incorporates self-inhibition and biomass inactivation effects of high tetrachloroethene concentrations. *Environ. Sci. Technol.* **2011**, 45, 1093-1099,
- (25) Amos, B.K.; Suchomel, E.J.; Pennell, K.D.; Löffler, F.E. Spatial and temporal distributions of *Geobacter lovleyi* and *Dehalococcoides* spp. during bioenhanced PCE-DNAPL dissolution. *Environ. Sci. Technol.* **2009**, 43, 1977-1985.
- (26) Glover, K.C.; Munakata-Marr, J.; Illangasekare, T.H. Biologically enhanced mass transfer of tetrachloroethene from DNAPL in source zones: experimental evaluation and influence of pool morphology. *Environ. Sci. Technol.* **2007**, 41, 1384-1389.
- (27) Christ, J.A.; Abriola, L.M. Modeling metabolic reductive dechlorination in dense non-aqueous phase liquid source zones. *Adv. Water Resour.* **2007**, 30, 1547-1561.
- (28) Becker, J.G.; Seagren, E.A. Modeling the effects of microbial competition and hydrodynamics on the dissolution and detoxification of dense nonaqueous phase liquid contaminants. *Environ. Sci. Technol.* **2009**, 43, 870-877.
- (29) Sleep, B.E.; Seepersad, D.J.; Mo, K.; Heidorn, C.M.; Hrapovic, L.; Morrill, P.L.; McMaster, M.L.; Hood, E.D.; Lebron, C.; Lollar, B.S.; Major, D.W.; Edwards, E.A. Biological enhancement of tetrachloroethene dissolution and associated microbial community changes. *Environ. Sci. Technol.* **2006**, 40, 3623-3633.
- (30) Chu, M.; Kitanidis, P.K.; McCarty, P.L. Effects of biomass accumulation on microbially enhanced dissolution of a PCE pool: a numerical simulation. *J. Contam. Hydrol.* **2003**, 65, 79-100.
- (31) Detwiler, R.L.; Rajaram, H.; Glass, R.J. Interphase mass transfer in variable aperture fractures: controlling parameters and proposed constitutive relationships. *Water Resour. Res.* **2009**, 45, 1-21.
- (32) Schaefer, C.E.; Callaghan, A.V.; King, J.D.; McCray, J.E. Dense nonaqueous phase liquid architecture and dissolution in discretely fractured sandstone blocks. *Environ. Sci. Technol.* **2009**, 43, 1877-1883.
- (33) Tunnicliffe, B.S.; Thomson, N.R. Mass removal of chlorinated ethenes from rough-walled fractures using permanganate. *J. Contam. Hydrol.* **2004**, 75, 91-114.

- (34) Block, P.A.; Brown, R.A.; Robinson, D. Novel activation technologies for sodium persulfate *in situ* chemical oxidation. *Proceedings of the Fourth International Conference on the Remediation of Chlorinated and Recalcitrant Compounds*, Monterey, CA, **2004**.
- (35) Waldemer, R.H.; Tratnyek, P.G.; Johnson, R.L.; Nurmi, J.T. Oxidation of chlorinated ethenes by heat-activated persulfate: kinetics and products. *Environ. Sci. Technol.* **2007**, 41, 1010-1015.
- (36) Liang, C.; Ling, C.-P.; Chen, C.-C. pH dependence of persulfate activation by EDTA/Fe(III) for degradation of trichloroethylene. *J. Contam. Hydrol.* **2009**, 106, 173-182.
- (37) Tsitonaki, A.; Petri, B.; Crimi, M.; Mosbaek, H.; Siegrist, R.L.; Bjerg, P.L. In situ chemical oxidation of contaminated soil and groundwater using persulfate: a review. *Critical Rev. Environ. Sci. Technol.* **2010**, 40, 55-91.
- (38) Liang, C.; Bruell, C.J.; Marley, M.C.; Sperry, K.L. Persulfate oxidation for in situ remediation of TCE. II. Activated by chelated ferrous ion. *Chemosphere* **2004**, 55, 1225-1233.
- (39) Huang, K.C.; Zhao, Z.; Hoag, G.E.; Dahmani, A.; Block, P.A. Degradation of volatile organic compounds with thermally activated persulfate oxidation. *Chemosphere* **2005**, 61, 551-560.
- (40) Huang, K.-C.; Hoag, G.E.; Chheda, P.; Woody, B.A.; Dobbs, G.M. Chemical oxidation of trichloroethylene with potassium permanganate in a porous medium. *Adv. Environ. Res.* **2002**, 7, 217-229.
- (41) Hrapovic, L.; Sleep, B.E.; Major, D.J.; Hood, E.D. Laboratory study of treatment of trichloroethene by chemical oxidation followed by bioremediation. *Environ. Sci. Technol.* **2005**, 39, 2888-2897.
- (42) Heiderscheidt, J.L.; Siegrist, R.L.; Illangasekare, T.H. Intermediate-scale 2D experimental investigation of in situ chemical oxidation using potassium permanganate for remediation of complex DNAPL source zones. *J. Contam. Hydrol.* **2008**, 102, 3-16.
- (43) Schnarr, M.; Truax, C.; Farquhar, G.; Hood, E.; Gonullu, T.; Stickney, B. Laboratory and controlled field experiments using potassium permanganate to remediate trichloroethylene and perchloroethylene DNAPLs in porous media. *J. Contam. Hydrol.* **1998**, 29, 205-224.
- (44) Huang, K.-C.; Chheda, P.; Hoag, G.E.; Woody, B.A.; Dobbs, G.M. Pilot-scale study of in situ chemical oxidation of trichloroethene with sodium permanganate. *Proceedings of the Second International Conference on the Remediation of Chlorinated and Recalcitrant Compounds*, Monterey, CA, **2000**.

- (45) Nelson, M.D.; Parker, B.L.; Al, T.A.; Cherry, J.A.; Loomer, D. Geochemical reactions resulting from in situ oxidation of PCE-DNAPL by  $\text{KMnO}_4$  in a sandy aquifer. *Environ. Sci. Technol.* **2001**, 35, 1266-1275.
- (46) McGuire, T.M.; McDade, J.M.; Newell, C.J. Performance of DNAPL source depletion technologies at 59 chlorinated solvent sites. *Ground Water Monit. Rem.* **2006**, 26, 73-84.
- (47) Thomson, N.R.; Hood, E.D.; Farquhar, G.J. Permanganate treatment of an emplaced DNAPL source. *Ground Water Monit. Rem.* **2007**, 27, 74-85.
- (48) Lee, E.S.; Seol, Y.; Fang, Y.C.; Schwartz, F.W. Destruction efficiencies and dynamics of reaction fronts associated with the permanganate oxidation of trichloroethylene. *Environ. Sci. Technol.* **2003**, 37, 2540-2546.
- (49) Petri, B.G.; Siegrist, R.L.; Crimi, M.L. Effects of groundwater velocity and permanganate concentration on DNAPL mass depletion rates during in situ oxidation. *J. Environ. Engin.* **2008**, 134, 1-13.
- (50) MacKinnon, L.K.; Thomson, N.R. Laboratory-scale in situ chemical oxidation of a perchloroethylene pool using permanganate. *J. Contam. Hydrol.* **2002**, 56, 49-74.
- (51) Urynowicz, Michael A., and Robert L Siegrist. Interphase mass transfer during chemical oxidation of TCE DNAPL in an aqueous system. *J. Contam. Hydrology*, **2005**, 80, 93-106.
- (52) Crimi, M.L., and R.L. Siegrist. Impact of Reaction Conditions on  $\text{MnO}_2$  Genesis During Permanganate Oxidation. *J of Environ Eng.* **2004**, 130, 562-572.
- (53) Park, Y. J., K. K. Lee, G. Kosakowski, and B. Berkowitz. Transport behavior in three-dimensional fracture intersections. *Water Resour. Res.*, **2003**, 39, 1215.
- (54) Mourzenko, V. V., Yousefian, F., Kolbah, B., Thovert, J.-F. and Adler, P. M. Solute transport at fracture intersections. *Water Resour. Res.*, **2002**, 38, 14.
- (55) Berkowitz, B., Naumann, C., and Smith, L. Mass transfer at fracture intersections: An evaluation of mixing models. *Advances in Water Resources.* **1994**, 25, 861-884.
- (56) Bekri S., Thovert, J.F. and Adler, P.M. Dissolution and deposition in fractures. **1997**.
- (57) Becker, M. W. and Shapiro, A. M., Tracer transport in fractured crystalline rock: Evidence of nondiffusive breakthrough tailing. *Water Resources Research* **2000**, 36, 1677-1686.
- (58) McKay L.D., Sanford, W. E., and Strong, J. M., Field-Scale Migration of Colloidal Tracers in a Fractured Shale Saptolite. *Groundwater*, **2000**, 38, 139-147.



- (59) Johnson J., Brown, S., and Stockman, H., Fluid flow and mixing in rough-walled fracture intersections. *Journal of Geophysical Research*, **2006**, 111.
- (60) Kosakowski, G., Berkowitz, B., Scher, H., Analysis of field observations of tracer transport in a fractured till. *Journal of Contaminant Hydrology*, **2001**, 47, 29-51.
- (61) Keller, A., High resolution CAT imaging of fractures in consolidated material, *International. Journal of Rock Mechanics and Mineral Science*, **1997**, 34, 358–375.
- (62) Wood, T.R.; Glass, R.J.; McJunkin, T.R.; R.K. Podgorney, R.A.; Laviolette, K.S.; Noah, D.L.; Stoner, R.C.; Starr; and Baker, K. Unsaturated Flow through a Small Fracture-Matrix Network: Part 1. Experimental Observations. *Vadose Zone J.* **2004**, 3, 90-100.
- (63) Pankow, B. L., Cherry, J. A., Chapman, S. W., Guilbeault, M. A. Review and Analysis of Chlorinated Solvent Dense Nonaqueous Phase Liquid Distributions in Five Sandy Aquifers, *Vadose Zone Journal*, **2003**, 2:116-137.
- (64) Reynolds, D. A. and Kueper, B. H. Numerical Examination of Factors Controlling DNAPL Migration Through a Single Fracture. *Ground Water*, **2002**, 40, 368-377.
- (65) Kueper, B.; McWhorter, D.B. The Behavior of Dense, Nonaqueous Phase Liquids in Fractured Clay and Rock. *Groundwater*, **1991**, 29, 716-728.
- (66) Schuille and Pankow J. F., Schuille, F., Dense Chlorinated Solvents in Porous and Fractured Media: Model Experiments. **1988**. Boca Raton, Florida, Lewis Publishers.
- (67) National Research Council. Rock Fractures and Fluid Flow: Contemporary Understanding and Applications, **1996**. National Academy Press, Washington, DC.
- (68) Cussler, E. L., Diffusion: Mass Transfer in Fluid Systems. **2005**. Cambridge, UK, Cambridge University Press.
- (69) Kueper, B. H., Wealhall, G. P., Smith J.W, Leharne S.A., Lerner D.N., An Illustrated Handbook of DNAPL Transport and Fate in the Subsurface, **2004**. Environment Agency, United Kingdom.
- (70) Parker, B. L., R. W. Gillham, Cherry, J.A., Diffusive Disappearance of Immiscible-Phase Organic Liquids in Fractured Geologic Media. *Ground Water*, **1994**, 32, 805-820.
- (71) Kosakowski, G., Anomalous transport of colloids and solutes in a shear zone, *Journal of Contaminant Hydrology*, **2004**, 72 :23– 46.
- (72) Berkowitz, B., Scher, H., Theory of anomalous chemical transport in fracture networks. *Physics Review E* **1998**, 57, 5858 – 5869.

- (73) Reistma, S., B.H. Kueper, “Laboratory Measurement of Capillary-Pressure Saturation Relationships in a Rock Fracture”, *Water Resour. Res.* **1994**, 30, 865-878.
- (74) Boving, T. B., and P. Grathwohl (2001), Tracer diffusion coefficients in sedimentary rocks: correlation to porosity and hydraulic conductivity, *J. Contam. Hydrol.*, 53, 85-100.
- (75) Schaefer, C.E., DiCarlo, D.A., and Blunt, M.J.. Experimental Measurement of Air-Water Interfacial Area during Gravity Drainage and Secondary Imbibition in Porous Media. *Water Resour. Res.* **2000**, 36, 885-890.
- (76) Vainberg, S.; Condee, C.W.; Steffan, R.J. Large-scale production of bacterial consortia for remediation of chlorinated solvent-contaminated groundwater. *J. Indus. Microbiol. Biotechnol.* **2009**, 26, 1189-1197.
- (77) Novakowski, K.; Bickerton, G.; Lapcevic, P.; Voralek, J.; Ross, N. Measurements of groundwater velocity in discrete rock fractures. *J. Contam. Hydrol.* **2006**, 85, 44-60.
- (78) Saripalli, K. P., Kim, H., Suresh, P., Rao, C. and Annable, M.D. Measurement of Specific Fluid–Fluid Interfacial Areas of Immiscible Fluids in Porous Media. *Environ. Sci. Technol.*, **1997**, 31 (3), 932-936.
- (79) Saripalli, K. P.; Rao, P. S. C.; Annable, M. D. Determination of specific NAPL-water interfacial areas of residual NAPLs in porous media using the interfacial tracers technique. *J. Contam. Hydrol.* **1998**, 30, 375–391.
- (80) Annable, M.D. Jawitz, J.W., Rao, P.S.C., Daib, D.P., Kim, H. and Wood, A.L. Field Evaluation of Interfacial and Partitioning Tracers for Characterization of Effective NAPL-Water Contact Areas, *Groundwater* **1998**, 36, 495 -502.
- (81) Cho, J.; Annable, M. D.; Rao, P. S. C. Measured mass transfer coefficients in porous media using specific interfacial area. *Environ. Sci. Technol.* **2005**, 39, 7883–7888.
- (82) Tsang, Y. W. Usage of “Equivalent apertures” for rock fractures as derived from hydraulic and tracer tests. *Water Resour. Res.* **1992**, 28, 1451-1455.
- (83) Schaefer, C.E.; Towne, R.M.; Vainberg, S.; McCray, J.E.; Steffan, R.J. Bioaugmentation for treatment of dense non-aqueous phase liquid in fractured sandstone blocks. *Environ. Sci. Technol.* **2010**, 44, 4958-4964.
- (84) Yu, S., Dolan, M., Semprini, L.. Kinetics and inhibition of reductive dechlorination of chlorinated ethylenes by two different mixed cultures. *Environ. Sci. Technol.* **2005**, 39, 195-205.

- (85) Clement, T., Peyton, B., Skeen, R., Jennings, D., Petersen, J.. Microbial growth and transport in porous media under denitrification conditions: experiments and simulations. *J. Contam. Hydrol.* **1997**, 24, 269-285.
- (86) Ramsburg, C.A., Thornton, C.E., Christ, J.A.. Degradation Product Partitioning in Source Zones Containing Chlorinated Ethene Dense Non-Aqueous-Phase Liquid. *Environ. Sci. Technol.* **2010**, 44, 9105-9111.
- (87) Toride, N., Leij, F.J., van Genuchten, M.Th. The CXTFIT code for estimating transport parameters from laboratory or field tracer experiments. U.S. Salinity Laboratory, Agricultural Research Service, Riverside, CA, **1995**, Research Report No. 137.
- (88) Cady, C.C., Silliman, S.E., Shaffern, E. Variation in aperture estimate ratios from hydraulic and tracer tests in a single fracture. *Water Resour. Res.* **1993**, 29, 2975-2982.
- (89) Damste, J.S.S., Schouten, S., and Keller, A.A. High resolution CAT imaging of fractures in consolidated materials. *Int. J. Rock Mech. Min. Sci.* and Geomechanics Abstracts. **1997**, 34, 358-370.
- (90) Karpyn, Z.T., Grader, A.S., Halleck, P.M. Visualization of fluid occupancy in a rough fracture using micro-tomography. *J. Coll. Interface Sci.*, **2007**, 307, 181-187.
- (91) Detwiler, R.L., Rajaram, H., Glass, R.J. Saturated relative permeability of variable-aperture fractures. *Physical Review E*, **2005**, 71, 1-9.
- (92) Anastasiadis, S.H., Chen, J.-K., Koberstein, J.T., Seigel, A.F., Sohn, J.E., Emerson, J.A. The determination of interfacial tension by video image processing of pendant fluid drops. *J. Coll. Interface Sci.*, **1987**, 119, 55-66.
- (93) Jain, V., Bryant, S., Sharma, M. Influence of wettability and saturation on liquid-liquid interfacial area in porous media. *Environ. Sci. Technol.* **2002**, 37, 584-591.
- (94) Morley, M.C., Yamamoto, H, Speitel Jr., G.E., Clausen, J. Dissolution kinetics of high explosives particles in a saturated sandy soil. *J. Contam. Hydrol.* **2006**, 85:141-158.
- (95) Falta, R.W.; Rao, P.S.; Basu, N. Assessing the impacts of partial mass depletion in DNAPL source zones. I. Analytical modeling of source zone strength functions and plume response. *J. Contam. Hydrol.* **2005**, 78, 259-280.
- (96) Adamson, D.T.; Newell, C.J. Support of source zone bioremediation through endogenous biomass decay and electron donor recycling. *Bioremediation J.* **2009**, 13, 29-40.
- (97) Sleep, B.E.; Brown, A.J.; Lollar, B.S. Long-term tetrachloroethene degradation sustained by endogenous cell decay. *J. Environ. Engin. Sci.* **2005**, 4, 11-17.

- (98) Seagren, E.A.; Rittmann, B.E.; Valocchi, A.J. Quantitative evaluation of the enhancement of NAPL-pool dissolution by flushing and biodegradation. *Environ. Sci. Technol.* **1994**, 28, 833-839.
- (99) Harrison, J.J.; Rabiei, M.; Turner, R.J.; Badry, E.A.; Sproule, K.M.; Ceri, H. Metal resistance in *Candida* biofilms. *FEMS Microbiol. Ecol.* **2006**, 55, 479-491.
- (100) Chen, S.; Sun, D.; Chung, J.S. Anaerobic treatment of highly concentrated aniline wastewater used packed-bed biofilms reactor. *Process Biochem.* **2007**, 42, 1666-1670.
- (101) Zysset, A.; Stauffer, F.; Dracos, T. Modeling of reactive groundwater transport governed by biodegradation. *Water Resour. Res.* **1994**, 30, 2423-2434.
- (102) Yu, S., Semprini, L., 2004. Kinetics and modeling of reductive dechlorination at high PCE and TCE concentrations. *Biotech. Bioengin.* **2004**, 88, 451-464.
- (103) Brusseau, M.L., S. K. Sandrin, L. Li, I. Yolcubal, F. L. Jordan, R. M. Maier. Biodegradation during contaminant transport in porous media: 8. The influence of microbial system variability on transport behavior and parameter determination. *Water Resour. Res.*, 2006, 42.
- (104) Jeong-Hun Park, Xianda Zhao, Voice, T.C. Comparison of Biodegradation Kinetic Parameters for Naphthalene in Batch and Sand Column Systems by *Pseudomonas Putida*. *Environ. Progress* **2001**, 20, 93-102.
- (105) Liang, C.; Lee, I.-L.; Hsu, I.-Y.; Liang, C.-P.; Lin, Y.-L. Persulfate oxidation of trichloroethylene with and without iron activation in porous media. *Chemosphere* **2008**, 70, 426-435.
- (106) Huang, K.C.; Hoag, G.E.; Chheda, P.; Woody, B.A.; Dobbs, G.M. Kinetics and mechanism of oxidation of tetrachloroethylene with permanganate. *Chemosphere* **2002**, 46, 815-825.
- (107) Siegrist, R.L.; Urynowicz, M.A.; West, O.R.; Crimi, M.L.; Lowe, K.S. *Principles and Practices of In Situ Chemical Oxidation Using Permanganate*. Battelle Press, Columbus, OH, 2001.
- (108) Kao, C.M.; Huang, K.D.; Wang, J.Y.; Chen, T.Y.; Chien, H.Y. Application of potassium permanganate as an oxidant for in situ oxidation of trichloroethylene-contaminated groundwater: a laboratory and kinetics study. *J. Haz. Mat.* **2008**, 153, 919-927.
- (109) Buxton, G.V.; Malone, T.N.; Salmon, G.A. Reaction of  $\text{SO}_4^{\cdot -}$  with  $\text{Fe}^{2+}$ ,  $\text{Mn}^{2+}$  and  $\text{Cu}^{2+}$  in aqueous solution. *J. Chem Soc., Faraday Trans.* **1997**, 93, 2893-2897.

- (110) Schwillie, F. Dense Chlorinated Solvents in Porous and Fractured Media, Lewis, Chelsea, Mich., **1988**.
- (111) Schwillie, F., Migration of organic fluids immiscible with water in the unsaturated zone. **1984**. In: Pollutants in Porous Media: The Unsaturated Zone between Soil Surface and Groundwater, Springer, New York, N.Y., pp. 27–48.
- (112) Rubin, H., Rathfelder, K. and Abriola, L. M. Modeling Quasi-Steady NAPL Dissolution in Fractured Permeable Media. *J. of Envi Engn* **1997**, 205-16.
- (113) Moreno, L., Tsang, Y. W., Tsang, C. F., Hale, F. V. and Neretnieks, I. Flow and tracer transport in a single fracture: A stochastic model and its relation to some field observations, *Water Resour. Res.*, **1988**, 24, 2033–2048.
- (114) Geller, J. T., and J. R. Hunt, Mass transfer from nonaqueous phase organic liquids in water-saturated porous media, *Water Resour Res.*, **1993**, 29, 833-845.
- (115) Powers, S. E.; Abriola, L. M.; Weber W. J. An Experimental Investigation of Nonaqueous Phase Liquid Dissolution in Saturated Subsurface Systems: Steady State Mass Transfer Rates, *Water Resour. Res.*, **1992**, 28, 2691–2705.
- (116) Detwiler, R. L.; Rajaram, H.; Glass R. J. Nonaqueous-Phase-Liquid Dissolution in Variable-Aperture Fractures: Development of a Depth-Averaged Computational Model with Comparison to a Physical Experiment, *Water Resour. Res.*, **2001**, 37, 3115–312.
- (117) Detwiler, R. L., Glass, R. J. and Bourcier, W. Experimental observations of fracture dissolution: The role of Peclet number on evolving aperture variability. *Geophysical Res. Letters*, **2003**, 30, 1648-1652.
- (118) Helsel, D.R. and Hirsch, R.M., Statistical Methods in Water Resources, Elsevier: Amsterdam, **1992**.
- (119) Fure, A. D., Jawitz, J. W. and Annable, M. D. DNAPL source depletion: Linking architecture and flux response, *J. Contam. Hydrol.* **2006**, 85, 118-140.
- (120) Bear, J., Tsang, C. F., Marsily, G. Flow and transport in fracture rock, Academic Press Limited: San Diego, **1993**.
- (121) Miller, C. T.; Poirier-McNeill, M. M.; Mayer, A. S. Dissolution of trapped nonaqueous phase liquids: Mass transfer characteristics. *Water Resour. Res.*, **1990**, 26, 2783–2796.



- (122) Li, X.D. and Schwartz, F. W. DNAPL remediation with in situ chemical oxidation using potassium permanganate: Part I. Mineralogy of Mn oxide and its dissolution in organic acids, *Jour of Cont Hydrol.* **2004**, 68, 39-53.
- (123) Siegrist R. L., Crimi, M. L. and Simpkin, T. J., eds., Chemical Oxidation for Groundwater Remediation, Springer: New York, 2011.
- (124) Esposito, S. J. , Thomson, N. R., Two-phase flow and transport in a single fracture-porous medium system, *J. Contam. Hydrol.* , **1999**, 37, 319-341.
- (125) Siegrist R. L., Urynowicz, M. A., Crimi, M. L. and Lowe, K.S. Genesis and Effects of Particles Produced during In Situ Chemical Oxidation Using Permanganate, *J. Environ. Eng.*, **2002**, 128, 1068-1079.



## APPENDIX A: SUPPORTING DATA

### A-1. CALCULATION OF BACK-PARTITIONING COEFFICIENT

Solubility of TCE = 1100 mg/L or **8.37 mM** (Molecular weight = 131 g/mol)

Solubility of cis-DCE = 3500 mg/L or **36 mM** (Molecular weight = 96.95 g/mol)

Solubility of VC = 2763 mg/L or **44.20 mM** (Molecular weight = 62.5 g/mol)

Solubility of Ethene = 131 mg/L or **4.67 mM** (Molecular weight = 28.05 g/mol)

Regressed value of DCE back-partitioning coefficient for Experiment-A =  $0.04 \text{ hr}^{-1}$

$$\xi_{TCE} = \frac{36}{8.37} * 0.04 = 0.17 \text{ hr}^{-1}$$

$$\xi_{VC} = \frac{36}{44} * 0.04 = 0.03 \text{ hr}^{-1}$$

$$\xi_{Eth} = \frac{36}{4.67} * 0.04 = 0.3 \text{ hr}^{-1}$$

Regressed value of DCE back-partitioning coefficient for Experiment-B =  $0.004 \text{ hr}^{-1}$

Similar calculations can be performed and the back-partitioning coefficients for the other daughter products of Experiment-B could be determined.

## A-2. PERSULFATE ELUTION DURING THE SINGLE FRACTURE CHEMICAL OXIDATION EXPERIMENTS

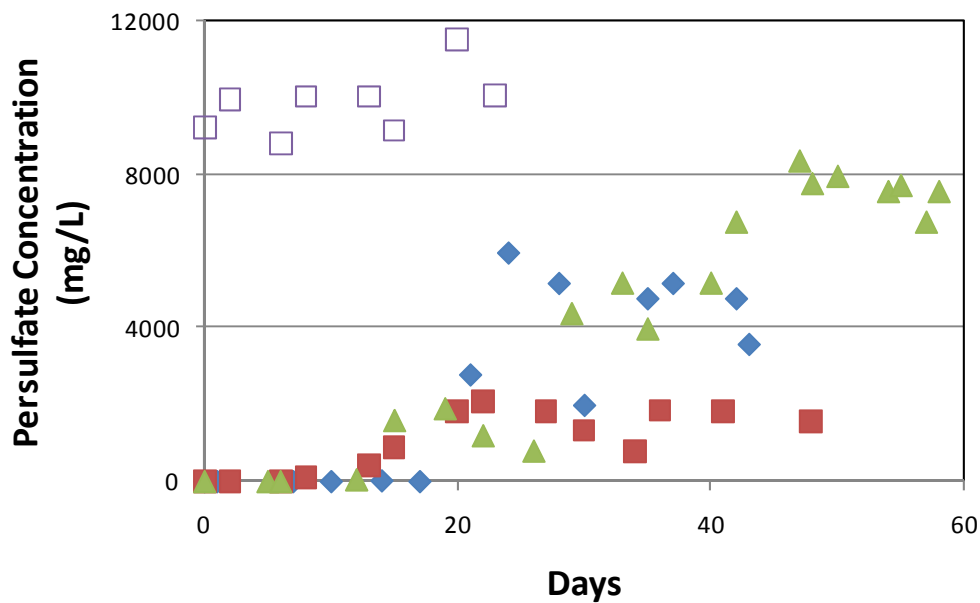


**Figure A-2.** Persulfate effluent concentrations for the four persulfate experiments. ♦ - A1 (persulfate + 1,000 mg/L Fe-EDTA), ■ - A1 (persulfate + 500 mg/L Fe-EDTA), ▲ - C2 (persulfate + 500 mg/L Fe-EDTA), □ - C2 (alkaline activated persulfate).



## APPENDIX B: LIST OF PUBLICATIONS

### *Articles in peer-reviewed journals*

- Schaefer, C.E.; Callaghan, A.V.; King, J.D.; McCray, J.E. Dense nonaqueous phase liquid architecture and dissolution in discretely fractured sandstone blocks. *Environ. Sci. Technol.* **2009**, 43, 1877-1883.
- Schaefer, C.E.; Towne, R.M.; Vainberg, S.; McCray, J.E.; Steffan, R.J. Bioaugmentation for treatment of dense non-aqueous phase liquid in fractured sandstone blocks. *Environ. Sci. Technol.* **2010**, 44, 4958-4964.
- Schaefer, C.E., Towne, R.M., Vainberg, S., McCray, J.E., and Steffan, R.J. Assessment of chemical oxidation for treatment of dense non-aqueous phase liquid in fractured sandstone blocks. *J. Environ. Engin. (review decision 2011 – minor revisions)*.
- Christensen, K., McCray, J., Altman, P., Schaefer, C. Steady state DNAPL dissolution kinetics in a three-dimensional experimental fractured sandstone network. submitted to *J. Contam. Hydrol.*
- Torlapati, J., Clement, T. P., Schaefer, C.E., Lee, K.K. Modeling *Dehalococcoides sp.* augmented remediation in fractured sandstone. submitted to *Ground Water Monitor. Remed.*

### *Articles in preparation*

- Christensen, K., McCray, J., Schaefer, C. DNAPL dissolution and mass removal during chemical oxidation in a three-dimensional experimental fractured sandstone network.
- Altman, P., McCray, J., Schaefer, C. DNAPL dissolution during bioaugmentation in a three-dimensional experimental fractured sandstone network.